UV laser source for atom optics experiments with metastable helium

A thesis submitted for the degree
of Masters by Research of
the Australian National University

Ivan Blajer

September 22, 2004

This thesis contains no material which has been accepted for the award of any other degree or diploma in any university. To the best of the author's knowledge and belief, it contains no material previously published or written by another person, except where due reference is made in the text.

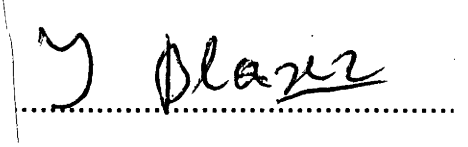

Ivan Blajer

September 22, 2004

Contents

Summary of Thesis

The development of a practical UV laser source at 389nm for use in metastable helium experiments is reported in this thesis. The motivations for which are in order to study the interactions of very cold metastable helium atoms (1 mK) in a magneto-optical trap (MOT) with 389nm photons which are not well understood. Secondly the use of the laser source as an imaging and diagnostic tool would greatly enhance the efficiency of current setups based on CCD cameras and photodetectors that use fluorescence based on the interaction with the helium transition at 1083nm.

Currently the only method for producing cw tunable radiation at this wavelength is the use of non-linear techniques in particular second harmonic generation of near IR laser sources such as Ti:Sapphire lasers, the theory of which is presented in chapter 2. The ability to produce adequate powers relies on resonant enhancement in an external cavity, thus significant effort was made on maximising the output power which is discussed in chapter 4. I have shown that the maximum possible output power with the current setup is 30mW at 389nm for 1W input power. This agrees with the theoretical maximum which is based on the reflectivity of the current optics set.

Due to the use of an external cavity, the use of feedback stabilisation is necessary to produce a usable beam with low intensity noise. Previously the system suffered from significant intensity noise of around 30%. With the development of a new feedback controller and more stable electronics, the noise has been reduced to less

than 10%. The feedback stabilisation system is characterised and a model developed to predict its behaviour and ways to improve the current state of the system. This is described in chapter 5.

Finally the observation of saturated absorption spectroscopy in a DC discharge cell at this new wavelength is reported. Frequency locking of the UV output to the 3^3P state of helium was subsequently achieved, enabling more quantitative experiments to be performed with the system in the future, which previously had not been possible.

Acknowledgements

Firstly I would like to thank my principal supervisor Dr Ken Baldwin for his guidance over the course of my project and for reading and correcting this thesis. Thank you to Dr Matt Sellars for the stimulating discussions, help in the laboratory concerning the laser control electronics side of things and for corrections to the thesis. Dr Andrew Truscott for suggestions when things weren't working in the lab and maintaining the pump laser. Dr Jeroen Koelemeij from the Vrije University in Amsterdam who visited for a month and imparted some of his practical experience with the 389nm system. Thank you to Dr Stephen Buckman and Prof. Neil Manson for their encouragement and support.

Thank you to the highly professional AMPL technical staff Mr Steve Battison, Mr Kevin Roberts and Mr Graham Cornish for their help over the last two years. Also to the staff at electronics Mr Dennis Gibson, Mr Michael Blacksell and Mr David Anderson.

I can't thank enough my fellow lab colleagues, in particular Rob Dall and Linda Uhlmann for putting up with my bad moods and passing on their laboratory experience on to me. To James Swansson for developing the laser system to the state that I found it in. The department would have not been so enjoyable if not also for the likes of Johanna Nes, Milica Jelisavcic, Thomas Senn, Tom Hanna and Rene Chaustowski for the laughs and friendship. Special thanks also go to Ben McMillan, Dave Pretty, Danielle Medek, Victoria Coleman, Clive Michael, Phil Krins, Lionel

Darre, Frances Rivera and Katie Orr for their love and friendship making Canberra such a lovely place to live in.

Finally to my family for their moral and fiscal support without whom I would have not have made it. For my mum Novka, dad Zlatko and brother Anton that endured my absence, stress and bankrupcy. They believed and loved me even when I didn't. This one is for you. *Mnogu ve sakam!!!!*

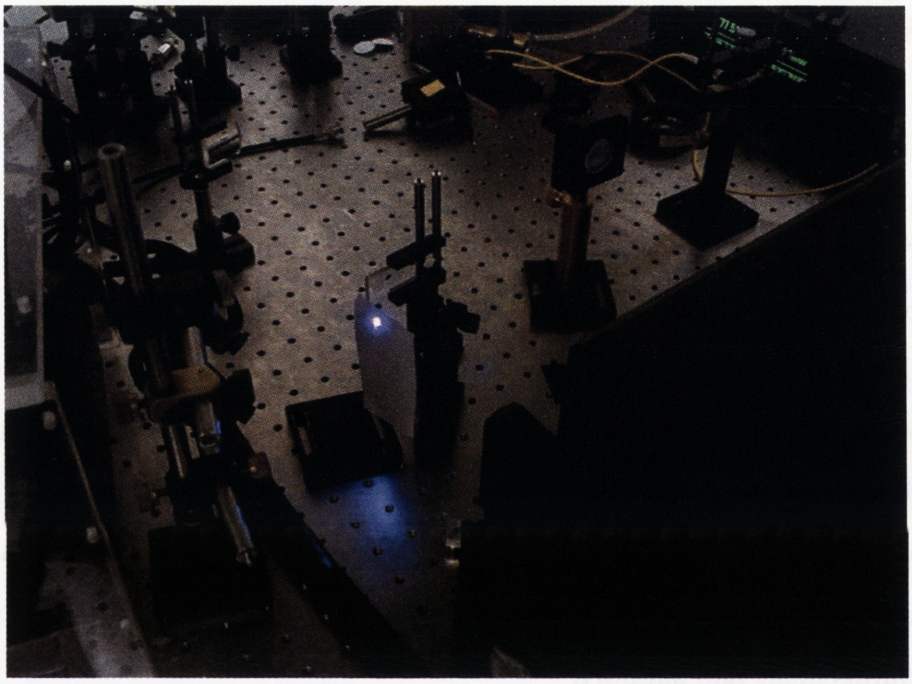

Figure 0.1: The 389nm laser in action!

CHAPTER 1

Introduction

1.1 Laser manipulation of atoms

The use of coherent laser sources for the purpose of cooling and manipulation of neutral atomic species has been well established since the mid 80's. The field was pioneered by Steven Chu, William D. Phillips and Claude Cohen-Tannoudji, who jointly received the Nobel Prize in 1997 for their ground breaking work which established a new area of physics, commonly referred to as atom optics. Atom optics deals with the properties of atoms, both classical and quantum, using external fields or microstructures which are used to both probe and influence their behaviour. The development of stable, broadly tunable laser sources since the 1960's has enabled an atom's internal and external states to be studied and manipulated with unprecedented precision. The experimental realisation of Bose-Einstein condensation in 1995 was one of the most exciting breakthroughs of modern physics, which was theoretically predicted almost 70 years earlier and is a direct product of the techniques that encompass atom optics. These techniques enable neutral atoms to be manipulated in ways similar to those by which optics manipulates light. Many analogues of optical elements have been built in the laboratory, giving striking proof for the wavelike properties of matter. These properties become apparent when the de Broglie wavelength given by $\lambda_{dB} = \frac{h}{p}$ (where h is Planck's constant and p is the

atomic momentum) is comparable with the characteristic scale of the atom optical device.

In the atom manipulation laboratory at the ANU the properties of metastable helium atoms are studied in its interaction with laser light in cold atom scattering experiments, atom lithography and atom guiding in hollow optical fibers.

1.2 Metastable helium

In my experimental investigations I studied the interaction of intense laser light with metastable helium using a cooling transition at 389nm. Metastable helium has several distinct advantages over other atomic species which are commonly used for this types of experiments. The first atoms which were laser cooled were the alkali-metals (Na, Cs, Rb, Li and K). These have relatively simple level structure since their electronic configuration consists of a closed shell and one valence electron, enabling the system to be approximated by a one electron atom [1]. Further the transitions from the ground state lie in the visible part of the spectrum, making them accessible with laser light. They also have a high vapour pressure at relatively low temperatures, enabling straightforward creation of atomic beams.

The other group of elements used for atom optics experiments are the noble gases (He, Ne, Ar, Kr and Xe). While they are chemically inert under normal conditions and have no transitions accessible to laser light, it is possible to excite one of the electrons to a low lying excited state which is metastable. This is commonly done in an electric discharge inside the atomic source. These metastable states have long life times, e.g. 8000 s for the 2^3S_1 state of helium, and can consequently act as the effective ground state in atom optics experiments. The noble gases have several advantages over the alkali metals, especially since they have no nuclear spin and show no hyperfine splitting, thus reducing the number of states available. The high internal energy of the metastable state also makes it easy to detect single atoms

using charged particle detectors with near unit efficiency.

Helium has the simplest energy level structure of the noble gas atoms, a part of which is shown in Fig.1.1 It also has the lowest mass, thus giving it a high recoil

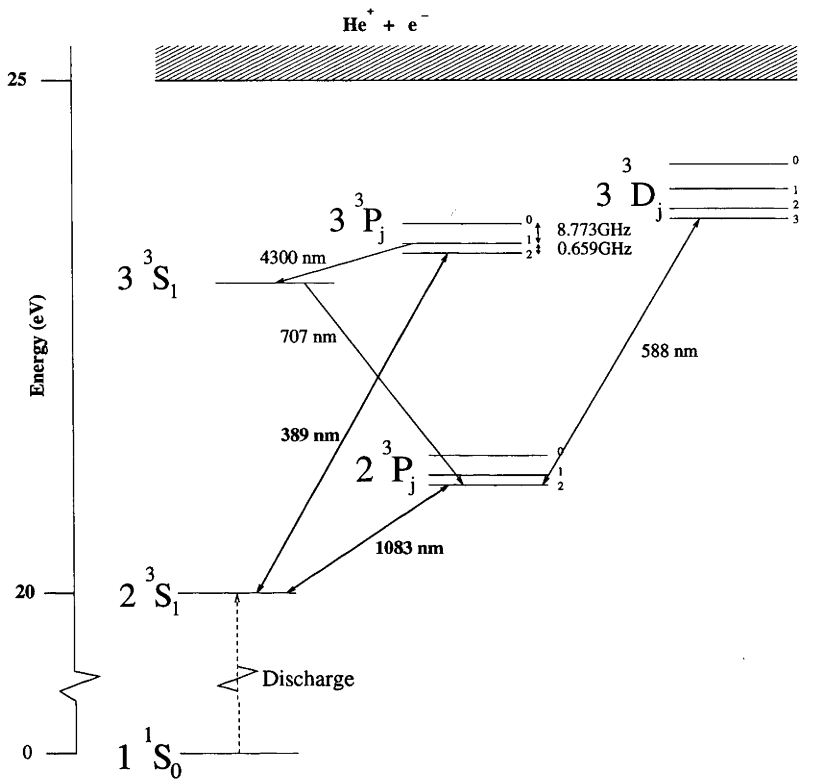

Figure 1.1: Energy level diagram of triplet helium, bold arrows indicate the two cooling transitions at 1083 and 389nm

velocity in comparison to other metastable atomic species.

The effective groundstate in metastable helium is the 2^3S_1 which has a lifetime of 8000s. Excitation to the metastable state is usually performed in an electrical discharge, 20eV being the excitation energy per atom. The two transitions in metastable helium used for atom optics are at 1083 and 389nm corresponding to transitions from the 2^3S_1 to the 2^3P_j and 3^3P_j states respectively. When choosing a cooling transition, the atomic parameters shown in Table 1.1 need to be considered, because they ultimately determine the limiting temperatures and densities in the

different cooling regimes.

In Table 1.1 Γ is the natural linewidth of the transition, where $\Gamma = 1/2\pi\tau$ and

Transition	λ(nm)	Γ (MHz)	I_{sat}(mW/cm^2)	v_r(cms^{-1})	a_{max}(cms^{-2})
$2^3S \rightarrow 2^3P$	1083	1.6	0.17	9.14	4.6×10^7
$2^3S \rightarrow 3^3P$	389	1.5	3.72	25.45	1.3×10^8
$2^3P \rightarrow 3^3D$	588	11.4	7.32	16.84	6.0×10^8

Table 1.1: Laser transition parameters for triplet He* [1].

τ is the natural lifetime of the upper state in seconds. The parameter $I_{sat} = \frac{\pi hc}{3\lambda^3\tau}$ depends only on the wavelength and the linewidth, and provides a measure of the intensity needed to saturate the transition. The recoil velocity v_{rec} is the change in velocity an atom experiences per photon scattering event. The maximum acceleration experienced by an atom is a_{max} which occurs under high saturation conditions. The implications of these parameters for atom optics experiments will be discussed below and in later chapters.

There has been considerable progress in the field of laser cooling and trapping of metastable helium with high densities and large atoms numbers realised inside a MOT by several groups using the 1083nm transition [2] [3], [4], [5], [6] including the realisation of Bose-Einstein Condensation (BEC) in 2001 [4], [5]. The light is produced by specialised DBR laser diodes which can be used in conjunction with Yb-doped fiber amplifiers to produce several watts of 1083nm light. The main advantages of this transition are the low saturation intensity of 0.17mW/cm^2 and the availability of tunable high powered sources with sub-megahertz linewidth. The $2^3S_1 \rightarrow 2^3P_j$ transition forms a closed system using circularly polarised light which is necessary for efficient deceleration of the atoms over many absorption/emission cycles. Inside a metastable helium trap losses are dominated by Penning collisions which occur between metastables, and the associated two body loss rate depends

on which state the atoms are in when the collisions occur e.g.

$$\mathrm{He}^\star + \mathrm{He}^\star \rightarrow \mathrm{He} + \mathrm{He}^+ + e^- \qquad (1.1)$$

$$\mathrm{He}^\star + \mathrm{He}^\star \rightarrow \mathrm{He}_2^+ + e^-$$

The loss rate coefficient for this process using 2^3P excited state collisions with 2^3S_1 atoms is of the order of $5 \times 10^{-9}\mathrm{cm}^3/\mathrm{s}$ depending on the detuning [7]. In most situations it is desirable to minimise these losses while maximising the trap density and the number of atoms trapped at lower temperatures.

It has been shown in several experiments [8], [9], [10] that the transition at 389nm has several advantages over 1083nm that address some of these issues. One experiment has led to the observation of lower than expected temperatures [8] which haven't been thoroughly investigated, and a novel type of VSCPT (velocity selective coherent population trapping) [10] was observed. The two body loss rate has been shown to be 7 times smaller for the 3^3P-2^3S_1 collisions assuming the atomic densities are equal [8]. However, there is an additional loss rate through two-photon ionisation of 3^3P state. Also, the 389nm excitation is not a closed transition since there is a 10 % leakage into the 3^3S_1 state. A further disadvantage of the 389nm transition is the higher I_{sat} requiring higher powers to be used. The two transitions have similar natural linewidths while the recoil velocity for 389 nm is 2.8 times larger than 1083 nm, leading to a larger spontaneous cooling force and thus a more compressed cloud. The higher recoil momentum also would yield larger beamsplitter separations in experiments such as atomic gratings where the splitting angle is proportional to the recoil $\hbar k$. Optical lattices made using 389nm light would yield smaller lattice scale lengths since the spacing between lattice sites is $\lambda/2$. Recently it has been shown that long range dimers can be produced through photoassociation spectroscopy at 1083nm [6], [11] although it remains an open question whether such long-range bound molecular states exist for the transition at 389nm. Using the transition at 389nm also has a more practical advantage for metastable helium atom optics experiments which use detection of the fluorescence from the atomic cloud,

e.g. as an imaging and diagnostic technique to determine the size and density of the atomic cloud. This is because CCD cameras have much higher quantum efficiency at 389nm compared to 1083nm leading to higher signal to noise ratios.

In the Atom Manipulation Laboratory the physics of metastable helium are studied through several ongoing experiments. A bright atomic beam for beam atom optics experiments is also capable of loading a MOT. In the MOT both atom-atom and electron-atom collisions are studied. Also the guiding of helium atoms in hollow optical fibres with laser light was demonstrated. The atomic source consists of a nitrogen cooled DC helium discharge that passes through collimation, Zeeman slower and two compressor stages where the helium atoms are captured by the MOT. Up to 1×10^9 atoms are trapped with a density of $\approx 1 \times 10^{10}$atom/cm^3 at a temperature of 1mK [12], [13]. This year a new beamline optimised for higher densities based on a helium-cooled rather than a nitrogen cooled source has come online [14], resulting in a smaller mean velocity of the atoms produced in this source. Thus the whole system is more compact and higher densities can be achieved with a view to producing a BEC. Both beamlines use the $2^3S_1 \rightarrow 2^3P_2$ cooling transition of helium at 1083nm. In this thesis I report on the significant improvement of an existing laser source at 389nm to access the $2^3S_1 \rightarrow 3^3P_j$ group of transitions. This is to be used as a complementary source to the existing 1083nm lasers for the improvement of current imaging/cooling techniques and the study of new phenomena at this wavelength.

1.3 The scope of this thesis

The focus of this thesis is improvement of the existing 389nm cw laser setup to enable new experiments to be undertaken. My improvements relate to the frequency stabilisation and intensity stabilisation of the output 389nm beam. Saturated absorption spectroscopy was successfully performed enabling the 3^3P states to be

clearly resolved and frequency locked to the relevant cooling transition. This had previously not been observed with this system. The limitations to the output power were also investigated and suggestions have been made to correct them. The realisation of the goals of this project required a total rebuild of the whole system which had not been operational for some time and a characterisation of all the components with only the basic layout of the cavity and locking setup being initially in place.

Chapter 2 of this thesis deals with the theory of non-linear optics, second harmonic generation with Gaussian beams and the use of cavity enhancement in the context of second harmonic generation. The choice of design for the 389nm frequency doubling laser are outlined at the conclusion of the chapter.

The main sections of the apparatus and some relevant theory are described in Chapter 3. The chapter includes some additional theory on the feedback control of laser cavities, and covers the locking scheme and PID control.

Experimental results focusing on the optimisation of the output power are presented in Chapter 4. The contributing factors to the output power level (in particular the mode matching and enhancement in the cavity) are dealt with in this chapter.

Chapter 5 deals with the frequency stabilisation of the cavity to the laser pump. The relevant aspects of control theory are presented along with a model of the current control system and the performance of its components, and how they effect the overall frequency stability. The measured intensity stability of the output is presented and quantified and compared with the model.

Chapter 6 covers aspects of laser spectroscopy relevant to the experiments that were performed to observe saturated absorption spectroscopy in a DC discharge at 389nm. The detailed experimental procedure is described and traces of the saturated absorption signals are presented. The technique for subsequent locking of the UV output to the atomic transition is described.

Important aspects of this thesis, including the cavity alignment procedure which

yielded the maximal power, and the details of modeling of the cavity, are presented in the appendices. Electronic circuits crucial to the development of the system for the cavity controller and differential photodetector are also included in the appendices. Finally, a practical guide to locking the cavity is also included for completeness and instructional purposes.

CHAPTER 2

Second harmonic generation of 389nm light in LBO

2.1 Non-linear optics

One of the largest growing fields of research in modern physics is the study of non-linear phenomena. In the scope of non-linear optics, the interaction between light and matter is such that the output properties of the light field are not linearly dependent on the input field. In particular the output amplitude depends in a non-linear fashion on the input amplitude. When an atom is placed in an oscillating electromagnetic field it induces a dipole moment in the electron distribution which in turn oscillates, re-emitting the input radiation [15]. This is called the polarisation wave $\mathbf{P}$

$$\mathbf{P}(\mathbf{r},\mathbf{t}) = \chi\mathbf{E}(\mathbf{r},\mathbf{t}) \tag{2.1}$$

Here $\mathbf{E}$ is an oscillating electric field whose amplitude depends on both the position $\mathbf{r}$ as well as the time t. The constant χ is the linear susceptibility through which many commonly encountered effects such as absorption, refraction, reflection, normal and anomalous dispersion are mediated. At low intensities the electron can be seen as moving in a harmonic potential driven by the external field. At higher intensities the potential is no longer harmonic, leading to higher order effects. In this case the

polarisation $\mathbf{P}$ is expanded in a power series of the input field.

$$\mathbf{P}(\mathbf{r},t) = \chi_1\mathbf{E}(\mathbf{r},t) + \chi_2\mathbf{E}^2(\mathbf{r},t) + \chi_3\mathbf{E}^3(\mathbf{r},t) + \chi_4\mathbf{E}^4(\mathbf{r},t) + ... \tag{2.2}$$

The first term in the series is the dominant first order susceptibility which leads to the before mentioned linear effects. The higher order terms (for which the higher order susceptibilities χ_i generally are successively smaller) are the realm of non-linear optics. The effects arising from the various terms in these series include upconversion, sum/difference frequency generation, parametric oscillation, self focusing and numerous other effects. These are often realised in practice in non-linear crystals, so-c-alled because of their relatively large higher order susceptibilities.

One common nonlinear technique is the frequency doubling of lasers which arises from the second order susceptibility, and produces a polarisation wave at the second harmonic of the input wavelength, with power proportional to the square of the input power. Second harmonic generation has been used to produce high power tunable laser light at wavelengths for which lasing media either don't exist, or are expensive or difficult to operate. In this thesis we produce laser light at 389nm by second harmonic generation in an LBO crystal.

2.2 General theory of second harmonic generation

Second harmonic generation using a laser beam was first demonstrated in 1961 by Franken *et al.* [16] and was the first nonlinear optical phenomenon to be observed in the laboratory. The process arises from the second order χ_2 term in equation 2.2 where the polarisation wave created in the medium can be decomposed into two components which oscillate at both fundamental and at twice the fundamental frequency. A laser beam of frequency ω incident on a non-linear material has an electric field strength that can be represented as

$$E(t) = Ee^{i\omega t} + c.c. \tag{2.3}$$

If this is substituted for E in equation 2.2 and ignoring terms higher than E^2 we get as in [15]

$$P(t) = \chi_1 E e^{i\omega t} + 2\chi_2 E E^* + (\chi_2 E^2 e^{2i\omega t} + c.c) + c.c \tag{2.4}$$

As can be seen from the equation above the polarisation wave contains three components: the first being at the same frequency as the input field; the second component is a component at zero frequency, which means that a static (DC) field is induced inside the medium; and the third component is the second harmonic. Second harmonic generation can also be visualised from a quantum mechanical point of view as photons being exchanged between the various frequency components of the electromagnetic field. This is shown schematically in figure 2.1 where two photons of frequency ω are destroyed and a single photon of frequency 2ω are created in a single event [15].

During this process both the energy and the momentum of the photons must be

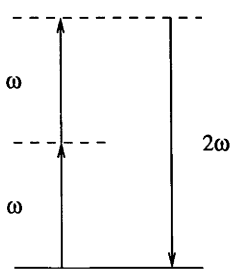

Figure 2.1: Energy level diagram describing second harmonic generation at 2 ω from fundamental radiation at frequency ω.

conserved, which can be expressed respectively as:

$$\hbar\omega + \hbar\omega = 2\hbar\omega \tag{2.5}$$

$$\vec{k}_\omega + \vec{k}_\omega = \vec{k}_{2\omega} \tag{2.6}$$

where $\hbar = h/2\pi$ and $|\vec{k}_\omega| = \frac{2\pi}{\lambda}$ is the wave vector of the radiation. The second equation is the condition of phase matching and for incident plane waves one can define the phase mismatch as:

$$\Delta k = 2k_\omega - k_{2\omega} = 2\frac{2\pi}{\lambda_1} - \frac{2\pi}{\lambda_2} = \frac{2\omega}{c}(n_1 - n_2) \tag{2.7}$$

Here c is the speed of light, and n_1 and n_2 represent the two indices of refraction $n = c/\nu\lambda$, for the fundamental and second harmonic respectively. This means that the two waves travel through the medium at different speeds $v = c/n$, making it possible for the harmonic waves created at different places to cancel each other out. For plane waves the intensity of the harmonic wave is related to the phase mismatch through

$$I = I_{max}\frac{sin^2(\Delta kL/2)}{(\Delta kL/2)^2} \tag{2.8}$$

which as expected is sharply peaked at $\Delta k = 0$. Thus phasematching is crucial.

Most materials exhibit a property for wavelengths well away from absorption edges called normal dispersion, for which the refractive index is an increasing function of frequency, and for which a zero phase mismatch is not possible. The solution is to use birefringent materials where the refractive index is also dependent on the polarisation of the incident radiation at a particular wavelength. Birefringent crystals enable near perfect phasematching to be achieved through the dependence of the refractive index on the polarisation as well as frequency. This is illustrated in figure 2.2 for the case of a positive uniaxial crystal. It can be seen that it would be possible to choose a pair of wavelengths second harmonic and fundamental wavelengths for which the refractive indices are equal. The polarisations for the fundamental waves define the two types of phase matching commonly used:

Type I

In this type of phasematching the polarisation of the fundamental waves are parallel to each other, and the second harmonic is perpendicular to this direction. So the

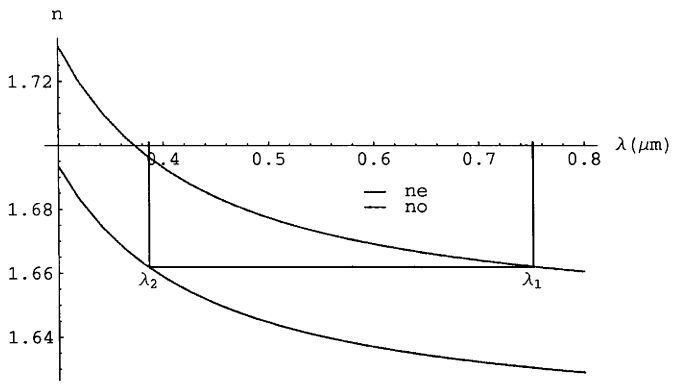

Figure 2.2: The refractive indices for the two polarisations labeled n_o and n_e for the case of a negative uniaxial crystal as a function of wavelength $\lambda(\mu\text{m})$. Phasematching is satisfied for a pair of wavelengths λ_1 and λ_2 representing the fundamental and second harmonic fields respectively.

refractive indices at ω and 2ω are made equal along the two axes ie

$$n_e(2\omega) = n_o(\omega) \tag{2.9}$$

The subscripts o and e refer to the ordinary and extra-ordinary planes of polarisation with respect to the crystal axis.

Type II

The two incident and induced polarisations at the fundamental are perpendicular to each other. The second harmonic is parallel to one of these waves. The refractive index at the second harmonic is made to equal the sum of the refractive indices for the two polarisations of the fundamental.

$$n_e(2\omega) = \frac{1}{2}(n_o(\omega) + n_e(\omega)) \tag{2.10}$$

The choice of phase matching scheme depends on the crystal properties and requirements of the particular experiment. Usually one or the other type is used. In general type I is easier to achieve, however type II requires less bi-refringence.

Commonly type I phase matching is achieved by angle tuning the crystal illustrated in figure 2.3. The figure 2.3 shows critical phasematching where the wave vector **k**

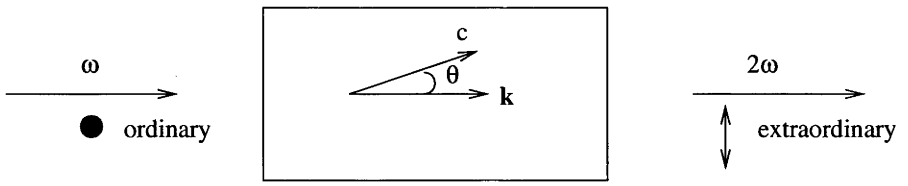

Figure 2.3: Geometry of phasematching by angle tuning, c indicates the optic axis of the crystal and arrows indicate the polarisation of the incident and emitted radiation.

propagates at angle θ to the crystal axis c. The second harmonic wave oscillating at frequency 2ω is polarised perpendicular to the fundamental wave at frequency ω. Type II phasematching is usually performed by temperature tuning the non-linear crystal.

In practice, second harmonic generation is usually realised using laser beams which possess a Gaussian intensity profile, rather than a plane wave. Thus a theory which enables the calculation of the output beam properties in terms of the input beam optical intensity profile and crystal parameters is discussed in the following sections.

2.3 Gaussian beam propagation

The propagation and behaviour of laser beams is the field of Gaussian optics which concerns itself with solutions of the paraxial wave equation. Here I briefly follow some of the main points from the early paper by Kogelnik and Li [17]. Coherent light waves satisfy the scalar wave equation for the field component or potential u as given by

$$\nabla^2 u + k^2 u = 0 \tag{2.11}$$

We assume the laser beam is traveling in the z direction for which the solution is given as

$$u = \psi(x, y, z)e^{-ikz} \tag{2.12}$$

Here $\psi(x, y, z)$ is a slowly varying complex function which represents the differences between plane waves and Gaussian beams, namely a non-uniform intensity distribution perpendicular to the propagation direction, the expansion of the beam with distance, and curvature of the phase fronts. These properties of laser beams lead to some unique effects when they are applied to optical systems. The solution for u when inserted into equation 2.11 leads to an equation for the complex varying amplitude ψ:

$$\frac{\partial^2\psi}{\partial x^2} + \frac{\partial^2\psi}{\partial y^2} - 2ik\frac{\partial\psi}{\partial z} = 0 \tag{2.13}$$

Here $d^2\psi/dz^2$ has been neglected since the amplitude varies very slowly with the propagation direction z, with $z = 0$ being defined at the focus of the laser beam. This wave equation has as one of the solutions the so called TEM_{00} mode which yields a Gaussian transverse intensity profile for the laser beam. Although it is not the only solution, it is the most important and is also called the fundamental mode. For example, the higher order modes of a laser resonator with rectangular symmetry are products of the fundamental mode solution and Hermite polynomials. The form of the lowest order mode is given by

$$\psi = exp\{-i(P + \frac{k}{2q}r^2)\} \tag{2.14}$$

where $P(z)$ is a parameter which gives the complex phase shift as a function of the propagation distance, and $q(z)$ is the complex beam parameter. This describes the Gaussian variation of intensity as a function of distance from the optic axis where $r^2 = x^2 + y^2$. The complex beam parameter q is decomposed into two more intuitive beam parameters R and w as follows

$$\frac{1}{q} = \frac{1}{R} - i\frac{\lambda}{\pi w^2} \tag{2.15}$$

In this equation $R(z)$ is the radius of curvature that intersects the optic axis and $w(z)$ is the scale length for decrease of field amplitude from the center. This decrease has a Gaussian form and the so called spot size w is measured as the distance at which the field amplitude drops to $1/e$ times the value in the center. The beam has a Gaussian profile at every cross section along the axis. but the spot size w changes along the axis. The diameter of a laser beam at any point along the axis is simply $2w$. There is an important point at $z = 0$ along the propagation axis at which R in equation 2.15 is infinite i.e. the wave fronts are plane. At this point the beam diameter is at its minimum $2w_o$ and usually z is measured from this point. The complex beam parameter is purely imaginary at this point:

$$q_o = i\frac{\pi w_o^2}{\lambda} \tag{2.16}$$

The variation of the spot size w and the wavefront curvature R along the axis z are given by the following equations:

$$w^2 = w_o^2[1 + (\frac{\lambda z}{\pi w_o^2})^2] \tag{2.17}$$

$$R(z) = z[1 + (\frac{\pi w_o^2}{\lambda z})^2] \tag{2.18}$$

The equation for the spot size $w(z)$ is a hyperbolic function and is shown in figure 2.4. The asymptotic behaviour of equation 2.17 yields the far field diffraction angle θ and is given by

$$\theta \simeq \frac{\lambda}{\pi w_o} \tag{2.19}$$

This is a useful quantity which gives a simple relation for beam propagation for distances much greater than the so-called Rayleigh length z_R from the waist.

$$z_R = 2\pi w_o^2/\lambda = k w_o^2/2 = b/2 \tag{2.20}$$

The Rayleigh length represents the extent of the focal region of the laser beam.

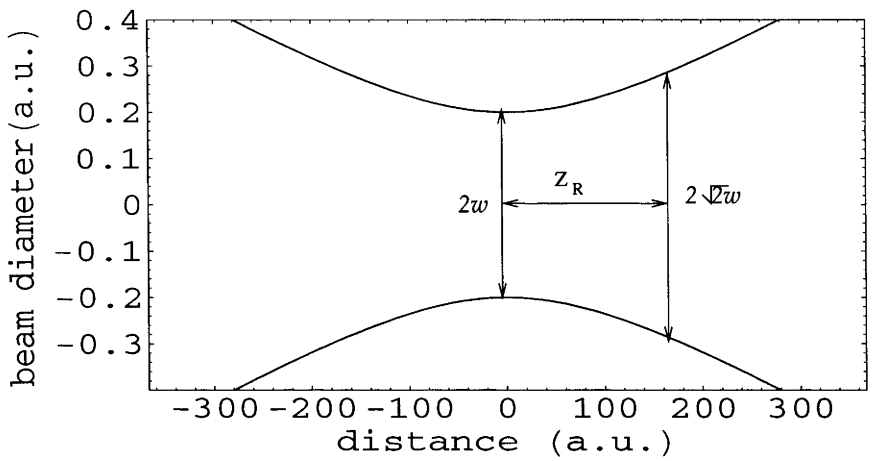

Figure 2.4: The waist of a laser beam at the focus as function of distance from the origin at $z = 0$. The quantity z_R represents the Rayleigh length.

It is important to discuss how laser beams travel through optical elements. This will enable calculation of the required beam parameters of the frequency doubling cavity. The ray matrix formalism [17] provides a convenient and powerful tool for calculating the resultant beam parameters given an arbitrary optical system and the input beam. It is based on the principle that a simple optical system such as a lens can be represented by the following form:

$$\begin{pmatrix} r' \\ \theta' \end{pmatrix} = \begin{pmatrix} 1 & 0 \\ -1/f & 1 \end{pmatrix} \begin{pmatrix} r \\ \theta \end{pmatrix} \tag{2.21}$$

In the above formalism the entries of the column vectors represent the radial displacement r from the optic axis and angle θ at which a ray is traveling. The positions of the input and output planes in this case are immediately before and after a lens of focal length f. If the system is made up of a series of lenses then the total matrix is calculated by matrix multiplication of the transfer matrices describing each individual element, with the first element in the beam path appearing last in the multiplication. This framework is very useful for ray tracing calculations with large numbers of elements, and also works with Gaussian optics with a few additions. A

simple lens does not affect the transverse intensity distribution of the beam i.e. a Gaussian remains a Gaussian, a higher mode retains its shape. However the lens modifies the spot size w and curvature R discussed previously. The output beam parameter q_2 immediately after an ideal thin lens is related to the input parameter q_1 as follows.

$$\frac{1}{q_2} = \frac{1}{q_1} - \frac{1}{f} \tag{2.22}$$

A more complicated system can be calculated using the so called ABCD law given by

$$q_2 = \frac{Aq_1 + B}{Cq_1 + D} \tag{2.23}$$

The A, B, C and D are the elements of the total ray transfer matrix of the form of equation 2.21. In following sections it will be shown how this theory can be used to describe and predict the behaviour of the beam as it travels inside the doubling cavity, since an optical resonator can be unfolded into a series of lenses. The generation of the second harmonic power is highly dependent on the beam parameters as will be shown in the following section, and the doubling cavity has to be designed with these parameters in mind.

2.4 Second harmonic generation with Gaussian beams

Second harmonic generation is a common tool for extending the spectral range of many laser systems, enabling a wider range of applications. The theory of second harmonic generation for a general case using Gaussian beams was first treated by Boyd and Kleinman [18]. In the paper they derive expressions for the second harmonic power in terms of the properties of the incident beam and the crystal parameters in the situation where a non-linear crystal is placed at the focus. To calculate the second harmonic wave traveling along the z direction a solution is sought of wave equation similar to equation 2.13 except now there is a source term

i.e. the induced polarisation wave that appears on the right hand side via the χ_2 non-linearity [15]:

$$\nabla_T^2 u_2 + 2ik_2 \frac{\partial u_2}{\partial z} = -\frac{4\pi\omega_2^2}{c^2}\chi_2 u_1^2 e^{i\Delta kz} \tag{2.24}$$

Here $\Delta k = 2k_1 - k_2$ is the phase mismatch discussed previously and the labels 1, 2 represent the fields oscillating at the fundamental and second harmonic frequency. The $u_{1,2}$ are amplitudes of the fundamental and second harmonic field with $\omega_{1,2}$ being their respective frequencies. It can be seen that the second harmonic depends on the square of the input field u_1 as expected. The trial solution for u_1 is the Gaussian solution given by equation 2.14, slightly reworked into a more compact dimensionless form [15].

$$u_1(r,z) = \frac{A_1(z)}{1+i\tau} e^{-r^2/w_o^2(1+i\tau)} \tag{2.25}$$

$$u_2(r,z) = \frac{A_2(z)}{1+i\tau} e^{-2r^2/w_o^2(1+i\tau)} \tag{2.26}$$

The term $\tau = 2z/b$ is simply the propagation coordinate z normalised to the confocal parameter of the beam in equation 2.20. The approximation is also made that pump power is constant, which is valid in situations where only a small fraction of the power is converted into the second harmonic. This is not always true and leads to effects discussed in later sections. Both beams have equal confocal parameters which is physically intuitive because the second harmonic is generated coherently over the longitudinal extent of the fundamental beam. Since the confocal parameters are equal, the second harmonic beam has a waist that is $\sqrt{2}$ times the waist of the fundamental, a proportionality that is also true for the far field diffraction angle. The solutions of equation 2.26 are inserted into the wave equation 2.24, and the

following equation for the second harmonic amplitude A_2 can be derived:

$$A_2(z) = \frac{i4\pi\omega}{nc}\chi^2 A_1^2 J_2(\Delta k, z_0, z) \tag{2.27}$$

$$J_2(\Delta k, z_0, z) = \int_{z0}^{z} \frac{e^{i\Delta k z' dz'}}{(1 + 2iz'/b)} \tag{2.28}$$

In the plane wave limit i.e. for weak focusing which corresponds to $b \gg |z_0|, |z|$

$$J_2(\Delta k, z_0, z) = \int_{z0}^{z} e^{i\Delta k z' dz'} = \frac{e^{i\Delta k z} - e^{i\Delta k z_0}}{i\Delta k} \tag{2.29}$$

which has the result that

$$|J_2(\Delta k, z_0, z|^2 = L^2 \frac{\sin^2(\Delta k L/2)}{\Delta k L/2} \tag{2.30}$$

$L = z - z_0$ is the length of the interaction region and z_0 and z correspond to the positions of the entrance and exit faces of the crystal relative to its center. The last equation displays the dramatic decrease of the second harmonic amplitude for $\Delta k \neq 0$, and is proportional to the square of the interaction length. The square of $A_2(z)$ gives the intensity $I_2(z)$ at each point along the axis, and these contributions are summed over the interaction length to give the power P_{2w} emanating at the exit face of the crystal. The relation for P_{2w} in terms of the input power P_w according to [18] is thus:

$$P_{2w} = \gamma_{shg} P_w^2 \tag{2.31}$$

$$\gamma_{shg} = \frac{2w_1^2 d_{eff}^2 k_1 l}{\pi n^3 \epsilon_0 c^3} h(B, \xi) \tag{2.32}$$

Where the symbols are defined as follows:

γ_{shg} - the single pass second harmonic conversion efficiency (W^{-1})

d_{eff} - the effective nonlinear constant (m/V)

$k_1 = 2\pi/\lambda_1$ - the wavenumber for the fundamental wave (m^{-1})

w_1 - waist size of the fundamental beam inside the crystal (m)

ϵ_0 - the permitivity of free space (F/m)

n - the index of refraction at the fundamental frequency

c - the speed of light in vacuum (m/s)

ρ - the walk off angle (rad)

l - length of crystal (m)

$h(B,\xi)$ - is the Boyd and Kleinman focusing parameter

The original paper goes into great detail of the derivation of this form expressions for last factor $h(B,\xi)$. This factor depends on the walk-off parameter $B = \rho\sqrt{lk_1}/2$ and the focusing parameter $\xi = l/b$. Walk-off is a consequence of birefringence, which as mentioned before is neccesary to obtain optimum phasematching. The fundamental and second harmonic have Poynting vectors which do not travel in the same direction but at walk-off angle ρ with respect to each other. In situations where there is a large walk-off, the optimum phasematching condition in fact is not $\Delta k = 0$. Under conditions where $4B^2 > \xi > 6/B^2$, which corresponds to a small walk-off and weak focusing, the single pass efficiency γ_{shg} can be rewritten as

$$\gamma_{shg} = \frac{2w_1 d_{eff}^2 k_1^3}{\sqrt{\pi} n^5 \epsilon_0 c \rho} \arctan\left(\frac{l}{k_1 w_1^2}\right) \tag{2.33}$$

A plot of γ_{shg} as a function of the waist size and the crystal length is shown in figure 2.5. This has been calculated using the parameters of the LBO doubling crystal used in the experiment and the fundamental radiation at 778nm. The figure plots the dependence of the single pass efficiency γ_{shg} as a function of the crystal length and the waist size inside the crystal. It shows that there is waist size for which the function exhibits a local maximum as the crystal length increases. Even at optimum conditions γ_{shg} is very small - of the order of $1 \times 10^{-5} W^{-1}$. Consequently planar or confocal optical cavities are often used to enhance the power of the fundamental wave in the crystal to obtain optimum output at the second harmonic.

2.5 Optical Resonators and Enhancement

In this section we discuss some of the general points of the theory of wave propagation in optical resonators. In particular we discuss the properties of enhance-

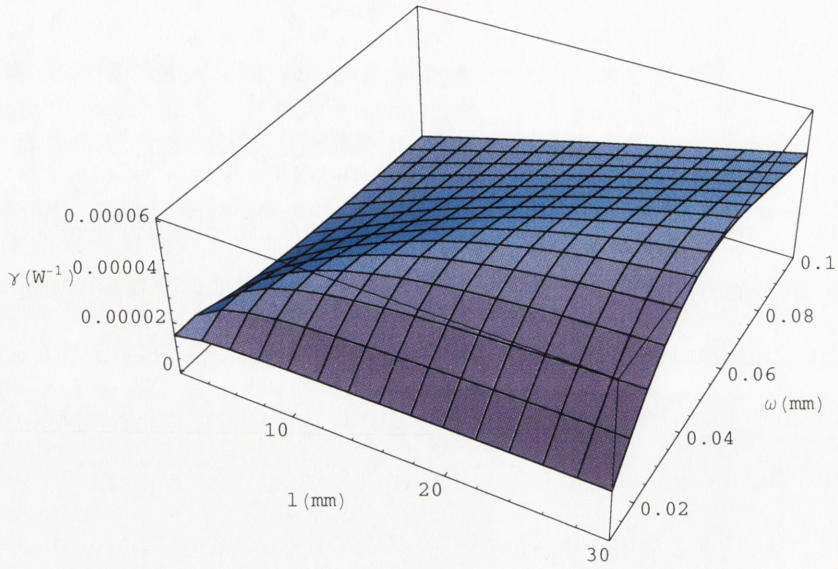

Figure 2.5: The single pass efficiency $\gamma_{shg}(\mathrm{W}^{-1})$ as a function of the crystal length $l(mm)$ and waist size $\omega(mm)$ for LBO at 778nm.

ment, frequency discrimination, how the enhancement plays a role in the doubling efficiency and some points on the choice of geometry. The fundamental operation of optical cavities in terms of power enhancement is a consequence of the superposition property of Maxwell's wave equations. In general an optical cavity consists of two or more highly reflective mirrors arranged so that the in-coupled light follows a closed loop, whereupon the beam properties are the same after one round trip. In such a cavity the propagation of a laser mode is the same as for free space, neglecting refractive index and dispersion due to the air, and phase changes and reflectivity losses with each of the cavity elements.

There are two types of commonly used cavities for frequency doubling of lasers. They are the standing wave and running wave cavities, the general features of which are shown in figure 2.6. To understand the operation of the enhancement cavity we calculate its response to an incident coherent field, derive the reflected and trans-

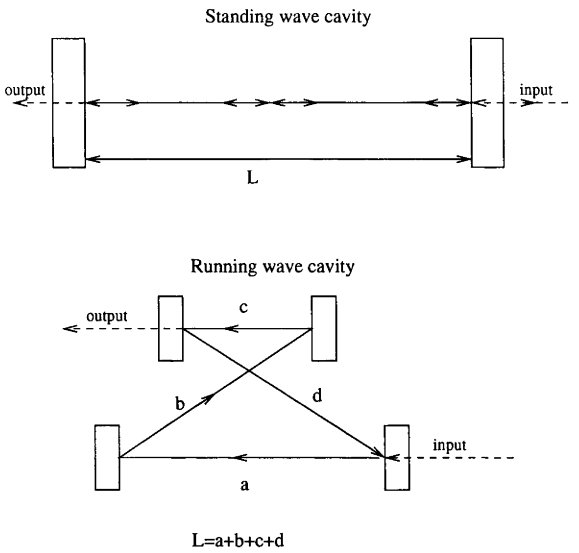

Figure 2.6: Schematic diagram of running wave and standing wave cavities

mitted fields and thus intensity. According to [19] a planar cavity is identical to a Fabry-Perot interferometer made up of flat mirrors with their separation fixed. The incident wave travels back and forth between the cavity mirrors which are highly reflective and which create a standing wave pattern, provided certain conditions are satisfied. The phase difference acquired by a wave in one round trip of the cavity can be written as

$$\begin{aligned} \phi &= \frac{2\pi}{\lambda} 2L + 2\delta \\ &= \frac{4\pi}{c} fL + 2\delta \end{aligned} \tag{2.34}$$

where f is the laser frequency in Hz. Here δ represents the phase change upon reflection. For the wave to reproduce itself, and assuming $\delta = 0$, the phase change must be an integral multiple of 2π thus

$$\phi = f\frac{4\pi L}{c} = 2\pi m \quad m = 1, 2, 3, ... \tag{2.35}$$

$$f = \frac{mc}{2L} \tag{2.36}$$

The second equation tells us that the frequency of the wave must be an integer multiple of the inverse of the cavity transit time. The frequency spacing between adjacent maxima is called the free spectral range (FSR) and is given by $f = \frac{c}{2L}$ for the planar cavity. The situation is only slightly different for the ring cavity and since the wave only traverses the cavity once before it reproduces itself, the FSR for this cavity is twice as large as for the planar case i.e. $f = \frac{c}{L}$. To calculate the transmitted and reflected intensity we first assume a coherent plane wave coupled to the planar cavity with electric field E_0 which has zero phase at the input. Immediately after the output mirror, the first and subsequent order transmitted electric fields are given by:

$$E_{t1} = E_0 t_1 t_2 e^{i\phi} \tag{2.37}$$

$$E_{t2} = E_{t1} r_1 r_2 e^{2i\theta} \tag{2.38}$$

$$E_{t3} = E_{t2} r_1 r_2 e^{2i\theta} = E_{t1} (r_1 r_2)^2 e^{4i\theta} \tag{2.39}$$

$$E_t = \sum_{l=1}^{\infty} E_{tl} = [E_0 t_1 t_2 e^{i\phi}] \sum_{m=0}^{\infty} (r_1 r_2)^m e^{2mi\theta} \tag{2.40}$$

$$= [E_0 t_1 t_2 e^{i\phi}](1 + r_1 r_2 e^{2i\theta} + (r_1 r_2)^2 e^{4i\theta} + (r_1 r_2)^3 e^{6i\theta} + ... \tag{2.41}$$

From this set of equations it can be seen that a pattern emerges. Here θ represents the acquired phase shifts between adjacent orders, and the t_1,t_2 are transmissions for the mirrors being related to the reflectivities r_1, r_2 by $t + r = 1$. The mirrors are assumed to be identical. The sum appearing can be turned into a geometric series, the result being [19]

$$E_t = E_0 e^{i\phi} \frac{t_1 t_2}{1 - (r_1 r_2) e^{2i\theta}} \tag{2.42}$$

The intensity transmitted normalised to the incident intensity is

$$T = |E_t|^2/|E_0|^2 \tag{2.43}$$

$$T = \frac{t_1^2 t_2^2}{1 - 2r_1 r_2 \cos 2\theta + r_1^2 r_2^2}$$

Here $R_1 = r_1^2$ where R_1 is the reflectance of element 1 and thus

$$t_1^2 = 1 - r_1^2 = 1 - R_1 = T_1$$

$$T = \frac{T_1 T_2}{(1 - \sqrt{R_1 R_2})^2 + 4\sqrt{R_1 R_2}\sin^2\theta}$$

The normalised reflected intensity is $1 - T$. Equation 2.5 gives the well known Airy function as a function of phase angle (related to frequency as $\theta = \frac{4\pi L f}{c}$) and is shown graphically in figure 2.7. The figure shows the dramatic redistribution of the energy

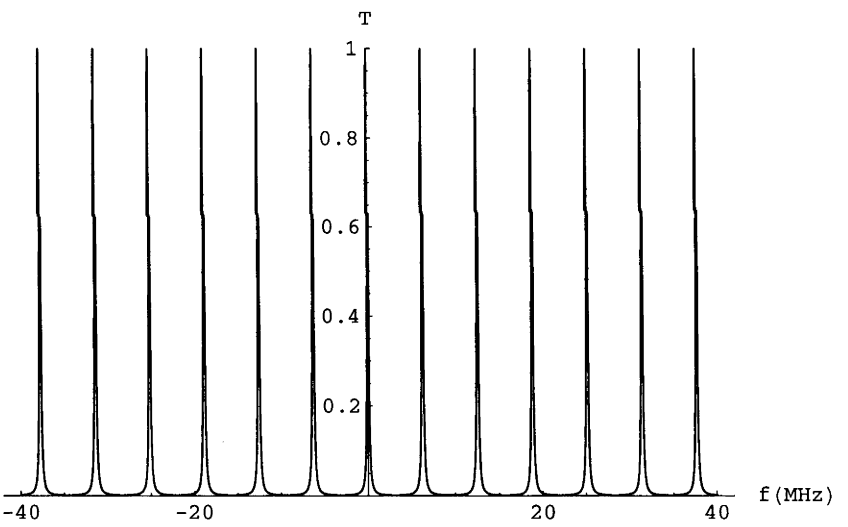

Figure 2.7: Cavity transmission T as a function of frequency f for R=0.92.

density centered on the cavity resonances. Experimentally T is always less than 1 since losses are inevitable. The resonances, as previously discussed, are separated by one FSR, and the ratio of the FSR to the full width at half maximum of the peaks is called the finesse $\mathcal{F}$. The finesse gives a measure of the average number

of round trips that a wave on resonance undergoes in the cavity before being lost. The equation for the finesse is given by [19]

$$\mathcal{F} = \frac{\pi\sqrt{R}}{1-R} \tag{2.44}$$

where $R = \sqrt{R_1 R_2}$ is the geometric mean of the mirror reflectances, and the total

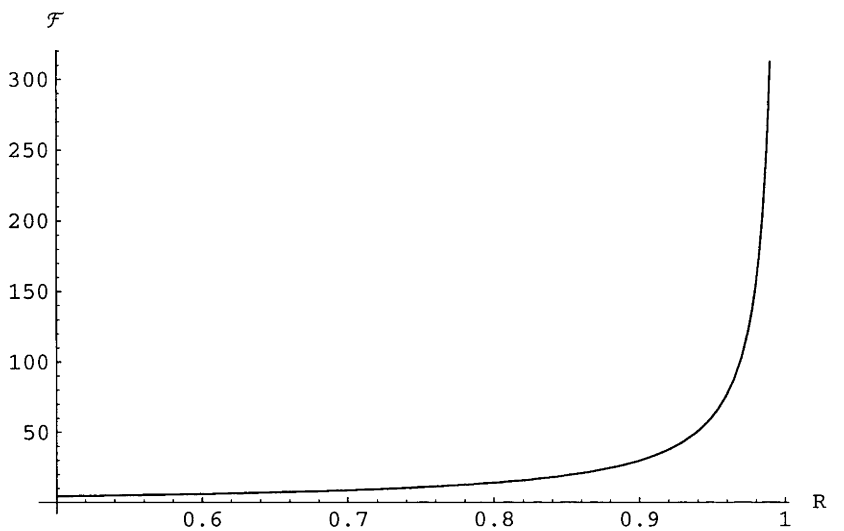

Figure 2.8: Cavity finesse as $\mathcal{F}$ a function of average reflectance R

losses in the cavity are just $1 - R$. These losses are entirely a result of transmission/absorption losses by the resonator mirrors. As can be seen from figure 2.8, the finesse is a sharp function of the mirror reflectance and is vital in determining the power enhancement in a cavity.

The previous discussion assumes monochromatic radiation, and experimentally the reflectance of the mirrors has a finite bandwidth that must be taken into account. Operation of the cavity using wavelengths outside this bandwidth range would result in a dramatic broadening of the peaks observed in figure 2.7, and a decrease in the enhancement of the electromagnetic field.

In the particular case of second harmonic generation, the use of an enhancement

cavity greatly increases the conversion efficiency by increasing the power entering the crystal. It was shown previously that the single pass efficiency γ_{shg} was rather small. On resonance inside the cavity according to [20] the power at the second harmonic $P_{2\omega}$ is

$$P_{2\omega} = \gamma_{shg} P_{\omega,c}^2 \tag{2.45}$$

$$P_{\omega,c} = \frac{T_1 P_\omega}{(1 - \sqrt{R_1 R})^2}$$

In this equation $T_1 = 1 - R_1$ is the transmission of the input coupler while R in this case is the mean reflectivity of the remaining cavity elements. It can be seen that in a situation of moderate enhancement, where for example $T_1 = 0.02$ and $R = 0.975$, then $P_{\omega,c}/P_\omega \approx 40$ is creating an increase in the converted power of $40^2 = 1600$. The choice of reflectivity for the input mirror $R_1 = 1 - T_1$ affects the enhancement factor and is called impedance matching, in analogy with electrical circuits since there is a trade off between power entering and leaving the cavity through the input coupler. It determines the amount of power that is coupled into the cavity on resonance. The enhancement is at maximum whenever the input coupler reflectivity T_1 equals the mean reflectivity R and increases sharply if both T_1 and R approach unity.

The expression for $P_{\omega,c}$ only applies in situations where the fraction of converted power is small (undepleted pump approximation). At higher powers the losses due to conversion must be taken into account which changes the dependence of the converted power on the input from quadratic to eventually linear [21]. This enters through the mean cavity reflectivity R as in equation 2.5. In the case of a non-linear crystal in a four mirror ring cavity resonator, $R = R_2 R_3 R_4 T_{crystal} T_{shg}$ where $T_{crystal}$ is the linear transmission through the crystal and $T_{shg} = 1 - \gamma_{shg} P_{\omega,c}$ is the non-linear transmission that depends on the fraction of converted power. If T_{shg} becomes large then the relation for $P_{\omega,c}$, is complicated and would need to be solved numerically.

The choice of cavity is dependent on the requirements of the application. In the context of second harmonic generation, most authors have used a ring cavity [20],

[21], [22], [23], [24], [25]. Various configurations have been employed but most use curved focusing mirrors arranged off-axis as two of the elements. When choosing a cavity configuration the main factors that need to be considered are the physical dimensions (which influence the mechanical/thermal stability and thus the ultimate linewidth), the conversion efficiency and the output beam quality. These properties are all interrelated, but in practice one chooses the highest priority and this determines the cavity geometry.

Standing wave cavities are chosen over ring cavities most commonly in cases requiring compactness. They can even be made monolithic i.e. as a part of the lasing medium or doubling crystal, by applying multilayer coatings on the input and output faces of the crystal [26]. This also makes cavity more mechanically stable, reducing the requirements for frequency stabilization since the lasing/doubling element is commonly rigid. Standing wave cavities also eliminate the astigmatism/ellipticity introduced by the use off axis reflections in a ring cavity.

The main advantages of using a ring cavity is that the reflected intensity at the input coupler (also used for frequency locking) is not directed back toward the input laser which may disturb its frequency stability. The amount of back reflection is a lot smaller than for a standing wave cavity. Input and output coupling is simpler because flat optical elements can be used, making alignment easier, since in practice standing wave cavities do not use totally flat mirrors due to the geometry being unstable and difficult to align. In a standing wave cavity, linear losses through the active element are also twice as large as for a ring cavity due to waves traveling in both directions, which also leads to an overall reduction in conversion. For the same reason, in a ring cavity the doubled radiation that is to be extracted travels uni-directionally rather than being emitted equally in opposite directions in a standing wave cavity. Ring cavities, however, are generally mechanically less stable and require extensive active frequency stabilisation to maintain optimum cavity length.

In the experiment decribed here a ring cavity has been employed on the basis

of its high conversion efficiency to realise a source of UV radiation for use in He* atom optics experiments. The initial goal of my work on the system was to stabilise both the frequency and output intensity of the ring cavity. The following chapters describe the characteristics and optimisation of this system.

CHAPTER 3

Experimental Setup of 389nm source

The focus of this thesis is the development and improvement of an existing laser frequency doubling system which produces tunable UV radiation at 389nm for the excitation of the $2^3S \rightarrow 3^3P$ transition of helium. The system consists of a Ti:Sapphire laser operating in single mode at a wavelength of 778nm with sub-megahertz linewidth. The external frequency doubling cavity resonator has a confocal configuration with a LBO crystal as the frequency doubling element. Frequency doubling occurs most efficiently when the cavity length is resonant with the input radiation, due to a build up of the circulating power. A fraction of the circulating fundamental is converted into the second harmonic. The small single pass conversion efficiency given by the parameter γ_{shg} makes the use of an external cavity resonator necessary. Once adequate stable power is produced, a part of the 389nm light was used to lock the frequency of the laser to one of the 3^3P_j excited states, using saturated absorption spectroscopy described in more detail in the Chapter 6. The final setup is shown schematically in figure 3.1 and the main elements described in the following sections.

3.1 The Cavity

The main part of the experiment is the external frequency doubling cavity shown in 3.1 which had been built and developed by previous students [27], [28]. A similar

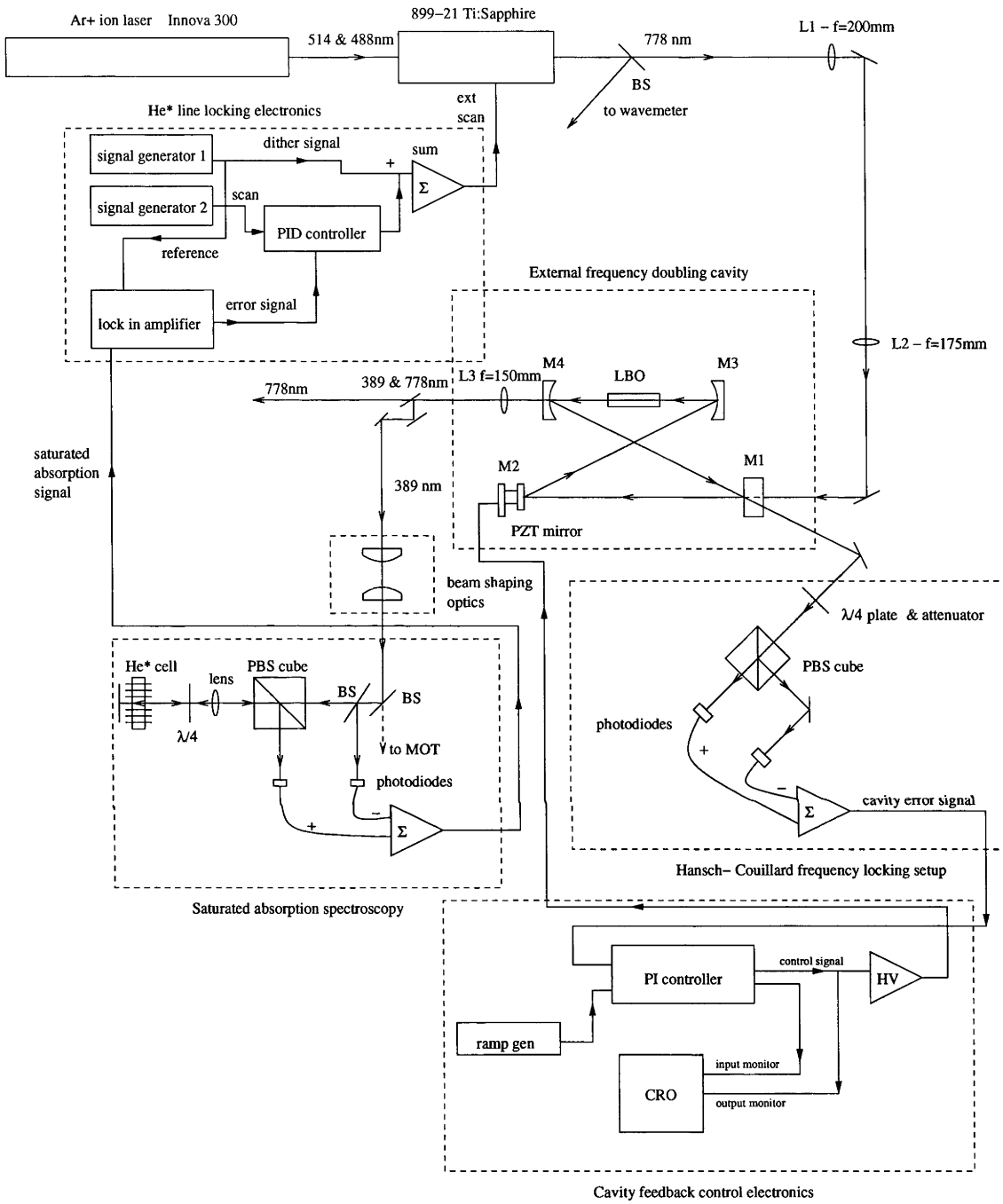

Figure 3.1: The experimental setup of the 389nm external frequency doubling cavity and control systems. Legend: BS - beamsplitter, L - lens, M - mirror, PBS - polarising beamsplitter, HV - high voltage amplifier, $\lambda/4$ - quarter wave plate, PZT - piezotransducer, CRO - oscilloscope, Σ - summing amplifier, LBO - lithium triborate crystal

setup was used at the Stony Brook University, NY [29]. Here I transcribe the main features of their analysis, in particular towards the design of the cavity.

3.1.1 General arrangement

The main priority in the design of this system was doubling efficiency, thus a running wave cavity was used. The doubling cavity consists of two plane mirrors and two plano-concave focusing mirrors ($f = 50$ mm) arranged as a confocal resonator in a bow-tie arrangement as shown in Figure 3.2. The fundamental light is coupled

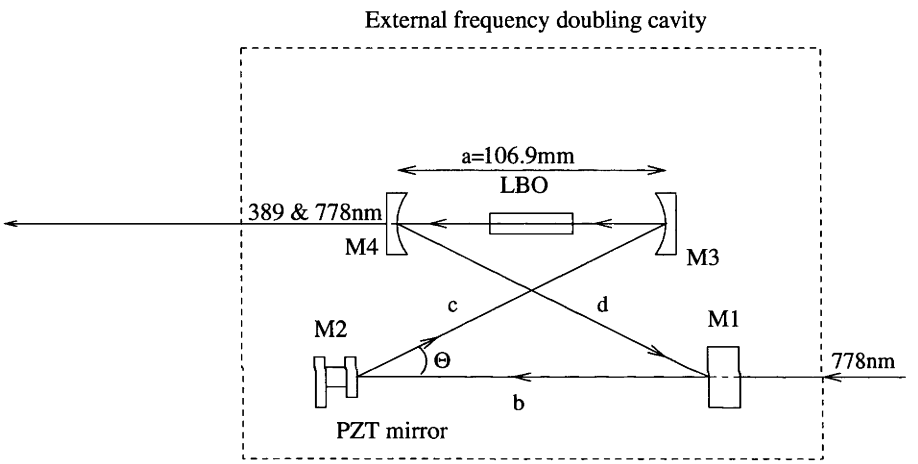

Figure 3.2: Geometry of bow-tie doubling cavity

in through the planar mirror M1 and follows a path shown by the arrows in the figure. It traverses the distance $L = a + b + c + d$ before reproducing itself after one cavity round trip. Planar mirror M2 is mounted on top of a piezo-electric translator (PZT) which enables the length of the cavity to be scanned, and is tilted at an angle $\Theta = 6^o$ in the plane of the cavity that defines the tangential plane. Frequency doubling occurs inside an 18mm long LBO crystal with end faces cut perpendicular to the direction of the laser beam which have been anti-reflection (AR) coated for both the fundamental and second harmonic. It is placed at the focal point of the

two focusing mirrors M3 and M4 where the intensity of the beam is at maximum. The use of perpendicular AR-coated end faces simplifies alignment and reduces astigmatism introduced by the use of a Brewster cut crystal. The curved mirror M4 is the output coupler from which the second harmonic and a very small fraction of the fundamental escapes the cavity. All mirrors are coated with a high reflective (HR) dielectric coating designed to have the highest reflectivity for the fundamental radiation at 778nm for light polarised in the direction of the saggital (vertical) plane and at near normal angles of incidence.

The mirrors have been mounted in gimbal mounts with three degrees of freedom: rotation in the tangential and sagittal planes, as well translation along the axis of the beam. The mounts sit on shortened posts and bases which have been glued with Araldite to a solid block of granite which sits on several thick sheets of rubber foam to isolate the cavity from mechanical vibrations. The whole arrangement is enclosed in a specially made perspex housing for further isolation from vibrations and air currents.

Performance of the doubling cavity in terms of the conversion to the second harmonic is determined by the beam parameters inside the cavity. Firstly, the beam size at the focus between the mirrors M3 and M4 has to be of a particular size given by equation 2.33. This has to be satisfied for every round trip cycle that the beam completes. Secondly, the coupling between the input laser and the lowest order eigenmode TEM_{00} of the resonator needs to be maximised. This determines the amount of light that enters the cavity on resonance independent of impedance matching. Finally, the number of roundtrips that the beam undergoes before being lost to leakage through the mirrors or conversion to the second harmonic has to be maximised.

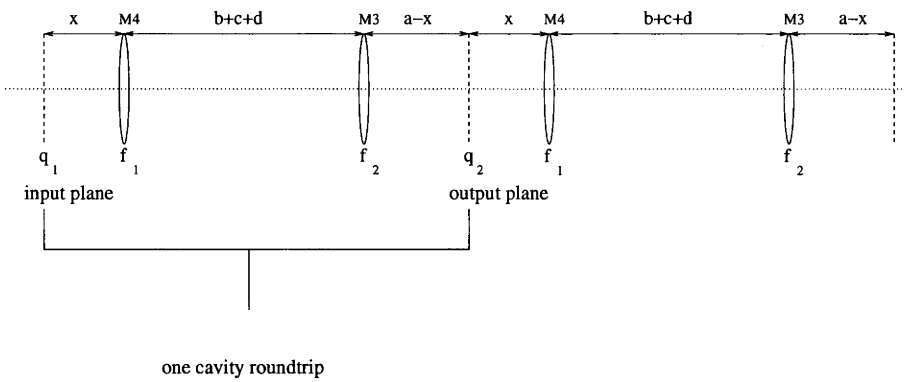

Figure 3.3: The doubling cavity represented as a repeating sequence of lenses

3.1.2 Cavity Design

To calculate the beam parameters inside the cavity according to [17] it is possible to unfold any arbitrary resonator into a linear path, all the focusing elements being replaced by a repeated sequence of lenses that enable calculation of the resultant ray transfer matrix. Thus the beam parameter along any point in the round trip can be evaluated. The unfolded cavity is shown in figure 3.3. For our particular system the ray transfer matrix for one round trip beginning anywhere along the path before the output coupler M4 would be

$$\begin{pmatrix} A & B \\ C & D \end{pmatrix} = \begin{pmatrix} 1 & a-x \\ 0 & 1 \end{pmatrix} \cdot \begin{pmatrix} 1 & 0 \\ -1/f_2 & 1 \end{pmatrix} \cdot \begin{pmatrix} 1 & b+c+d \\ 0 & 1 \end{pmatrix} \cdot \begin{pmatrix} 1 & 0 \\ -1/f_1 & 1 \end{pmatrix} \cdot \begin{pmatrix} 1 & x \\ 0 & 1 \end{pmatrix} \tag{3.1}$$

$$= \begin{pmatrix} 1+x(\frac{xL}{f_1 f_2} - \frac{1}{f_1} - \frac{1}{f_2}) - \frac{L}{f_1} & L+x-\frac{xL}{f_2} + (a-x)(1-\frac{x}{f_1} - \frac{x}{f_2} - \frac{L}{f_1} + \frac{Lx}{f_1 f_2}) \\ -\frac{f_1+f_2}{f_1 f_2} + \frac{L}{f_1 f_2} & 1 - \frac{L}{f_2} + (\frac{L}{f_1 f_2} - \frac{1}{f_1} - \frac{1}{f_2})(a-x) \end{pmatrix}$$

Here $L = b + c + d$ is the path length in the cavity that excludes the distance between the two curved mirrors. For a resonator to be stable, the beam must be periodically refocused along its path. This implies a condition for maximal cavity

round trip length L_{max} to be

$$L < L_{max} = \frac{a(f_1 + f_2)}{a - f_1 - f_2} \tag{3.2}$$

The mathematical manifestation of this stability criterion is that any power of the ray transfer matrix will be finite. This means that the system will reproduce itself after an arbitrary number of round trips. Because the cavity uses mirrors inclined at an angle θ, the curved mirrors M3 and M4 have different focal lengths in the two planes and consequently there are two transfer matrices. One is for the tangential plane which is in the plane of the ring, and one for the sagittal plane which is perpendicular to it. The effective focal lengths for the two planes are

$$\begin{aligned} f_t &= f \cos\theta \\ f_s &= \frac{f}{\cos\theta} \end{aligned} \tag{3.3}$$

In our cavity the two mirrors have the same focal lengths $f = 50mm$ and thus the cavity is symmetric. The output beam properties after one round trip can then be calculated using the ABCD law of equation 2.23. We set the input and output beam parameter $q_2 = q_1$ which gives the spot size of the cavity mode at that position according to [30] as

$$\frac{\pi w^2}{\lambda} = \frac{2|B|}{\sqrt{4 - (A + D)^2}} \tag{3.4}$$

and the waist to be

$$\frac{\pi w_0^2}{\lambda} = \frac{\sqrt{4 - (A + D)^2}}{2|C|} \tag{3.5}$$

with the location of the waist relative to the input plane

$$z = \frac{A + D}{2C} \tag{3.6}$$

The waist is located halfway between the two focusing mirrors in both planes. The cavity has also been designed to give a circular beam at the focus i.e. the waists in

the two planes are equal $w_0^t = w_0^s$. This was achieved by an appropriate choice of the distance L so that

$$L = \frac{1}{2\alpha}(-\beta \pm \sqrt{\beta^2 - 4\alpha\gamma}) \tag{3.7}$$

$$\alpha = 2\sigma a - 2f(1+\sigma^2)$$

$$\beta = 2f(\sigma R - a(1+\sigma^2))$$

$$\gamma = 4\sigma a f^2$$

$$\sigma = \cos\theta$$

An additional element needs to be inserted into the ray transfer to account for the change in refractive index inside the crystal. The type of phase matching used in the experiment is type I so that there is only one refractive index for the fundamental radiation. This matrix is given by

$$\begin{pmatrix} A & B \\ C & D \end{pmatrix} = \begin{pmatrix} 1 & l/n \\ 0 & 1 \end{pmatrix} \tag{3.8}$$

where l is the length of the crystal. The effect of the crystal is to increase the optical path length. Thus the focii in the center of the crystal will not coincide unless the physical distance a is decreased to $a = a' - l(1-1/n)$ where $n = 1.61$ is the refractive index. We used a 18mm long LBO crystal for which the ideal spot size which gives the maximum conversion efficiency is $w_0 = 31.5\mu m$. The dimensions of the cavity to produce a circular waist of this size at the center of focus are

$$a = 107 \text{ mm} \tag{3.9}$$

$$L = b + c + d = 713 \text{ mm}$$

$$\theta = 6^o$$

The spot size in the cavity halfway between the two plane mirrors is calculated to be $w_t = 311\mu m$ and $w_s = 283\mu m$.

3.1.3 Mode Matching

The desired cavity parameters listed in the previous section enable the alignment and optimisation to be performed. To maximise the power entering the cavity via mirror M1 both good alignment and good mode matching needs to be achieved.

Mode matching refers to transforming the laser mode to the lowest order TEM_{00} cavity eigenmode which has the dimensions quoted previously. Otherwise only a small fraction (given by spatial overlap of the two modes) of the input power will be coupled into the cavity. According to [24] the enhancement factor can be written as $S = \eta\kappa$ where η is the mode matching factor.

Mode matching is done by using a lens external to the cavity, or by using a pair of lenses to form a telescope giving the correct spot size. The choice of lens requires that the focal length f has to be greater than the characteristic length f_0 given by

$$f_0 = \frac{\pi w_c w_l}{\lambda} \tag{3.10}$$

The distances d_c and d_l from the lens to the cavity waist w_c and from the lens to the waist of the laser w_l are given by [17]

$$\begin{aligned} d_c &= f \pm \frac{w_c}{w_l}\sqrt{f^2 - f_0^2} \\ d_l &= f \pm \frac{w_l}{w_c}\sqrt{f^2 - f_0^2} \end{aligned} \tag{3.11}$$

Laser waist sizes and positions needs to be determined by measurement while the cavity waist and positions are quoted in the previous section. Furthermore, since there are two astigmatic beams that need to be matched to each other, a combination of cylindrical and spherical lenses is required to achieve optimum mode matching. Optimum mode matching in conjunction with the high reflectivity of the mirrors enables a high circulating power to be generated in the cavity and consequently highest second harmonic power.

3.1.4 LBO crystal

The frequency doubling element in our cavity is a 3x3x18mm crystal of lithium triborate (LiB_3O_5) obtained from Castech. It has been cut at the phase matching angle for our pump fundamental wavelength at 778nm with flat end faces perpendicular to the beam direction. The end faces are AR coated for both fundamental and second harmonic with manufacturer's quotes for the linear losses (at low incident power thus low conversion to the second harmonic) being 0.25% and 2% at the respective wavelengths.

The crystal is a negative-biaxial crystal and we use type I $ee \rightarrow o$ (fundamental waves polarised in e-axis, second harmonic in o-axis) phase matching by angle tuning the crystal's ϕ axis which is in the tangential plane of the cavity. For this purpose the crystal is mounted in a special holder made of copper (for good heat conduction) that is mounted on top of a New Focus three-axis translational stage. The stage enables rotation about the crystal's ϕ and longitudinal axes as well as one translational adjustment. A thin piece of indium foil provides good thermal contact between the crystal and the copper block to reduce the effects of heating by the 778nm beam.

The choice of LBO is due to several advantages it has over other doubling crystals. Other suitable materials for SHG of Ti:Sapphire lasers are lithium iodate ($LiIO_3$), β – barium borate (BBO) and pottasium niobate ($KNbO_3$). Pottasium niobate is unsuitable for operation at 778nm because phasematching by temperature tuning can only be done down to 838nm, due to a phase transition in the crystal below T=-36° [24]. Authors favour LBO in this wavelength regime [23], [25], [24] on the basis of its moderately high non-linear coefficient, small walk-off angle compared to BBO and $LiIO_3$, large angular acceptance and the highest damage threshold. The main crystal properties are shown in table 3.1.

The refractive indices were calculated using the Sellmeier equations for BBO and $LiIO_3$ [31] at 778nm. Subsequently, the phase matching angle and walk off were

Crystal	BBO	$LiIO_3$	LBO
n	1.54	1.73	1.61
phase-matching angle (deg) type I ee $\rightarrow$ o	30.36	44.42	$\phi = 33.8$, $\theta = 90$
walk-off (mrad)	65	80	17
d_{eff} Definition	$d_{22}\cos\theta$	$d_{31}\sin\theta$	$d_{32}\cos\phi$
d_{ij} (pm/V) Definition	$d_{22} = 2.22$	$d_{31} = -1.41$	$d_{32} = 1.17$
d_{eff} (pm/V)	1.92	2.86	1.00
Damage threshold GW/cm^2	5	0.5	10
$\gamma_{sh}(10^{-5}\mathrm{W}^{-1})$	5.31	5.38	4.41

Table 3.1: Comparison of three crystals for frequency doubling at 778nm

calculated using the phase matching formula for negative uniaxial crystals given by [32] respectively:

$$\sin\theta_{pm}{}^2 = \left(\frac{n_\omega^e}{n_{2\omega}^o}\right)^2\left[\frac{(n_{2\omega}^o)^2 - (n_\omega^o)^2}{(n_\omega^e)^2 - (n_\omega^o)^2}\right] \tag{3.12}$$

$$\rho = \arctan\left(n_o/n_e\right)^2 \tan\theta_m - \theta_m$$

These numbers, along with the corresponding effective non-linear coefficients d_{eff} [24], were used to calculate the single pass conversion efficiencies γ_{sh} for each crystal using equation 2.32. The experimental crystal size (18mm) and a $31.5\mu m$ waist were used in the calculation.

At first glance it might seem that $LiIO_3$ would be the best choice because it has the highest γ_{sh}. However, the high walk-off and low damage threshold make this crystal unsuitable for focused laser beams. The crystal is also highly hygroscopic, requiring a constant nitrogen purge which makes the surface quality more difficult to maintain. This is important since degradation would contribute to losses in the cavity. The acceptance angle which is given by the inverse slope of the phase matching curve vs. wavelength, provides an indication of the range of wavelengths that can be accessed for one crystal cut. BBO has similar doubling efficiency to

$LiIO_3$ at this wavelength, but its main drawback compared to the other two crystals is its small acceptance angle and high angular sensitivity which makes alignment more stringent [25]. BBO and $LiIO_3$ have much larger walk-off angle than LBO, which increases the astigmatism in the output beam as well decreasing the average power attainable due to a smaller aperture length. The aperture length gives the effective length over which the fields exchange energy in the crystal as given by $l_a = \frac{\sqrt{\pi} w_0}{\rho}$. Consequently, longer crystals would be required for BBO and $LiIO_3$ to achieve same average powers as LBO due to a higher walk-off. Furthermore LBO has the highest damage threshold of all the crystals, which makes it preferable in high power applications.

3.2 Ti:Sapphire laser

The source laser used in our experiment consists of the commercially available Coherent Innova 300 Argon ion pumping a Coherent 899-21 Ti:Sapphire. The Argon laser emits at many lines in the visible the strongest of which are at 488 and 514nm with a maximum cw power of 10W. The Ti:Sapphire ring laser converts this power into tunable radiation from 700-1100nm in the near infrared.

The active element in the ring laser is a Brewster cut $Ti:Al_2O_3$ crystal which is placed at the focus of two focusing mirrors that along with a third mirror and output coupler, form the ring cavity. Water cooling is provided to the laser crystal via temperature controlled chiller and the temperature maintained at 14^oC during operation. It was used in single frequency scanning mode (narrow band) with both thick and thin etalons installed, together with a scanning Brewster plate and proprietary external reference cavities. The external cavities compare the transmitted intensity to a normalising photodiode and extracts an error signal which is used to lock the frequency of the laser. The signal is used to correct for fast changes (up to 50kHz) in cavity length via the PZT mounted on mirror M2 [33]. Frequency

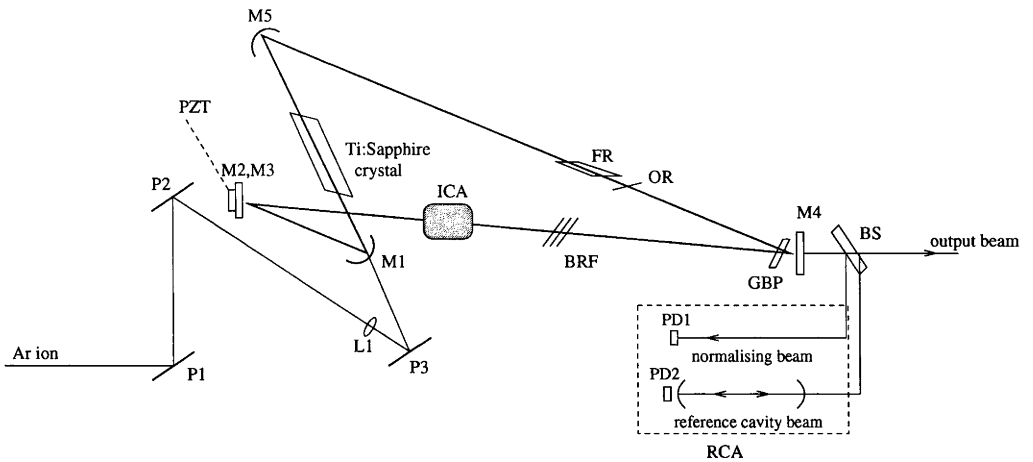

Figure 3.4: Schematic of Coherent 899-21 Ti:Sapphire laser. Legend : P1,2,3 - pump mirrors; L1 - lens; M1,2,3,4,5 - ring cavity mirrors; FR - Faraday rotator; OR - optical rotator; BRF - birefringent filter; ICA - intra-cavity assembly; RCA - reference cavity assembly; GBP - galvo-driven Brewster plate; PZT - piezo stack transducer; PD1,2 - photodiodes; BS - beamsplitter.

scanning and locking to the reference cavities is performed via the external control box. The optical diagram of the Ti:Sapphire is shown in figure 3.4

Wavelength tuning in the laser is performed by three main frequency selective elements inside the cavity. Coarse tuning is provided by the birefringent filter (BRF) which consists of three plates made of crystalline quartz mounted at Brewster angle to the forward beam. It operates by introducing losses for wavelengths not satisfying the Brewster criterion. The laser can be operated with only this frequency selective element when it is in broadband configuration with a linewidth of 2GHz. The thick and thin etalon are part of the intracavity assembly (ICA) that are installed when running the laser in narrowband configuration. The thick etalon is a Fabry-Perot cavity that consists of two identical prisms mounted on PZT's with a free-spectral range of 10GHz. The thin etalon is a quartz plate mounted on a galvanometer for tuning the angle at which the beam strikes it. Fine tuning of the laser frequency is performed by rotating the thin etalon offset control on the control box, which

changes the frequency by up to 10 GHz. With these elements installed the laser is forced to run in a single longitudinal mode and the linewidth is reduced to 20MHz. There is also a galvanometer mounted Brewster plate at the apex of the ring that compensates for changes in the path caused by the ICA, and also corrects for low frequency jitter. With all these components in place, the frequency of the laser can be scanned through 30GHz with minor variations in power. The final linewidth is quoted as below 500 kHz [34], with external reference cavities installed and locked to the peak of one of the external cavity modes.

The output mode is a nearly perfect Gaussian TEM_{00} mode, linearly polarised in the vertical direction with an approximately 300 μm waist size at the exit face of the laser. The beam is slightly astigmatic with an average aspect ratio of 1.2 and full angle divergences of 0.4 mrad in the horizontal and 1.46 mrad in the vertical dimensions respectively, as measured using a BeamScan beam profiler. The output power was measured using a calibrated Newport 8440 series meter with 818SL series head; the highest output power achieved was 1.1 W at 10W pump power. Typical running powers were 550-600mW at 8W pump power. Intensity noise on the output was measured to be of the order of 5% peak-to-peak measured over many minutes using a photodiode. The peak power had to be adjusted from day to day by adjusting the focusing to the crystal, the BRF and thin etalon offset. The power and detuning was found to drift, within 1-2 hours the power droped by 30% and the wavelength changed by 1-2 nm requiring this to be constantly readjusted. Wavelength monitoring was implemented by splitting off some of the light and directing it into a fibre optic coupled to a Burleigh WA-1100 wavemeter that gave an accuracy of ± 0.001 nm.

The power and stability of the Ti:Sapphire laser was absolutely crucial in determining the performance of the doubling cavity. Since the output power at 389nm scales as the square of the input, small decreases in input power would nonlinearly degrade the output power. The linewidth of the laser was not an issue since it is

much smaller than the observed doubling cavity linewidth of ≈3 MHz. Short term fluctuations in the detuning between the laser and the cavity mode frequency introduced intensity fluctuations in the output. Rotation of the polarisation from the optimal direction can also decrease the performance of the cavity since less light would enter the cavity and would upset the cavity locking circuit. Intensity noise in the laser output also manifests itself in the doubled laser output. Since the output power is dependent as the square of the input power, the variation of the input power is manifested as a variation of the output power as:

$$P_{2\omega} = \gamma_{sh} P_{\omega}^2 \tag{3.13}$$

$$dP_{2\omega} = 2\gamma_{sh} P_{\omega} dP_{\omega}$$

$$\frac{dP_{2\omega}}{P_{2\omega}} = 2\frac{dP_{\omega}}{P_{\omega}}$$

It can be seen that the relative power fluctuation in the UV output is double the variation in the input power e.g. a 5% intensity noise at the fundamental tranlates to a 10% intensity noise at 389nm. This places a fundamental limit on the doubling cavity stability without some sort of intensity stabilisation of the Ti:Sapphire laser.

3.3 Cavity locking

Efficient production of the second harmonic output relies on the external doubling cavity being resonant with the input radiation. This requires that the optical path length inside the cavity be precisely controlled and maintained to much less than $\lambda/\mathcal{F} = 7$ nm of one of the cavity resonances. This maximises field coherence (and thus input coupling and power enhancement) and reduces the intensity fluctuation of the output radiation.

Control of the cavity length is performed by translation of the mirror M2 which is mounted on a PZT stack and glued on a mirror mount. The PZT changes its length when voltage is applied across its terminals via the piezoelectric effect. The voltage applied to the PZT has to be such that it cancels the disturbances in the

surrounding environment that would otherwise move the cavity out of resonance. This is commonly referred to active frequency stabilization, as opposed to passive methods which involve isolation from the environment.

There are several techniques for frequency stabilisation of optical cavities, each of which involve the generation of an appropriate error signal that is sent to the control element. The relative merits of each can be compared in terms of the properties of the generated error signal. That is its sensitivity usually in terms of (MHz/V) and magnitude relative to the noise due to electronics and other external influences i.e. it's signal-to-noise ratio. This largely determines its ability to maintain the system in its desired state on both long and short timescales.

One relatively simple method utilises the transmission properties of an external Fabry-Perot (FP) cavity to lock the frequency of a laser to one side of the FP fringes [35]. The schematic is shown in figure 3.5. The system works by splitting a part of the output beam which is sent through a stabilised FP. The FP is tuned through the PZT mounted mirror to the position where the transmitted intensity is half the maximum. Since the transmission will depend on both the frequency and the intensity of the input beam, a second part is split off to serve as a intensity reference. The signals are detected by two photodiodes and fed to a differential amplifier that provides the error signal to the electronics controlling the laser cavity length. This is in fact the same locking method as used in our Ti:Sapphire laser. The error signal is the offset FP transmission curve the calculation of which is presented in figure 3.6.

When the laser frequency drifts, the voltage at the output of the differential amplifier moves away from the lock point, which in figure 3.6 is set at zero. The driving electronics then respond by feeding a signal that is proportional to this change that has an appropriate phase to make this voltage zero. A mechanical analogy can be made whereby the size of the error signal is equivalent to the size of the restoring force. The advantage of this system is its simplicity, and it can

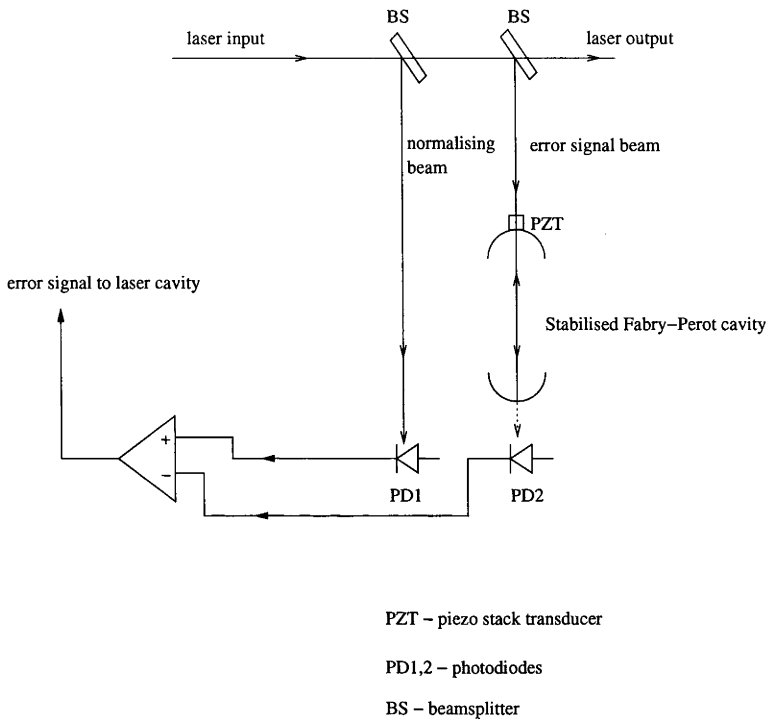

Figure 3.5: Schematic of the side fringe lock method

potentially be made to respond over a large bandwidth. The disadvantage is that the FP cavity is susceptible to thermal drifts which would cause a long term drift in the cavity frequency. Secondly it is not possible for the system to be locked at the maximum of the transmission fringe with this technique, which is desirable for our external doubling cavity because the peak of the transmission corresponds to the peak second harmonic power.

The slope on the side of the fringe (MHz/V) gives the sensitivity of this particular technique. Another notable parameter is the capture range which conveys how far the system can drift and still be brought back to the desired lock point. If an accidental frequency jump puts the system in figure 3.6 somewhere in the shallow part of the FP curve, then the system is likely to mode hop across one spectral range. Due to the great sensitivity at high finesse, the system is likely to perform

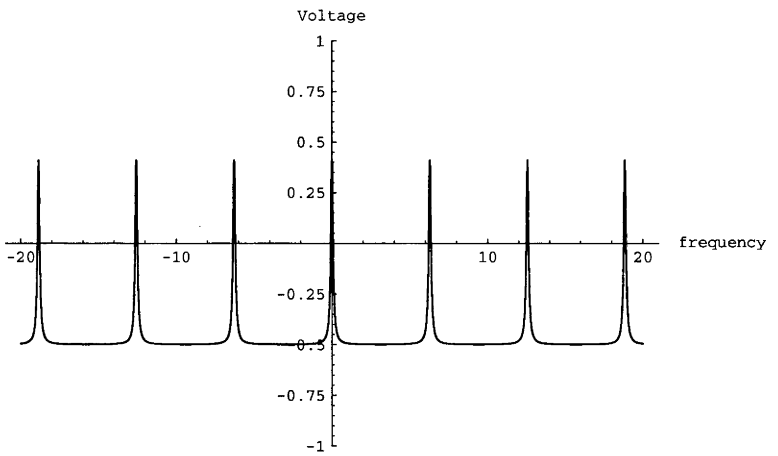

Figure 3.6: Error signal generated by fringe side method

successive mode hops, so subsequently low finesse cavities are used with this locking method (e.g. the Ti:Sapphire laser used in the experiments). In this case a higher finesse of the FP cavity decreases the locking bandwidth, but increases the capture range.

Other methods involve dithering the laser frequency internally via one of the cavity mirrors [36] or externally via an electro-optic modulator (EOM) or acousto-optic modulator (AOM) as in the Pound-Drever-Hall method. Both of these schemes involve generating sidebands to the laser output frequency and monitoring the reflection from or transmission through a reference cavity. The detected signal is then extracted through phase sensitive detection at the modulation frequency. The advantages of this system are: (1) the sensitivity can be varied by varying the modulation frequency but this comes at the expense of the capture range; (2) it is possible to lock to the peak of a resonance (rather than the side); and (3) that it is insensitive to intensity noise to first order since it uses AC detection. The main disadvantages are that the error signal can be complicated [33], and the associated electronics are also elaborate greatly increasing the noise present in the control loop.

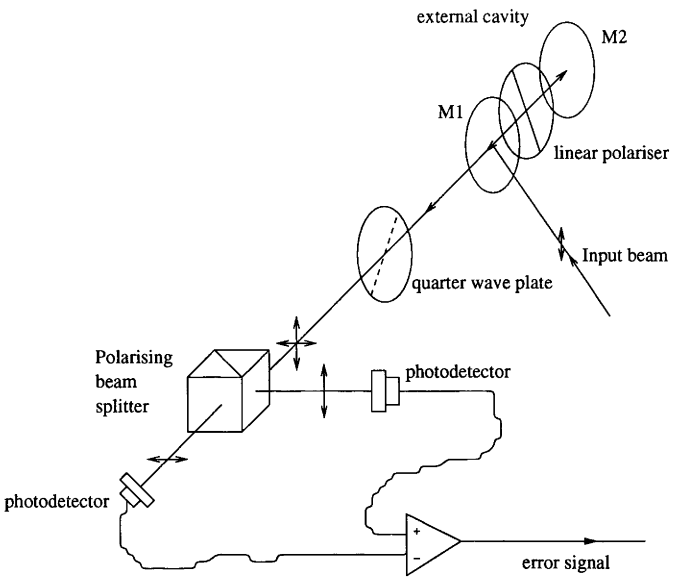

Figure 3.7: Schematic setup of Hansch-Couillaud locking scheme as used in the 389nm frequency doubled laser

The reflection techniques give the highest possible bandwidth because the cavity introduces a maximum phase shift of 90 degrees at high frequencies.

With some of these considerations in mind the scheme implemented in our experiment is the Hansch-Couillard [37] technique (also called the Pound-Hansch method). It uses the polarisation of a reflected beam from a cavity to derive an error signal. It produces a signal with a very sharp resonant slope at the peak cavity resonance as well as broad dispersive wings enabling a wide capture range. It also does not require modulation to be introduced to the laser or the external cavity.

The schematic of the laser locking system is shown in figure 3.7. This is the optical analogue of a scheme introduced by Pound in 1946 for microwaves. It works on the principle that an optical cavity that contains a polarising element has a different round trip loss depending, on the polarisation of the input radiation. The cavity has a preferred polarisation for which the losses are low. The polariser in the cavity is rotated so that its pass axis is nearly parallel to the polarisation of the incoming beam. Thus in the scalar approximation the incident amplitude E^i can

be split into two components

$$E^i_{||} = E^i \cos\theta \tag{3.14}$$
$$E^i_{\perp} = E^i \sin\theta$$

θ being the angle of the incident polarisation relative to the pass axis of the polariser.

At the input coupler M1 the perpendicular component gets reflected so its amplitude $E^r_{\perp}$ is [37].

$$E^r_{\perp} = E^i_{\perp}\sqrt{R_1} \tag{3.15}$$

Here $R_1 = 1 - T_1$ is the reflectivity of the input mirror M1. The parallel component sees a cavity of low loss and undergoes a frequency dependent phase shift δ after completing one round trip. Thus the amplitude $E^r_{||}$ of reflected wave is

$$E^r_{||} = E^i_{||}\{\sqrt{R_1} - \frac{T_1}{\sqrt{R_1}}\frac{Re^{i\delta}}{1 - Re^{i\delta}}\} \tag{3.16}$$
$$= E^i_{||}\{\sqrt{R_1} - \frac{T_1 R}{\sqrt{R_1}}\frac{\cos\delta - R + i\sin\delta}{(1-R)^2 + 4R\sin^2\delta/2}\}$$

Here $R < 1$ is the amplitude ratio between successive round trips. When the cavity is on resonance ($\delta = 2m\pi$) the two waves are in phase (second line of equation 3.16 is real), and the two polarisations add to give a circularly polarised beam. When the two waves are out of phase the polarisation is elliptical, whose handedness depends on the detuning from resonance. The light travelling toward the detectors passes through a $\lambda/4$ plate whose fast axis is rotated at $\theta = 45^o$ to the polarising axis of the beam splitter cube. The $\lambda/4$ transforms the elliptically polarised light back into two linearly polarised beams whose intensity is equal when the incoming polarisation is circular. The polarising beam splitter cube splits this beam into two beams of linear polarisation whose relative intensities are used to balance two photodetectors. The error signal for this locking scheme is [37]

$$I_a - I_b = 2I^i \cos\theta \sin\theta \frac{T_1 R \sin\delta}{(1-R)^2 4R\sin^2\delta/2} \tag{3.17}$$

Here $I^i = \frac{1}{2}c\epsilon|E^i|^2$ is the incident intensity and I_a and I_b are the intensities at the two photodetectors. The error signal shows a sharp resonant slope as well as broad dispersive wings and is shown in figure 3.8. The signal in figure 3.8 is clearly

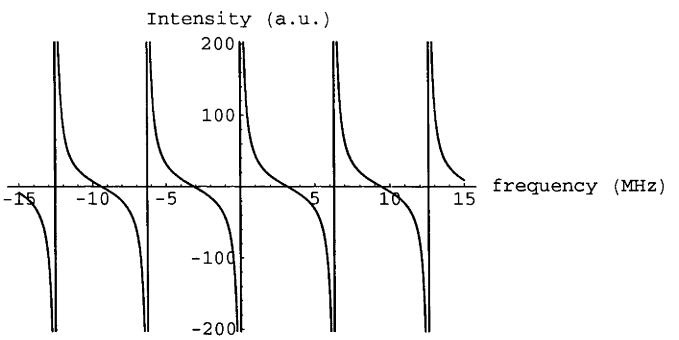

Figure 3.8: Error signal of Hansch-Couillaud locking scheme as calculated using equation 3.17 for $R = 0.97$ and $T_1 = 0.975$

idealised since absorption losses in the mirrors are not included in equation 3.17. Inclusion of absorption losses limits the peak intensity and decreases the gradient of the resonant slope which in the figure is infinite.

The favourable features of this technique are that it enables a tight lock to be achieved at the doubling cavity resonance point, and the system can easily be brought back to lock if the laser frequency accidentally drifts. The error signal is obtained directly from the reflected intensity which reduces the need for elaborate electronics which can induce delays and additional noise in the control system. The main drawback is that it is sensitive to drifts in the laser polarisation, and to any additional dispersion in the cavity optics. This was, however, not found to be a major problem in our setup which required only small readjustments in rotating the $\lambda/4$ plate after many hours of operation.

3.4 The PI controller

This section describes the theory and operation of the cavity control system which is used for locking the cavity frequency to the laser. In our system a variation on the PI (proportional-integral) controller was developed to provide active control of the cavity length. It controls the cavity length by providing corrections to the PZT mounted mirror M2, thus keeping the cavity length resonant.

3.4.1 Feedback control

The purpose of a controller in an active control system is to bring a physical quantity to a predetermined value and to hold it at this value. In our system this physical value is the length of our doubling cavity. The controller's purpose is to feed a signal that counteracts any disturbance that will alter the value. The controller senses this disturbance via the error signal that is fed to it and to counteract it sends a control signal proportional to the disturbance but with a π phase change. This is known as negative feedback.

In principle it should be possible to control a system by simply amplifying the error signal and feeding it to the control element out of phase with respect to the input. This is termed as proportional control, which when implemented within an electronics context is simply an inverting amplifier (labeled A in figure 3.9). The amplifier when fed an input V_i relative to zero volts (ground) produces an output V_o. The gain G of the amplifier is the ratio of the input to the output i.e.

$$V_o = GV_i \tag{3.18}$$

$$V_o = -\frac{R_f}{R_i}V_i$$

$$\text{where } G = \frac{R_f}{R_i} \text{ is the ratio of the resistances shown.} \tag{3.19}$$

A proportional control system would be adequate only if the control element (in our case the PZT) was able to respond to a driving signal instantaneously. In

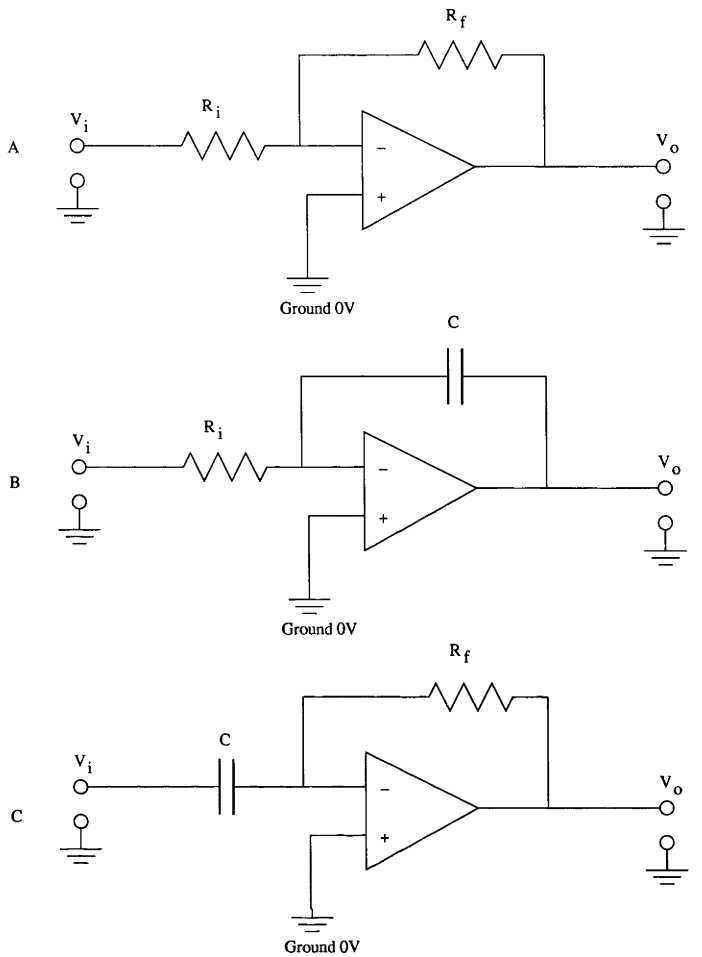

Figure 3.9: The three components of a PID controller A. proportional. B. integral. C. derivative

real situations control elements have a response time that is dependent on both amplitude and frequency of the driving signal. In this case the response time is how the PZT changes its length D upon an applied voltage V.

$$D = T(\omega)V \tag{3.20}$$

The function $T(\omega)$ is termed the frequency response. It describes the behaviour of the system in response to a small sinusoidal input at a frequency ω. Since the phase of the response is frequency dependent, the negative feedback may eventually become positive at some frequency, causing undesirable oscillation. Thus a control

system that has a frequency dependent phase and magnitude is needed. This is provided by integral and derivative stages in the control loop. The circuit diagrams for these are shown as B and C in figure 3.9.

When a voltage V_i is applied at the input of the integrator B, the output voltage V_o is proportional to the charge q on the capacitor and inversely proportional to its capacitance C

$$V_o = \frac{q}{C} = \frac{1}{C}[\int_0^t I_c dt + \text{constant}] \tag{3.21}$$

The constant is given by the charge on the capacitor at time t=0 which can be made zero. Because the inverting input in a negative feedback amplifier is always at zero volts, the current on the capacitor I_c equals the current across the resistor R_i i.e. $I_c = -I_R = -\frac{V_i}{R_i}$. Substituting this into the equation for the output voltage gives

$$V_o = -\frac{1}{C}\int_0^t \frac{V_i}{R_i} dt = -\frac{1}{R_i C}\int_0^t V_i dt \tag{3.22}$$

It can be see that the output voltage is proportional to the integral of the input voltage and $\tau = 2\pi R_i C$ is called the time constant.

The derivative stage C on the other hand produces the derivative of the input voltage:

$$V_o = -R_f C \frac{dV_i}{dt} \tag{3.23}$$

The basic configuration of a PID controller is implemented by amplifying the error signal through an isolation amplifier, passing the signal through each of the controller stages with a variable gain and finally summing each of the contributions. The general equation for such a controller is

$$V_o = -(\frac{R_f}{R_i} V_i + \frac{1}{R_i C}\int_0^t V_i dt + R_f C \frac{dV_i}{dt}) \tag{3.24}$$

This equation however is only insightful when the input V_i is a DC voltage. In a control system where we are interested in canceling out periodic signals, it is more

useful to understand the behaviour of a PID controller in terms of its frequency response. The frequency responses of the circuits shown in figure 3.9 are

$$T_{prop} = \frac{R_f}{R_i} \tag{3.25}$$

$$T_{int} = \frac{1}{i\omega R_i C + 1}$$

$$T_{deriv} = \frac{i\omega R_f C}{i\omega R_f C + 1}$$

$$T_{total} = \frac{R_f}{R_i} + \frac{1}{i\omega R_i C + 1} + \frac{i\omega R_f C}{i\omega R_f C + 1}$$

Here the $\omega = 2\pi f$ is the angular frequency of the input signal. The magnitude and phase for the derivative and integral responses given in 3.25 are

$$|T_{int}| = \frac{1}{\sqrt{1 + \omega^2 R_i^2 C^2}} \tag{3.26}$$

$$\phi_{int} = \arctan(\omega R_i C)$$

$$|T_{deriv}| = \omega R_f C \frac{1}{\sqrt{1 + \omega^2 R_f^2 C^2}}$$

$$\phi_{deriv} = \arctan\left(\frac{1}{\omega R_i C}\right)$$

The equations for the magnitude and phase of the total response are not shown for brevity. A plot of the magnitude and phase of the response versus frequency is called a Bode plot. These are shown in the following figures: 3.10, 3.11 and 3.12.

It can be seen from 3.10 that the integrator has a response that decreases as the frequency increases and has the greatest response at 0 Hz. The phase starts at zero and begins to lag up to a maximum of $\pi/2$ relative to the input signal at high frequencies. For this reason a circuit of this sort is also called a low pass filter. The derivative stage has the opposite characteristics as it has no response for DC and rises to the maximum at higher frequencies. The phase of the signal leads by $\pi/2$ which decreases with higher frequency eventually becoming in phase with the input signal. This circuit is also called a high pass filter. The proportional stage has no dependence on frequency and thus is not shown. Figure 3.12 shows how the

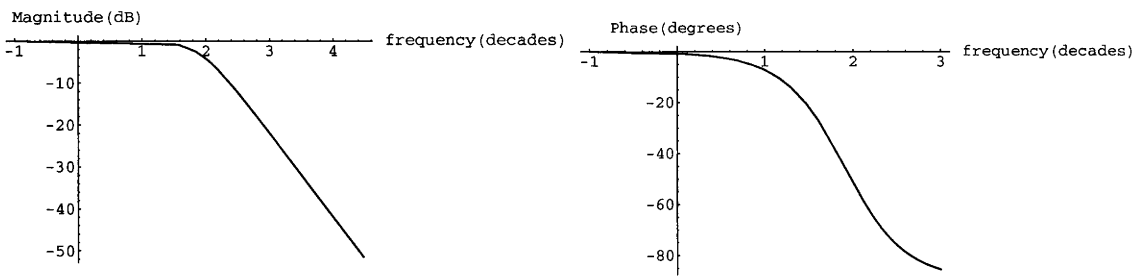

(a) integrator magnitude

(b) integrator phase

Figure 3.10: The phase and magnitude response of the integral stage calculated using equations 3.26.

combination of these three elements give the total response, in this case a notch filter which is used for removing frequencies in a narrow band from an input signal.

The frequency at which the magnitude of the response has fallen by $1/\sqrt{2}$ (corresponding to -3dB on a magnitude log scale) is called the cut-off frequency: $f_{3dB} = 1/\tau = 1/2\pi RC$ i.e. the inverse of the time constant. The response up to this frequency is essentially flat after which it begins to decrease at 20dB/decade. The region over which the response is flat is called the bandwidth.

It is also possible to attenuate the response faster than 20dB/decade by cascading multiple stages. This will give a maximum attenuation of $20n$ dB/decade and a maximum phase shift of $n\pi/2$, where n is the number of cascaded stages [38]. Any combination of these control elements can be utilised to give a desired bandwidth and roll-off. An ideal control system has the largest possible gain and bandwidth, while having zero gain at frequencies where it could cause the system to become unstable and oscillate.

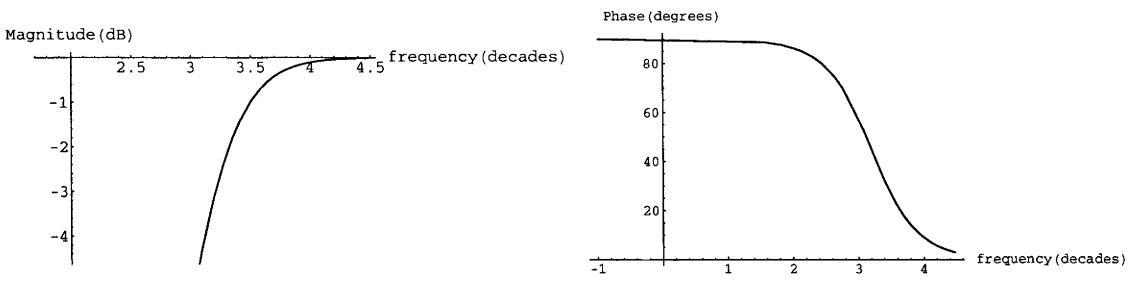

(a) derivative magnitude (b) derivative phase

Figure 3.11: The phase and magnitude response of the derivative stage

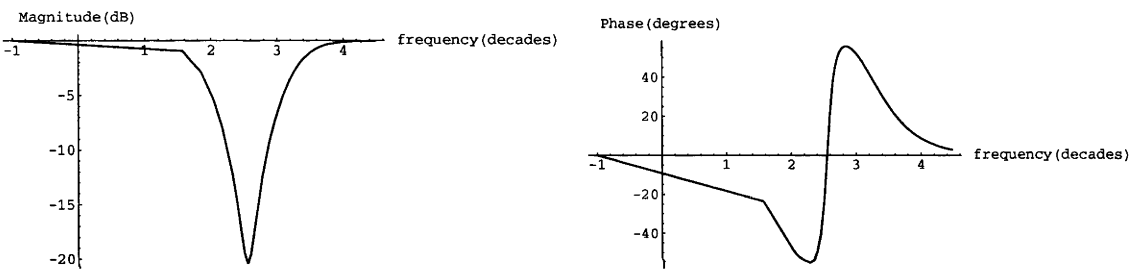

(a) total magnitude (b) total phase

Figure 3.12: The total phase and magnitude response of the system for a notch filter.

3.4.2 Overview of purpose built controller

With the discussion of the previous subsection in mind a suitable controller was built. Only an outline is presented here with details in Chapter 5. The focus was on building a workable controller which would enable the doubling cavity frequency to be locked for up to an hour at a time. Once locking was observed, the bandwidth of the lock loop was increased until it was not possible to do so due to oscillations in the system. Thus a design that enabled easy interchange of the internal components that determine the gains and time constants of the controller was essential. The re-

sponse of the PZT had to be taken into account since this is known to have resonant behaviour at higher frequencies which ultimately limits the locking bandwidth. The high voltage amplifier that drives the PZT also has a finite bandwidth and this had to be measured. The main source of disturbance in the cavity system is acoustical noise present in the room from the various vacuum pumps and the laminar flow unit that keeps the optics free of dust. Electrical hum at the mains frequency also had to be minimised.

The design of the controller is fairly standard and was based on ones built by Dr. Matt Sellars from the Laser Physics Centre. It is made on veroboard using standard operational amplifiers and passive components. The choice of operational amplifiers is due to their low-offset, low-noise characteristics while having a large gain-bandwidth product. All op-amps were used in negative feedback configuration for simplicity and higher stability. This enabled the construction of a high gain controller with a maximum voltage gain of approximately 800 at normal operation.

The general arrangement of the cavity controller and associated electronics is shown in figure 3.13. The controller includes the ramp generator used to scan through the cavity resonances used for cavity alignment, by incorporating a switch S_1 which enables the cavity to be locked or scanned. There are two controls for input and output offset of the output signal. The input offset is used to acquire initial lock and small adjustments of the lock point once the cavity frequency is locked. The output offset puts a DC offset on the output signal which at first was thought to be necessary to scan manually through the lock point but was later found to be redundant. There is also a BNC connector for monitoring the input error signal on the CRO. This compact arrangement enabled all control of the cavity to be done with one unit and minimal rewiring.

The control stage incorporates three stages: proportional (P) of low gain but highest bandwidth; integral (I) with reset; proportional filter (PF) of high gain but

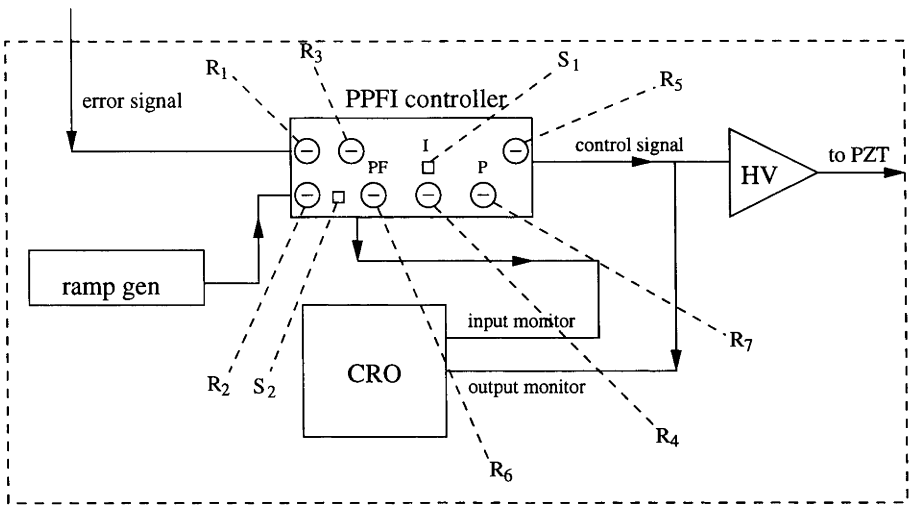

Figure 3.13: Block diagram of cavity control electronics. Legend: R_1 - input offset control, R_2 - scan depth control, R_3 - total gain, R_4 - integral gain (I) , R_5 - output offset control, R_6 - PF stage gain, R_7 - proportional stage gain (P), S_1 - integrator reset switch, S_2 - scan/lock switch, HV- high voltage amplifier, CRO - oscilloscope.

lower bandwidth than P stage composed of two identical proportional stages cascaded to give a faster roll off with frequency. The three stages are summed at the output and sent to the high voltage amplifier (HV) to drive the PZT. The gain of each control stage is set by a potentiometer from the front panel and there is also an attenuator at the input. Locking performance of the controller will be presented in Chapter 5 and instructions for its day to day operation are included in the appendices. The final circuit diagram for the controller is shown in the appendices.

The cavity controller enabled locking to the peak of the cavity resonances (limited by the drift of the Ti:Sapphire) realising a cw source of 389nm radiation. Furthermore it was possible to scan the Ti:Sapphire frequency while the cavity controller maintained lock without any need for feed forward in the system, and with only small adjustments of the controller gains. This was crucial to observe saturated

absorption signals in the He* discharge cell needed to lock the laser frequency to the 3^3P_j transition described in chapter 6.

CHAPTER 4

Optimisation of 389nm output power

4.1 Introduction

In this chapter the experiments that were performed in relation to optimising the output power of the frequency doubling cavity are discussed along with the results. Some points of the final alignment procedure are discussed, the details of which are in the appendices. The various experimental parameters that affected the ultimate conversion efficiency, in particular the mode matching and reflectivity of the mirrors are investigated and are compared with theory. Furthermore the reasons behind the observed conversion efficiency being lower than predicted are outlined, and it will be shown that the previous measurements of the output power [27], [28] are consistent with the present findings.

4.2 Cavity Alignment and Optimisation

The heart of the experimental setup is the frequency doubling cavity, which works by resonant enhancement of the fundamental intra-cavity power to produce usable powers in the UV. The ability of the cavity to perform this task is dependent on precise alignment, which is related to the interplay between the modematch-

ing and the performance of the optical components themselves. Modematching in particular is dependent on the cavity alignment and the precise placement of the modematching lenses that are external to the cavity. The experimental procedure for alignment of the cavity is described in Appendix A, assuming only that the cavity optics are in place and that the Ti:Sapphire laser source is operating. The positioning of the lenses required modeling of the beam propagation through the external optics and cavity, to calculate the beam properties through the use of ray matrices discussed in section 3.1.

4.3 Cavity Modeling and Modematching

To obtain close to optimum modematching the beam parameter inside the cavity had to be modeled. This was done by calculating the beam parameters as it propagates from the output coupler of the Ti:Sapphire laser, through the external optics and then into the cavity so that the optimum beam waist quoted in section 3.1.2 is produced in the center of the crystal. This requires the cavity dimensions to be known as well as knowledge of the beam parameters of the Ti:Sapphire output. Modeling with both a single lens and two lenses was done at various places in the cavity.

4.3.1 Ti:Sapphire characterisation

First the beam parameter of the Ti:Sapphire was measured using the BeamScan profiler. The apparatus consists of a computer controlled rotating drum that has a series of slits on its perimeter, which rotated past the input aperture where the beam is sampled and the intensity monitored by a photodiode. The computer software reads out the beam parameter from the fitted input intensity profile. The beam diameter was measured in two dimensions as the distance from the output of the laser is increased. Figure 4.1 shows the typical parabolic expansion of the beam

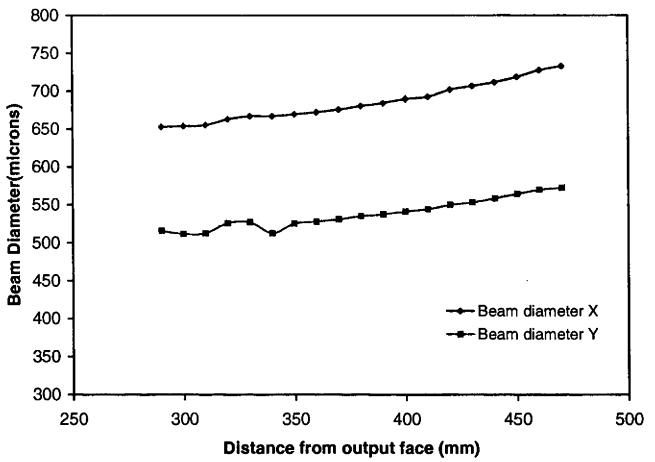

Figure 4.1: The beam diameter of the Ti:Sapphire as a function of distance from the output face, measured using the Beam Scan apparatus. Individual points obtained by averaging over 400 samples.

diameter with distance. The average ellipticity of the beam was measured to be 1.27. The waist size w_0 and its position z_0 were determined by using two points to fit to the spot size function:

$$w^2 = w_0^2\{1 + (\frac{\lambda(z_0 - z)}{\pi w_0^2})^2\} \tag{4.1}$$

The beam parameters returned by the fit are shown in table 4.3.1. The table shows that the two waists are not the same and do not coincide in position. In fact in this case they are located immediately after the output coupler. Modematching to the waist inside the cavity is made with respect to these two waists which are external to the Ti:Sapphire laser.

Using these measurements and the desired spot sizes inside the cavity, a Mathematica notebook was used to model the spot size in the cavity. The plots in figure 4.2 show variation in the spot size in the horizontal dimension and the wavefront curvature as a function of distance in between the two flat mirrors using a single f=500 mm lens for mode matching. The lens was placed 650mm from the position of

Plane	Waist size (μm)	Position (mm)
Horizontal	323.23	93
Vertical	262.49	210

Table 4.1: Beam properties of the Ti:Sapphire laser calculated by fitting the data obtained from Figure 4.1 with the waist function of equation 4.1. The position of the beam waists is relative to the output face of the laser.

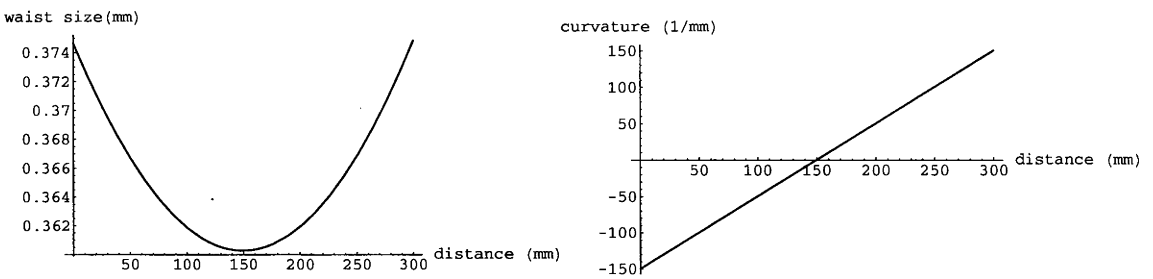

(a) beam size in the cavity

(b) wavefront curvature

Figure 4.2: The spot size and wavefront curvature in the horizontal dimension as a function of distance in between the two flat mirrrors using a single f=500mm lens for modematching. The zero in the plots is the position of the input coupler M1, and the separation between the two mirrors is 300mm.

the horizontal Ti:Sapphire waist. The minimum in the first plot is 360μm halfway between the two flat mirrors, which is slightly larger than the ideal 311μm waist size given in section 3.1.3. The waist size in the crystal when used in this configuration, depends strongly on the position of the modematching lens, while the position of the waist is more sensitive to the distance from the first focusing mirror M3. The plots for the spot size and wavefront curvatures are shown in figure 4.3. The position of the focusing mirror M3 had to be moved so as to increase the distance between it and the face of the crystal to achieve focus in the middle of the crystal 9mm from the entrance face, as shown in figure 4.3. The minimum waist is 29.4μm which is

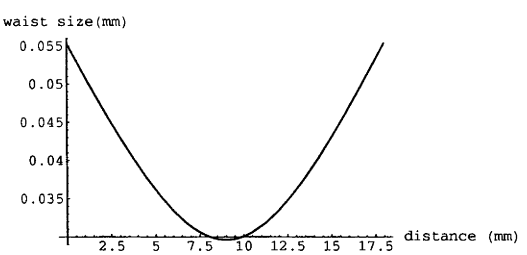

(a) beam size in the crystal

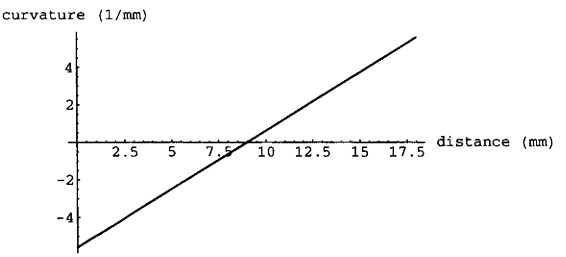

(b) wavefront curvature

Figure 4.3: The spot size and wavefront curvature in the horizontal dimension as a function of distance inside the crystal for modematching with a single lens f=500mm. Zero is at the position of the entrance face of the crystal, crystal length is 18mm.

smaller than the expected optimum size of 31.5 μm. The Mathematica notebooks used to obtain the plots for the single lens arrangement are waistcalc1lens.nb and waistcalc1lenscrystal.nb in the appendices.

The inflexibility of this arrangement is apparent since it is desirable to be able to alter the size and position of the waist independently. The problem is that the two waists are fixed spatially and each has an ideal size, so that the lens has to have a focal length that exactly matches these two waists. Similar results were obtained earlier in the year by using a single lens of f=400mm placed closer to the laser. The single lens arrangement produced only 68% of the maximum UV power that was eventually realised with a telescope. Possible reasons for this are an non-ideal waist in the crystal giving a smaller than ideal single pass efficiency, and imperfect mode match to the cavity.

The final configuration using the telescope takes care of these problems by collimating the incoming beam to a size that gives the correct waist size when focused in the crystal. It is then possible to vary the size and position of the waist in the crystal independently by translating the whole telescope backwards and forwards

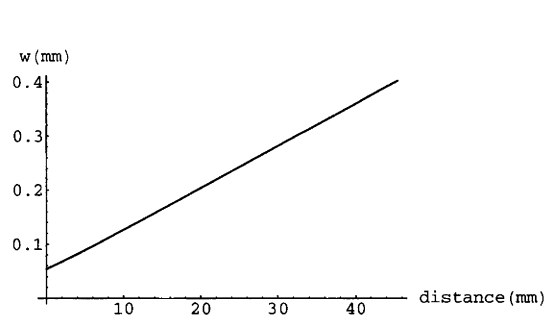

(a) beam size at exit face of the crystal

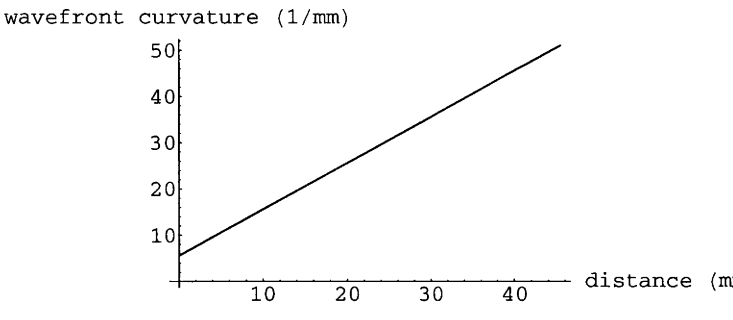

(b) wavefront curvature

Figure 4.4: The beam radius and wavefront curvature for a beam emanating at the exit face of the crystal which is $l = 9$ mm long as a function of distance. The distance from the exit face of the crystal to the focusing mirror is 45mm. The beam has been simulated as having the ideal waist size of 31.5μm at the center of the crystal.

along the beam path. Using Mathematica the optimum beam size at the first focusing mirror was calculated, starting with a waist in the crystal of 31.5μm and taking into account the change in refractive index inside the crystal. The plots shown in figure 4.4, indicate the correct beam radius at the focusing mirrors is approximately 410μm. Consequently the telescope was arranged to give a spot size as close as possible to this by placing the first lens at the position where the diameter of the Ti:Sapphire mode equaled the quoted value multiplied by the magnification ratio of the telescope (given by the ratio of the focal lengths when two lenses are used as infinite conjugates [19]). The distance between the lenses in the present case doesn't exactly equal the sum of the focal lengths as a consequence of Gaussian optics. The second lens was thus varied by monitoring the beam size at a large distance using the Beam Scan apparatus and translating the lens until the beam was collimated. Even though the final dimensions of the cavity were not exactly those quoted in section 3.1.2, the final cavity dimensions (obtained by the alignment described in appendix

A) do not alter the waist sizes and positions significantly. Figure 4.5 shows the

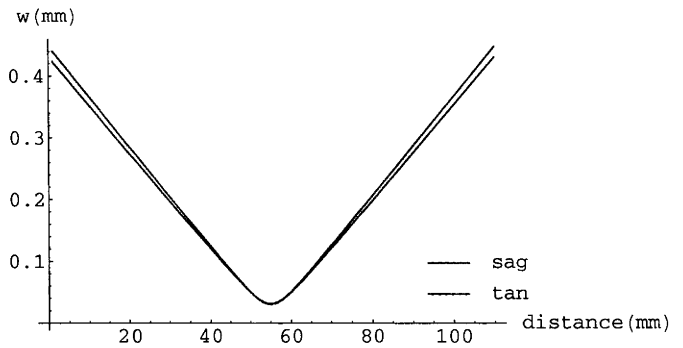

Figure 4.5: The beam radius of the lowest order cavity mode between the focusing mirrors calculated using the final cavity dimensions used in the experiment for the tangential (tan) and saggital (sag) planes.

waist positions between the focusing lenses calculated by altering the start position of the round trip between the two focusing mirrors in the ray transfer matrix (equation 3.1) and plotting the corresponding beam radius (equation 3.4) as function of position. The figure confirms that cavity waist is located halfway between the two mirrors (55mm from each focusing mirror) and the beam is non-astigmatic in the center and has a waist of 31 μm. Furthermore it supports the previous calculation of the optimal beam radius at the focusing mirrors.

4.3.2 Measuring cavity modematching

The high degree of mode matching achieved is confirmed by a measurement of the ratio of the power reflected out of the cavity on resonance versus the power that is reflected when the cavity is not resonant. This is performed by scanning through the cavity resonances and monitoring the fringes by one of the photodiodes in the Hansch-Couillaud locking setup. The result is shown in figure 4.6. Away from resonance, the laser "sees" a cavity of high loss and is reflected by the input coupler (the flat part of the trace). On resonance, however, the power entering the

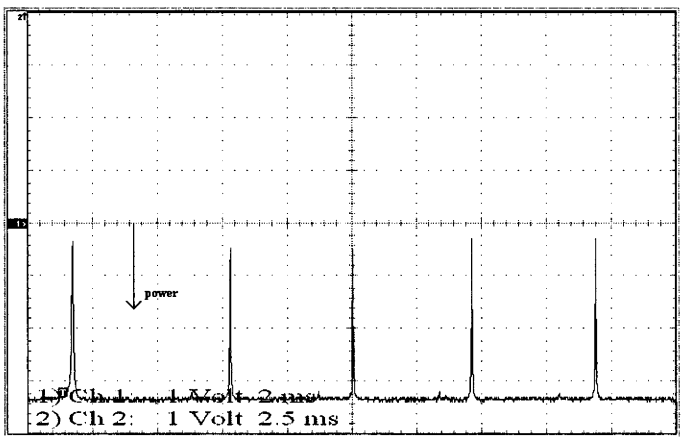

Figure 4.6: The cavity fringes monitored by one of the photodiodes when the piezo is scanned through the cavity resonances. The arrow indicates the direction of higher incident intensity from the zero line in the middle of the screen.

cavity is determined by the degree of modematching as well as impedance matching (which will be further discussed in the next section). These two factors correspond to the spatial and temporal overlap of the Ti:Sapphire and cavity mode. The trace shows that on resonance 91% of the incident power enters the cavity. The power reflected by our cavity due to impedance mismatch, has been found to be around 1.9%, so the major effect observed in figure 4.6 is due to modematching. This yields a modematching factor of $\eta = 0.89$. It may be possible to improve on this by using cylindrical lenses to correct the small astigmatism of the Ti:Sapphire, although this would not yield significant gains for the current configuration.

The well optimised modematching enabled the highest conversion efficiency to be observed in the experiments which were close to theoretical expectations. The most significant factor in determining the conversion efficiency was found to be the reflectivity of the mirrors.

4.3.3 Measuring the Finesse

The number of round trips that a laser beam undergoes inside the cavity is dependent on the losses of the optical elements. The number of round trips that a beam undergoes is roughly given by the ratio of the total losses in the cavity to the mean reflectivity of the components. This defines the finesse $\mathcal{F}$ given by

$$\mathcal{F} = \frac{\pi\sqrt{R}}{1-R} \tag{4.2}$$

$$R = R_1 R_2 R_3 R_4 T_{crystal} T_{shg} \tag{4.3}$$

where R gives the round trip mean reflectivity of all the components in the cavity and thus $1 - R$ represents the total losses. The $R_{1,2,3,4}$ are the reflectivities of each of the mirrors respectively, $T_{crystal}$ is the linear transmission in the crystal (when the incident power is low) and T_{shg} is the loss due to depletion of the pump which becomes significant at higher powers.

To be able to calculate the second harmonic power for a given incident power, the cavity finesse was measured. This is done directly from the cavity transmission signal like the one shown in figure A.3 by measuring the ratio of the free spectral range (FSR - the spacing between peaks) and the peak's full width at half maximum (figure 4.7). The results were obtained by monitoring the peak signal using three types of photodetectors (Table 4.2) to remove systematic errors since the finesse is very sensitive when $R \to 1$. Measurements were made for each of the 4 peaks in the up phase of the ramp. The waveform used was a smoothed ramp, so that the expansion of the piezo is linear to ensure the spacing between the peaks was also linear. The rounding of the edges prevent high frequency oscillations being excited in the piezo. However, because two peaks had to be captured on each scan of the digital oscilloscope (figure 4.7), discretising of the signal gives rise to systematic errors in measurement of the spacings and peak widths. In figure 4.7 the horizontal resolutions are 8×10^{-3} ms/pixel and 3×10^{-3} ms/pixel for the FSR and FWHM

Peak No	FWHM(ms)-N	FSR(ms)	FWHM(ms)-L	FSR	FWHM(ms)-H	FSR(ms)
1	0.0381	3.79	0.0381	3.81	0.0349	3.86
2	0.0349	3.67	0.0317	3.67	0.0317	3.71
3	0.0349	3.79	0.0317	3.81	0.0381	3.74
4	0.0381		0.0349		0.0413	

Table 4.2: Measurements of the peak width FWHM and FSR using three different photodetectors: N-Newport 8440 power meter; L - locking setup photodiode; H - home built photodiode.

measurements respectively which determine the shot-to-shot error in the finesse.

The measured finesses are shown in table 4.3. The measurements show that

	Finesse-N	Finesse-H	Finesse-L
	108.6 $\pm$ 8.6	121.8 $\pm$ 10.5	120.2 $\pm$ 9.5
	105.2 $\pm$ 9.0	97.4 $\pm$ 9.2	115.8 $\pm$ 11.0
	99.5 $\pm$ 8.6	91.0 $\pm$ 7.1	109.2 $\pm$ 10.3
Average	115.0 $\pm$ 5.5	103.2 $\pm$ 16.4	104.4 $\pm$ 4.6

Table 4.3: Finesse Measurements with three photodetectors to reduce errors due to instrumental factors arising from bandwidth/saturation effects. Legend: N-Newport 8440 power meter; L - locking setup photodiode; H - homebuilt photodiode. The last line is an average for each column with one standard deviation as the error. The overall average is 108 ± 9.

the finesse of the cavity is high (108$\pm$9) with the crystal in place and optimised to produce maximal 389nm light. With the crystal removed the finesse was measured to be 120-130 which is consistent with the linear loss in the crystal being about 0.08% at the fundamental. (Earlier a new crystal had to be bought because measurement of the finesse with the old crystal gave 84/87, indicating a degradation of the surfaces which was later confirmed by a simple reflection measurement of the two end faces).

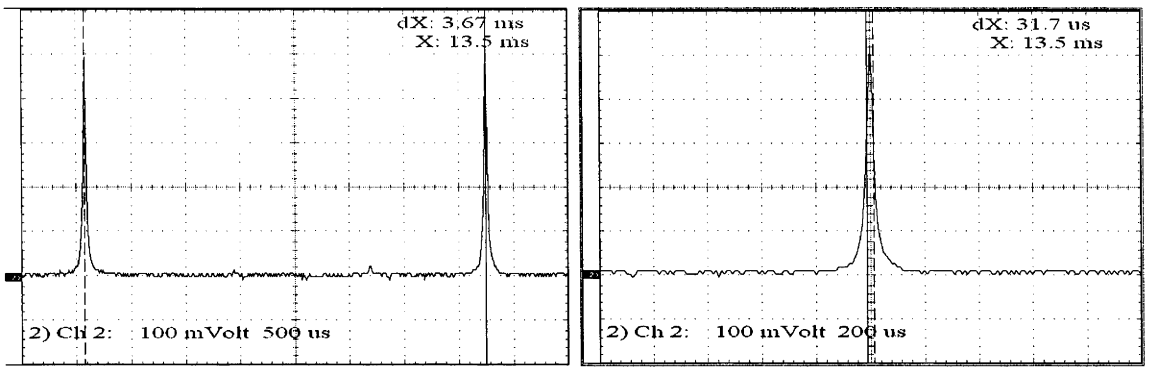

(a) One FSR (b) FWHM

Figure 4.7: Measuring FSR and peak FWHM using captures from the Tektronix TDS210 using the Wavestar software. The error in the measurements are ± 1 pixel.

4.3.4 Impedance matching

The finesse can now be used to calculate the mean reflectivity R which is

$$R = \frac{(2\mathcal{F}^2 + \pi^2) - \sqrt{(2\mathcal{F}^2 + \pi^2)^2 - 4\mathcal{F}^4}}{2\mathcal{F}^2} \tag{4.4}$$

while the error ΔR can be approximated by simplifying the previous equation and neglecting the small π^2 terms which gives

$$\Delta R = \frac{\pi}{\mathcal{F}^2}\Delta\mathcal{F} \tag{4.5}$$

The measured mean reflectivites for the three detectors and their averages are shown in figure 4.8, which indicates that the most probable reflectivity of the cavity is $R = 0.971 \pm 0.001$.

The reflectivity measurement can be affected by non-linear depletion of the pump, which can be calculated by measurement of the finesse as a function of

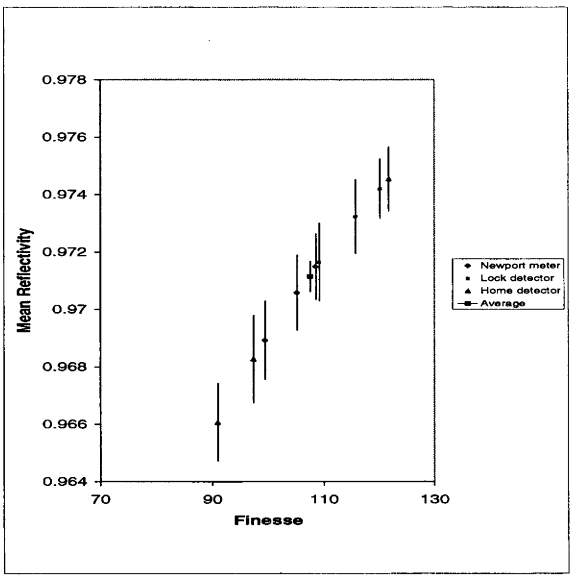

Figure 4.8: The measured mean reflectivities using the three photodetectors and the averages for each photodetector.

incident power. The enhancement in the cavity without pump depletion is [20]

$$\epsilon = \eta \frac{(1 - R_1)}{(1 - \sqrt{R_1 V})^2} \tag{4.6}$$

$V = R_2 R_3 R_4 T_{crystal}$ where V are losses other than the input coupler and

$$P_{2\omega} = \gamma_{shg} (\epsilon P_\omega)^2 = \gamma_{shg} P_{\omega,c}^2$$

Here ϵ is the enhancement, η is the modematching factor measured experimentally to be 0.89, $P_{\omega,c}$ is the circulating power on resonance, and P_ω and $P_{2\omega}$ are the incident powers at the fundamental and the second harmonic respectively. The enhancement has a maximum when the input coupler reflectivity $R_1 = V$ which is the optimum impedance matching condition. From the three input couplers that have been made for the system with $R_1 = 0.975, 0.982, 0.988$, it was found that $R_1 = 0.975$ produced the highest conversion efficiency in all the experiments performed, meaning that value of V most closely approximates R_1. So having $R = \sqrt{R_1 V} = 0.971$ which is a round trip loss of 2.9 %, $V = 0.967$ which is closest to the lowest input coupler reflectivity.

A plot of the enhancement as a function of input coupler reflectivity for various values of V is shown in figure 4.9. For the curve corresponding to $V = 0.967$ the

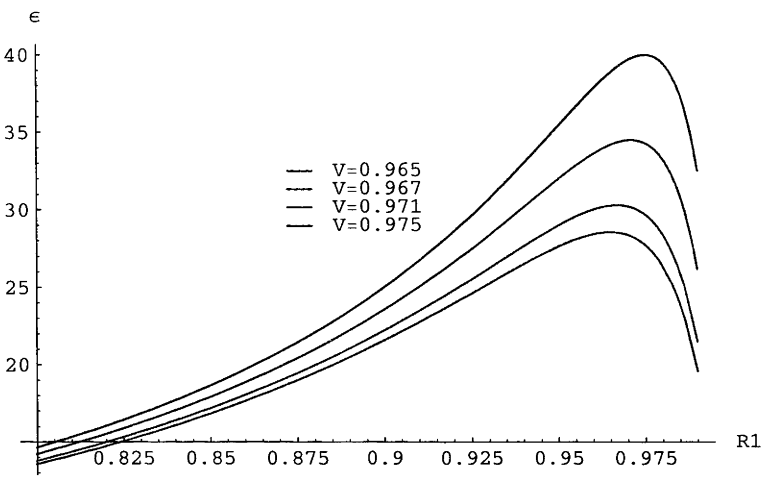

Figure 4.9: Enhancement ϵ in the cavity as a function of the input coupler reflectivity R_1 for various values of V

corresponding power enhancement ϵ for $R_1 = 0.975$ is $\epsilon \sim 30$. This means that on resonance with 1 W input power, the circulating power in the cavity is 30W. From the figure 4.9 it can be seen that significant gains that could be made with better impedance matching of the cavity with the current input coupler if $R_1 = V = 0.975$, the enhancement would be 30% higher, which would correspond to an almost 60% increase in the second harmonic power. Finally, the fraction reflected by the input coupler on resonance due to impedance mismatch is calculated as

$$\frac{P_r}{P_i} = \left(\frac{\sqrt{R_1} - \sqrt{V}}{1 - \sqrt{R_1 V}}\right)^2 \tag{4.7}$$

which for $V = 0.967, R_1 = 0.975$

$$\frac{P_r}{P_i} = 1.9\%$$

which as shown in the previous section, is smaller than the mode-matching losses.

The reasons for the poor impedance matching was found to be the reflectivity

of the mirrors which was quoted to be better than $R > 99.7\%$ [27]. However, the focusing mirrors were found to be only 99.5% reflective at 778nm by direct measurement using the calibrated Newport power meter. The piezo mirror was not measured because it is glued onto the piezo which can not easily be removed, but was assumed to have similar reflectivity, which is consistent with the measured losses in the cavity since $V = R_2R_3R_4T_{crystal} = (0.995)^3 \times 0.982 = 0.967$.

The single pass efficiency γ_{shg} can be calculated from equation 2.33 using the properties for the LBO crystal given in table 3.1 for a waist size $w_1 = 31.5\mu$m, wavelength $\lambda = 778$ nm and crystal length $l = 18$mm that gives a value of $\gamma_{shg} = 4.4152 \times 10^{-5}$ W^{-1}. This is slightly higher than the single pass efficiency which was measured by removing the input coupler and measuring the 389nm power generated by the crystal with the calibrated power meter: $\gamma_{shg} = 4.1 \pm 0.02 \times 10^{-5}$ W^{-1}. Using this, it is possible to calculate the multipass second harmonic power generated by the cavity (figure 4.10) for a given input power using equation 4.6 and $P_{2\omega} = \gamma_{shg}(\epsilon P_\omega)^2$. The experimentally measured second harmonic power corrected for the measured output coupling efficiency of 80 % at 389nm, is also shown in figure 4.10. The data points show excellent agreement with the theoretical curve. It can be seen that the effects of pump depletion are insignificant at this conversion efficiency, since the experimental points follow a P_ω^2 parabolic trend. Thus a 1W incident power coupled into the cavity produces 30mW of 389nm power. This is in agreement with measurements by previous students that have worked on this system [27], [28]. Dragana quotes 30mW at 900mW input power, which may reflect some subsequent degradation of the cavity mirrors. One of the goals of the project was to produce 40 to 100mW of power at 389nm, but this was found not to be possible due to the inadequate reflectivity of the cavity mirrors. Even with close to 100 % modematching the second harmonic power with the current cavity losses would be 37mW at maximum input power. The current conversion efficiency corresponds to a slope efficiency of 3% and a 389nm cavity enhancement factor of 732 (the ratio

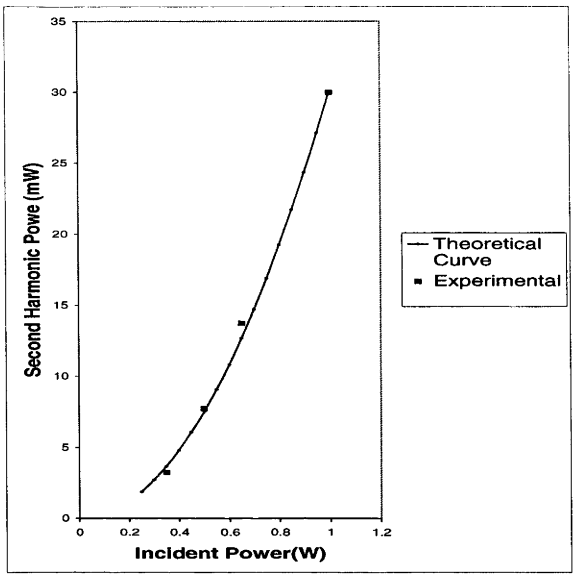

Figure 4.10: Calculated second harmonic power for $\gamma_{shg} = 4.1 \times 10^{-5}$ W^{-1}, $\eta = 0.89$ and $V = 0.967$ and experimental points corrected for output coupler transmission $T = 0.8$.

of the power generated at the UV with and without the cavity). The fundamental enhancement factor would need to be ~ 50 to achieve 100mW for 1W input power, which requires an impedance matched cavity with $R_1 = V = 0.98$.

4.3.5 Correction of output beam ellipticity

Due to the walk-off inside the crystal, the output beam is elliptical (larger in the vertical dimension) and astigmatic, thus the profile of the beam was measured to implement the appropriate corrective optics to make the output more usable for experiments. The output beam was first collimated using a single spherical lens and the diameter of the beam in the two dimensions determined by translating a 200μm pinhole mounted on a micrometer stage and recording the $1/e$ width of the intensity profile with a calibrated power meter. The beam diameters were measured to be around 710 and 270 microns in the two dimensions, equating to an ellipticity of $\approx$ 3:1. Subsequently a cylindrical telescope was setup to correct the ellipticity and

collimate the beam in both dimensions. The beam was also guided several lengths of the optical bench (total path of around 8 metres) to measure its divergence angle and the beam parameters were recorded further along the beam using the Beam Scan apparatus. This also confirmed previous measurements using the pinhole of the beam parameters and divergence. A series of scans along the beam path yielded an average ellipticity of 1.1 and far field full divergence angles of 3.3×10^{-4} and 3.7×10^{-4} radians respectively. A typical scan of the beam profile is shown in figure 4.11. All measurements were performed with the doubling cavity locked to the Ti:Sapphire using the feedback control system described in the following chapter.

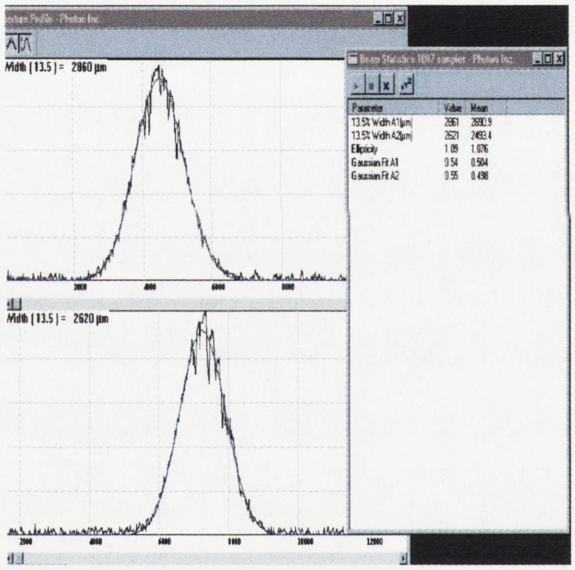

Figure 4.11: Intensity profiles in the horizontal (top trace) and vertical (bottom trace) dimensions of the corrected 389nm output. Shown are the raw intensity profiles and the fitted Gaussians from which the beam parameters are obtained. Note the relatively small noise of the intensity profiles.

4.3.6 Conclusion

It can be concluded that the maximum possible conversion efficiency has been achieved with this system. The primary limitation in its conversion efficiency is the reflectivity of its current optic set. The ellipticity and astigmatism of the output beam was corrected and a high degree of collimation was realised. Despite the limited power achieved, it was possible to perform useful experiments with the system which had previously not been done at the ANU. These experiments hinged upon the other main goal of the project which was of locking the resonant frequency of the cavity to the Ti:Sapphire laser frequency to achieve cw operation of the 389nm laser.

CHAPTER 5

Frequency locking of the external doubling cavity

In this chapter the details of the frequency stabilisation system that was used to lock the cavity resonance frequency to the Ti:Sapphire laser frequency are presented. The associated electronics - in particular the custom made controller - are described together with how they contribute to the overal stability of the control loop. Possible methods for improving the current locking system will also be discussed.

5.1 The Feedback Control System

The cavity control system is made up of three main elements as shown in figure 5.1. The purpose of the control system is to maintain a mode of the doubling cavity in resonance with the output of the Ti:Sapphire laser, and thus maximise the frequency doubled output. Any instability in the locking of the doubling cavity will result in instabilities in the intensity of the frequency doubled output as the center of the Ti:Sapphire output shifts around the peak of the cavity transmission. The control system maintains the length of the cavity so that it corresponds to an integer multiple of the Ti:Sapphire laser wavelength λ as in $1/\lambda_{laser} = m/L_{cavity}$ where m is an integer, thus satisfying the condition for the resonant enhancement of the Ti:Sapphire power. The frequency transducer is the PZT on which the

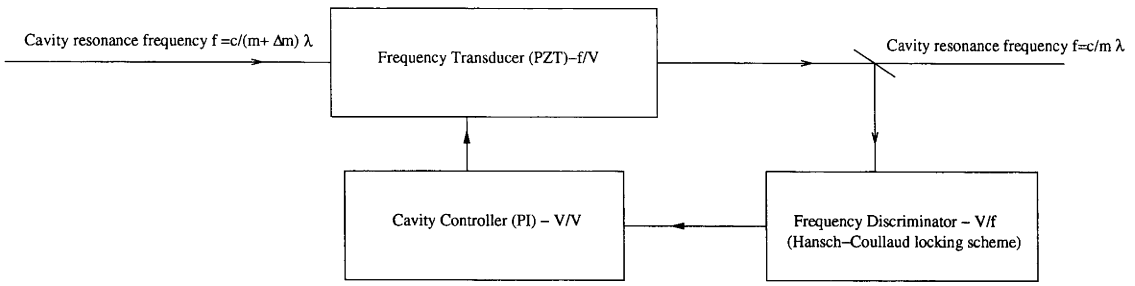

Figure 5.1: Block diagram of the external cavity control loop. It shows how a change in the resonant cavity frequency $f = c/\Delta m\lambda$ that does not correspond to an integer multiple of the Ti:Sapphire wavelength λ, is corrected by feedback to the frequency transducer. This changes the cavity frequency to an integer multiple of the free spectral range of the cavity $f = c/m\lambda$.

mirror M2 is mounted. The PZT changes the cavity length and thus the resonant cavity frequency. The frequency offset between the cavity mode and the laser was detected using the Hansch-Couillaud locking scheme. The resulting signal is sent to the cavity controller which applies the appropriate feedback signal which closes the control loop.

For the purposes of the experiments described in chapters 4 and 6, the intensity fluctuation for the 389nm output was required to be no greater than 10 %. This level of intensity stability requires the cavity length be controlled to less than 1nm which equates to a frequency offset of below 500kHz between the Ti:Sapphire output and the peak of the cavity transmission.

5.2 The Piezo Transducer

The piezoelectric stack (Piezomechanik GmbH) alters its length linearly with an applied voltage. One end of the piezo is glued to an optical mount and one of the flat resonator mirrors M2 is mounted on the other end. The piezo-electric transducer (PZT) increases its length from its equilibrium size at 0V up to a maximum

of 5μm at 150V. Shortening the cavity by this amount enables the cavity to be scanned over approximately six free spectral ranges of the cavity at the Ti:Sapphire laser wavelength. The extension produced by the piezo at an applied voltage V was measured using a He-Ne laser in a Michelson interferometer arrangement with the piezo-stack mounted mirror as one of the arms of the interferometer. The displacement was found to be linear with applied voltage with a proportionality constant of 34.39 nm/V which was comparable to the manufacturer's quoted value of 33.33 nm/V. To produce a displacement of one free-spectral range at 778nm requires a voltage of 22.7V. This translates to a $\approx$ 16 MHz/V frequency shift of the cavity resonant frequency. A high voltage amplifier (designed by Malcolm Gray and built by Mike Pennington) is used to drive the piezo-transducer up to 120 V. A previous high voltage amplifier was unstable [27] and produced large oscillations at the output which prevented stable locking of the doubling cavity. The PZT was operated in uni-polar mode, and hence large negative voltages were avoided to prevent damaging the transducer. Crucial to the performance of the system is information about the frequency response of the PZT.

The frequency of the first mechanical resonance was important since this is the practical upper frequency at which the control system can respond. The manufacturers product notes gives a general formula for calculating the first resonance frequency of the transducer:

$$F = \frac{1}{2\pi}\sqrt{\frac{S}{m}} \tag{5.1}$$

which suggests that the piezo can be treated as a spring of stiffness S with an attached mass m. The mass m is that of the mirror M2 (volume V, density n) which was calculated to be $m = Vn(BK7) = 2.51\text{g/cm}^3 \times \pi \times 0.3\text{cm}^3 = 2.36g$. This, together with the manufacturer's quoted value of $S = 45\text{N}/\mu\text{m}$, gives a resonance frequency of 22 KHz.

The other important property of the PZT is its capacitance. The product notes quote a nominal electrical capacitance of 70nF that increases with applied voltage,

since the piezo acts like a series of parallel plates that change their separation with applied voltage. The capacitance of the piezo determines its electrical properties under sinusoidal excitation, yielding information on the phase shift and its extension as a function of frequency. The capacitance is thus inversely proportional to the root mean square (RMS) distance between the plates, which is proportional to the RMS amplitude of the driving signal.

The electrical response of the piezo was measured using the circuit shown in figure 5.2. The circuit is driven by a signal generator that supplies a sine wave of

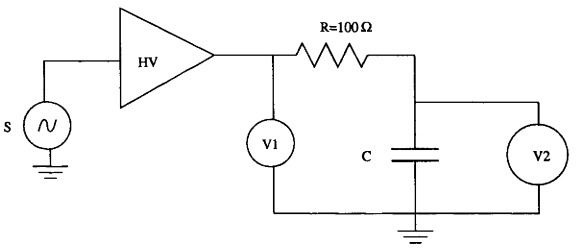

Figure 5.2: The electric circuit used to measure the piezo's electrical response. C is the piezo itself represented as a capacitance, V1 and V2 are the voltages measured on the CRO, HV is the high voltage amplifier, and S is the signal generator.

small amplitude, and the amplitudes at V1, and V2 were recorded as a function of frequency. The circuit acts as a voltage divider that has a frequency dependent gain given by

$$\frac{V1}{V2} = \frac{Z_c}{Z_c + R} = \frac{1}{i\omega C}\frac{1}{1/i\omega C + R} = \frac{1}{1 + iR\omega C} \tag{5.2}$$

This is a low-pass filter equation with a 3dB point given by $f = 1/2\pi RC$, and which exhibits phase lag that increases with frequency. Equation 5.2 only applies away from resonance, in the vicinity of which the system behaves more like a series LCR circuit. The measurement was performed for several amplitudes at the output of the HV amplifier as shown in figure 5.3. The curves in figure 5.3 are characteristic

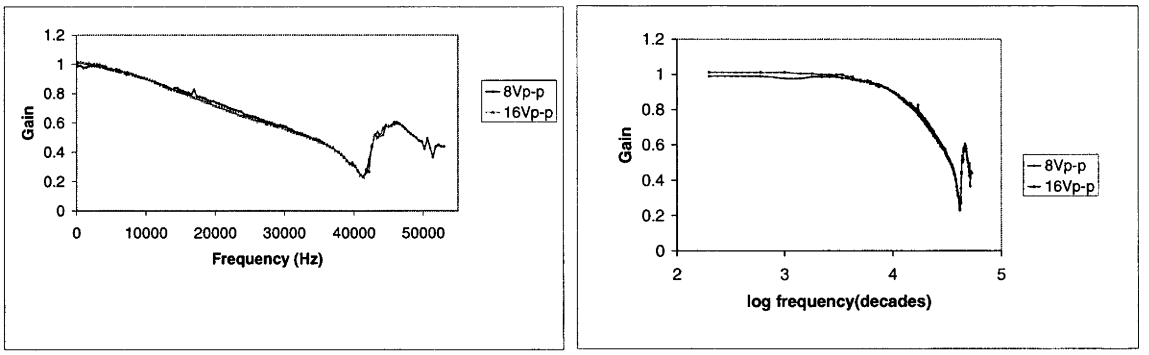

(a) (b)

Figure 5.3: The gain of the piezo as a function of frequency on (a) linear and (b) log scales for two signal amplitudes, 8 and 16V p-p.

of a capacitive load with resonant behaviour at $\approx$ 40kHz. The cut-off frequency (the -3dB point) for the 16Vp-p case is 20.6kHz compared to 21.8kHz for the 8Vp-p. The bandwidth of the piezo decreases at higher driving voltages, probably due to the amplitude-dependent capacitance effect. The equivalent capacitances are 77 and 73nF, which is consistent with the manufacturers quote of 70nF. The mechanical resonance of the piezo can be expected to be closely related to this electrical resonance, since the capacitance changes with the extension of the piezo. When the piezo is driven by the cavity controller and the frequency is locked, the size of the correcting signals sent to the piezo are of the order of 7nm/(34.27 nm/V) = 0.2Vp-p. Thus, it is expected that bandwidth would be greater than the 20KHz measured at much higher driving voltage used in Figure 5.3.

A more direct measurement of the frequency response was performed by monitoring the cavity error signal with the cavity locked, using only the integral stage gain of the cavity controller (details of which are given in section 5.4). In this configuration the cavity controller removes only low frequency vibrations below 1 kHz (the feedback system is behaving like a microphone) so that the response of the piezo could be observed at frequencies where piezo resonance occurs. The ampli-

tude response was observed by injecting a disturbance into the cavity by a signal generator of 1mV p-p amplitude (20mVp-p at the high voltage amplifier output) at the summing input of the high voltage amplifier and monitoring the residual error signal as the frequency was swept over several kHz. The phase response was also simultaneously measured using a lock-in amplifier. The schematic of the system used to obtain the measurement is shown in figure 5.4. The amplitude response of the

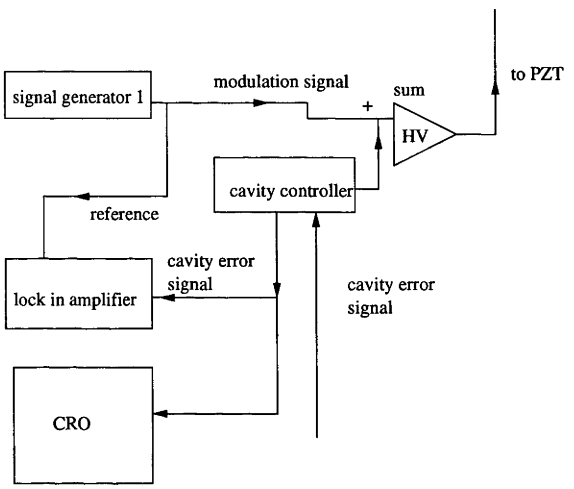

Figure 5.4: Electronic setup for measuring the amplitude and phase response of the PZT by addition of a modulation to the cavity control system.

piezo was observed by looking at the residual error signal in the frequency domain through the use of the Fast Fourier Transform (FFT) function of the CRO over a 50kHz bandwidth. A resonance was observed centered at around 8.6kHz which appears in the series of figures 5.5, 5.6, 5.7. The amplitude of the modulation peak was maximum at 8.6kHz and an overall increase in the noise at all frequencies is observed when the modulation is within 2kHz of the resonance. The plot of the amplitude and phase recorded by the lock-in amplifier (figure 5.8) shows a dramatic increase in amplitude and a rapid phase change of about 160 degrees around the resonance at 8.6kHz. The width of the sharp feature of the resonance is around 200 Hz. The roll-off at the lower frequencies is due to the cavity controller canceling the

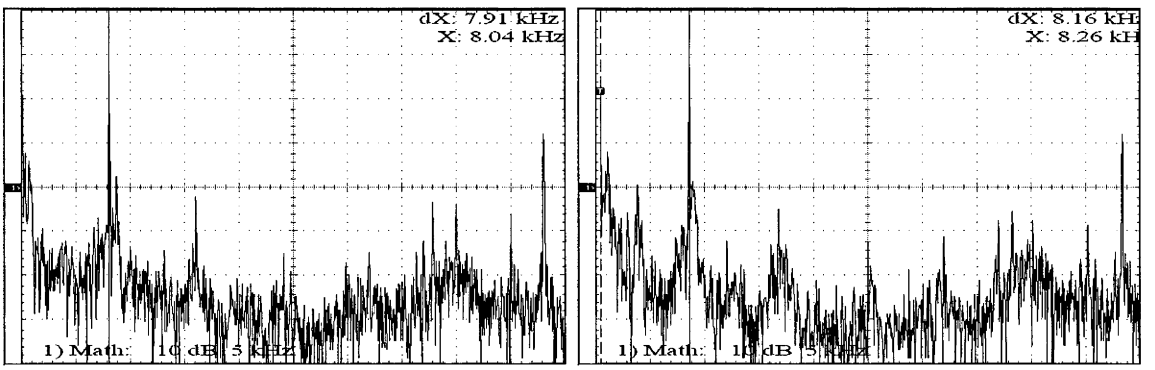

(a) 8000Hz (b) 8200Hz

Figure 5.5: Spectra of residual error signals with modulation frequencies at 8kHz and 8.2kHz. The traces are displayed on a log-linear scale with 10dB/division in the and 5kHz/division as the vertical and horizontal scales respectively. The horizontal scale is normalised to $1V_{RMS}$.

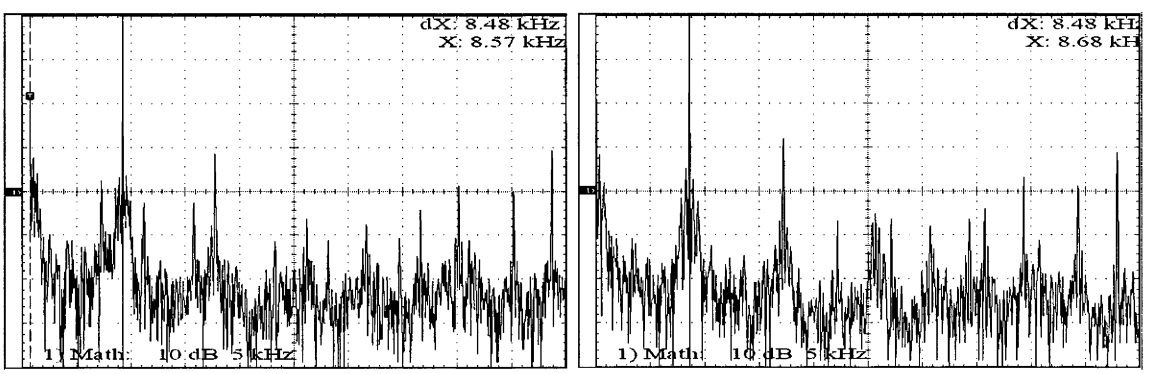

(a) 8500Hz (b) 8600Hz

Figure 5.6: Spectra of residual error signals with modulation frequencies at 8.5kHz and 8.6kHz. The horizontal and vertical scales are the same as Figure 5.5.

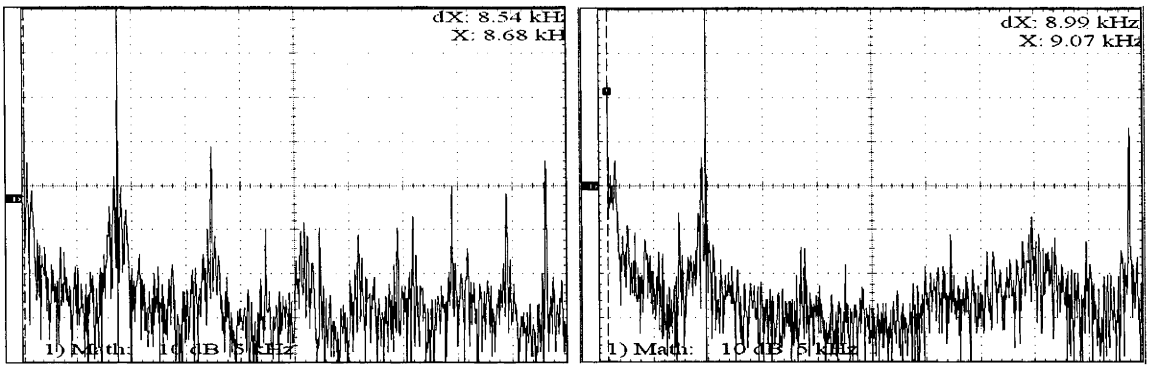

(a) 8800Hz (b) 9000Hz

Figure 5.7: Spectra of residual error signals with modulation frequencies at 8.8kHz and 9kHz. The horizontal and vertical scales are the same as Figure 5.5.

modulation signal. The plot also suggests that the amplitude response is similar at both low and high frequencies away from resonance. However there is a large phase shift at higher frequencies. A second resonance was observed at 40 kHz.

Amplitude dependence of the resonance frequency was observed by adding proportional control to the feedback loop and removing the modulation source.The proportional gain had the effect of reducing the amplitude of the error signal when the cavity was locked. The resonance was shifted to higher frequency by addition of proportional gain (figure 5.9) from 8.6 to 9kHz.

It can be concluded that due to the interplay between its electrical and mechanical properties, the piezo has a complicated frequency response. It resembles a capacitive load at low frequencies and is dependent on the amplitude of the driving signal. The usable frequency bandwidth (frequencies below the onset of resonance) increases as the extension of the piezo decreases. The maximal bandwidth of the piezo when in used in negative feedback system is of the order of 8 kHz, due to the onset of a sharp resonance at 8.6kHz (around 200 Hz wide) in the amplitude response, with a rapid change in the phase shift of $\approx$ 180 degrees across the resonance

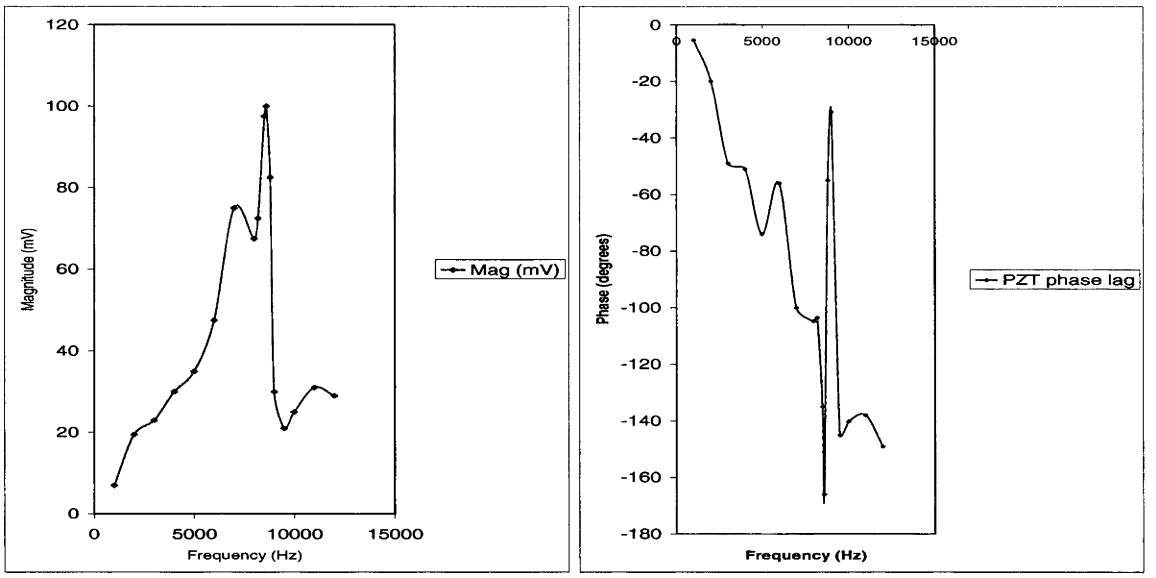

(a) amplitude response

(b) phase response

Figure 5.8: Plots of amplitude and phase response of the locked error signal with a 1mVp-p disturbance introduced into the system as a function of frequency over a range of 1-12kHz.

width.

5.3 The Hansch-Coulliaud Error Signal

The frequency discriminator in the control loop is the Hansch-Couillaud locking scheme [37] whose operation was described in Section 3.3. A typical trace of the dispersive signals generated by this scheme is shown in figure 5.10. To enable a good cavity lock, it was crucial to obtain an error signal quality similar to figure 5.10. The signal displayed here is at the MONITOR output of the controller described in detail in section 5.4. Thus there is a factor of 4 amplification of the signal and the input attenuation is 0.2. A closeup of the dispersion signal is shown in figure 5.11. The width of the resonance determines the locking bandwidth achievable with this locking scheme. The frequency width of the resonances is the free spectral range

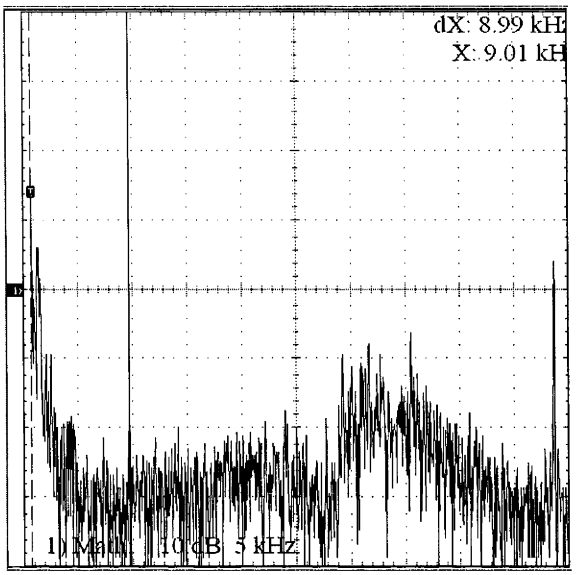

Figure 5.9: Spectrum of locked error signal with proportional signal added and without the modulation source showing the resonance a 9kHz. The horizontal and vertical scales are the same as Figure 5.5.

divided by the finesse. For this cavity specifications this is:

$$\Delta f = \frac{c}{L\mathcal{F}} \tag{5.3}$$
$$= 3.2\text{MHz}$$

This frequency width is not directly observed on the CRO since the width of the dispersion signals observed is an effect of the scanning rate of the cavity. The actual resonance width sets an upper limit on the locking bandwidth achievable. Typical error signals used in the experiment were around 220mVp-p, with a typical signal-to-noise ratio of $\approx$ 18:1 which was estimated from the magnitudes of the dispersion and noise signals present in Figure 5.10. The sensitivity at the center of the dispersive peaks of $\approx$ 13.3 MHz/V, was obtained by dividing width of the resonances given in equation 5.3 by the amplitude of the error signals. It was found that using error signals greater than 400mVp-p did not allow the cavity to lock, possibly because of the slew rate of the electronics. The amplitude of the error signals is dependent on

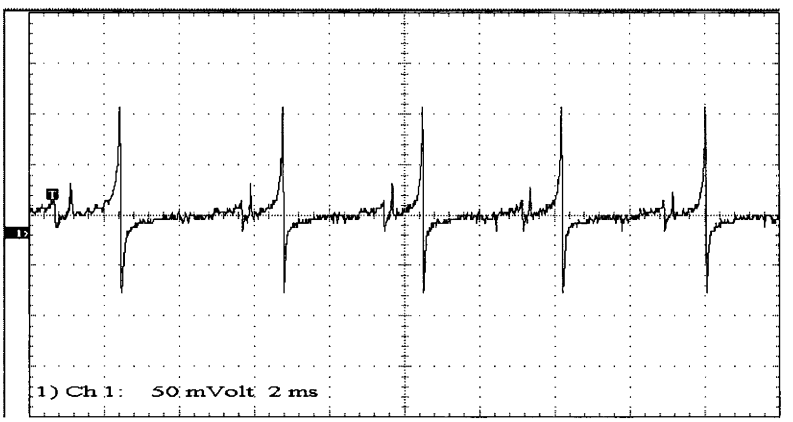

Figure 5.10: A trace of typical error signal when the cavity length is scanned. It shows the sharp resonant slope at the center dispersive wings.

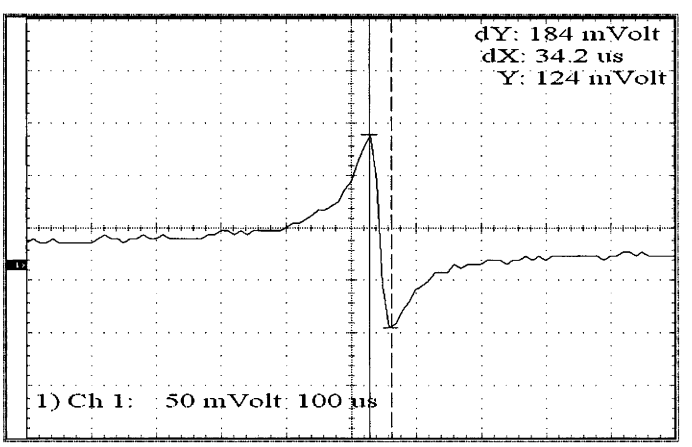

Figure 5.11: Close up of error signal showing the steep gradient at the center of the dispersion signal.

the input power of the laser with a conversion factor of 0.93V/mW.

The combined effect of the electronics of the photodiode and the controller however round the response due to their bandwidth being limited to around 10MHz [39].

The bandwidth of the photodetector amplifier was tested independently by feeding a sine wave into the BNC input of the photodetector (this is summed along with the photodiode current) and monitoring the amplitude at the output as the frequency was increased: this gave a bandwidth of 13MHz. The circuit diagram of the photodetector is shown in figure 5.12. The circuit consists of two reverse biased

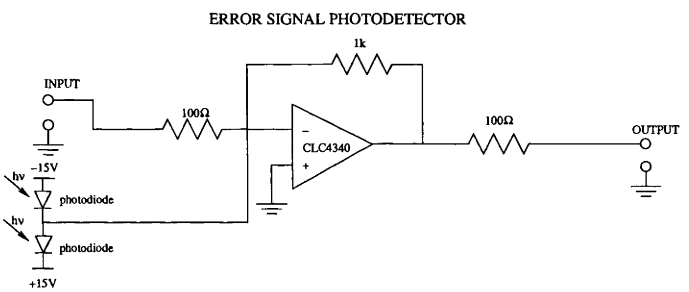

Figure 5.12: Circuit diagram of Hansch-Couillaud error signal photodector refer to text for details.

photodiodes with opposite biases that produce a photo current proportional to the incident intensity on each, which is summed at the inverting input of a CL430A operational amplifier. The amplifier produces close to zero volts when the intensity on both photodiodes is the same. The detector has been made on printed circuit board and the choice of the CL430A is due to its large bandwidth.

The operation of the Hansch-Couillaud locking setup relied on good cavity alignment, alignment of the locking optics and operation of the photodiodes in their linear regime. Higher transverse spatial modes present in the cavity caused additional dispersive shapes, resulting in a poorer lock to the fundamental longitudinal mode and locking to spurious modes. When the cavity is not on resonance the intensity at the

photodiodes is very high and saturates the photodiodes, distorting the error signal. Linear operation is ensured by a neutral density filter in the locking beam to obtain sharp dispersive resonances with a large signal-to-noise ratio. Due to an imbalance in the sensitivity of the photodiodes the dispersive signals are not centered around 0V. This imbalance is corrected by an offset in the cavity controller which requires a signal symmetrical about zero for optimal operation of its control stage.

In conclusion, the locking scheme that was implemented generated dispersive signals that had good locking characteristics: a sharp slope centered on the cavity resonance; broad dispersive wings; high signal to noise ratio. The locking system has the potential to provide a large locking bandwidth. The signal was used to drive the custom made cavity controller with great success.

5.4 Characteristics of the Cavity Controller

The electronic controller provides corrections to the cavity length using negative feedback (the input and output signals are 180 degrees out of phase) which is frequency selective, the error signal in section 5.3 being the input. The controller consists of three main parts: input section; control section; output section. Their roles can be summarised as follows:

Input section - provides initial amplification of the input error signal and electrical isolation of the control stage. Due to the error signal being non-symmetrical about zero, an input offset control is provided. An asymmetric error signal will cause laser intensity noise to be injected in the frequency doubled output by the cavity controller as it will be seen as frequency noise.

Control section - Contains the three control stages: proportional (P), integrator (I) and two-stage proportional with filter (PF) which are used to generate the drive signal for the PZT. Each stage has an adjustable gain and the individual contributions are summed.

Output section - amplifies the error signal and adds an offset if needed, or (as selected by a switch), it can send the amplified ramp signal used for scanning the cavity.

All the sections were implemented using OP7 and OP27 op-amps due to their low offset, low noise characteristics as well as having a large gain-bandwidth product. The op-amps were used exclusively in negative feedback configuration for higher stability and simplicity of design.

The circuit diagram of the input stage is shown in figure 5.13. The output of

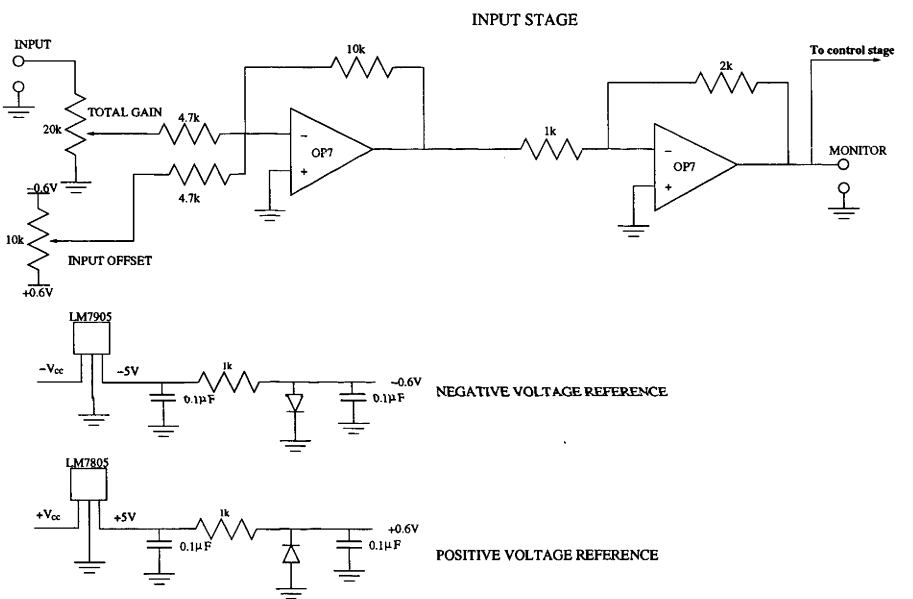

Figure 5.13: Circuit diagram of the input stage of the electronic cavity controller. Refer to the text for details.

the first amplifier is the sum of the input signal with the adjustable offset voltage. The offset voltage is generated using the fixed voltage drop across a diode used with reverse bias. This voltage drop is constant over a large range of bias currents. The output voltage of the first amplifier is simply

$$V_o = -\frac{R_f}{R_i}(V_1 + V_{off}) = -\frac{10}{4.7}(V_1 + V_{off}) = -2.1 \times (V_1 + V_{off}) \qquad (5.4)$$

Here the signal is the voltage V_1 and the offset voltage is V_{off} which ranges between $\pm 0.6V$ DC. The magnitude of the voltage V_1 is controlled by the 20k potentiometer shown in figure 5.13. The output from the first amplifier is further amplified by the second amplifier giving a total voltage gain of ≈ 4. The output of the input stage is sent to a BNC socket marked MONITOR and used to observe the error signal before the control stage on the CRO. This was found to be more useful for troubleshooting than monitoring the output of the controller. The amplified error signal is then passed to the control stage.

The control stage is made up of the three control elements and the summer. This section of the controller gives the frequency dependent amplitude and phase response needed to provide effective feedback control of the piezo over a maximum band of frequencies. To avoid exciting the mechanical resonance of the PZT at 8kHz no derivative stage is used. Instead a modified proportional-integral (PI) control stage is used. The circuit diagram of the final version is shown in figure 5.14. The

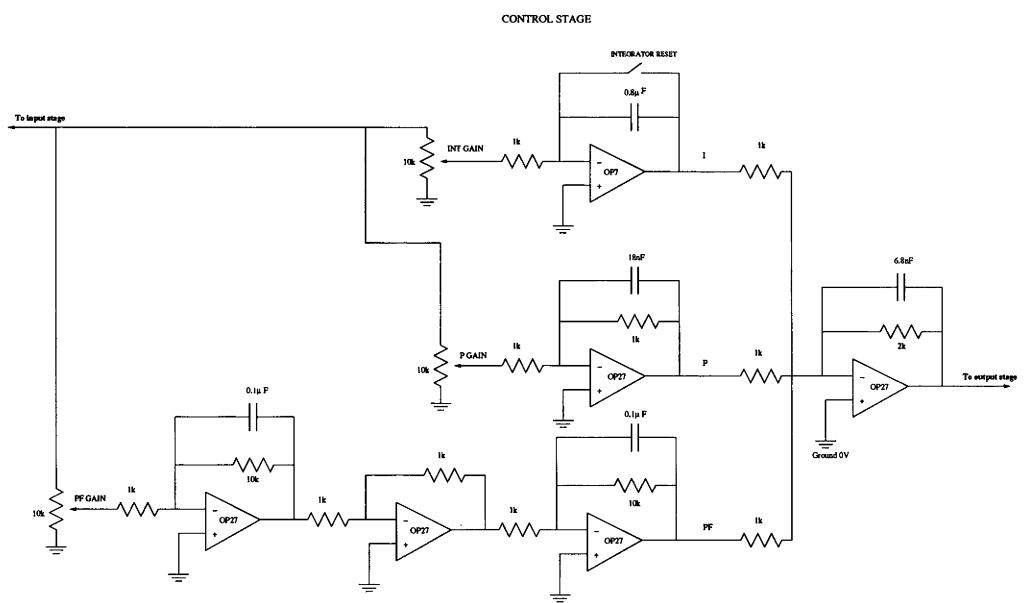

Figure 5.14: Circuit diagram of the control stage of the cavity controller. Refer to text for details.

role of the integrator (I) in the control loop is to remove drifts of the lock point, due to effects that occur on longer time scales like thermal expansion and air currents. Thus it has a small bandwidth with high gain at low frequencies. At DC the gain is the open loop gain of the op-amp ($\approx 10^5$). The integrator is a single OP7CP op amp with 0.8μF capacitor in the feedback loop giving an integration time constant $\tau = 2\pi RC = 2 \times \pi \times 1000 \times 8 \times 10^{-7} = 5ms$ with a reset switch which charges and discharges the capacitor. The reset switch is used to set the initial value of the integrator. This is necessary because the integrator yields a voltage that is proportional to the time integral (i.e. the output is proportional to the time elapsed from when the switch was opened) as well as the initial voltage. For DC voltages the expression for the integrator can be simplified as $V_o = -\frac{1}{RC}V_i(t - t_0)$ where t_0 is the time when switch is opened. Small offset voltages can quickly cause the output of the integrator to rise till it saturates to one of the power supply voltages. Thus the initial lock point, which is the voltage at time t_0, is set as close as possible to zero using the offset control of the input stage. Initially a 1 μF capacitor was used, but it was found that a shorter integration time constant gave longer locking intervals. This enabled an increase in the gain acting on the mains noise at 50Hz and its harmonics. It is present due both to electrical noise and to mechanical vibration of the optical bench by large power supplies in the laboratory.

The role of the proportional stage (P) in most controllers is to cancel vibrations in the mid band of audio frequencies usually up to several kHz. It simply amplifies the error signal and returns it with the opposite phase. In our controller the proportional stage is implemented by a single OP27 with unity gain and its response is rolled off at higher frequencies by the use of a 18nF capacitor in parallel with the 1k feedback resistor. This gives a bandwidth of $f_{3dB} = 8.8$kHz. The response of the proportional stage dominates the overall response at the higher frequencies $f > 5$KHz of our control loop and provides phase correction at these frequencies. This is manifested in the method of locking the cavity with the controller.

In our controller the section that provides most of the gain is the 2-stage low pass filter marked PF. It consists of two identical amplifiers each with nominal gain of 10. A 0.1 μF capacitor placed in parallel with the 10k feedback resistor, giving a bandwidth of f_{3dB} = 159Hz. There is a unity gain inverting buffer in between producing the two stages to reverse the phase going into the second stage, so that the output of the section is π out of phase with the input. The overall response of the PF section is that of a RC low pass filter with a nominal gain of 100 and bandwidth of f_{3dB} = 159Hz (the phase shift at this frequency is 90 degrees) but with a steeper roll-off than using a single RC stage. This section provides most of the control gain in the controller. However, because of the large gain, the bandwidth must be reduced due to the finite roll-off of its frequency response, and to avoid creating oscillations by having gain at frequencies where the piezo resonates ($f \approx$ 8.6kHz).

The error signals created by each of the individual control stages are summed by a single op-amp which also amplifies the resultant signal by a factor of 2. There is also a 6.8nF capacitor in parallel with the feedback 2k resistor that rolls off the response beyond 11KHz. This was found to be necessary to enable good locking probably due to the piezo's large phase shift at these frequencies.

Each of the control stages has a variable gain through a 10k potentiometer on the front panel of the controller which attenuates the signal at the input of each control stage. The output of the summer is the final control signal that is used to vary the cavity length when the system is locked. This signal is sent to the output stage of the controller.

The output stage of the controller implements the scan/lock function of the controller and adds a DC offset to the error signal if required. The circuit diagram for the output stage is shown in 5.15. The lock/scan switch selects whether the locking signal, or the scanning signal created by the signal generator, is sent to the output of the controller. An additional DC offset at the output was added to manually

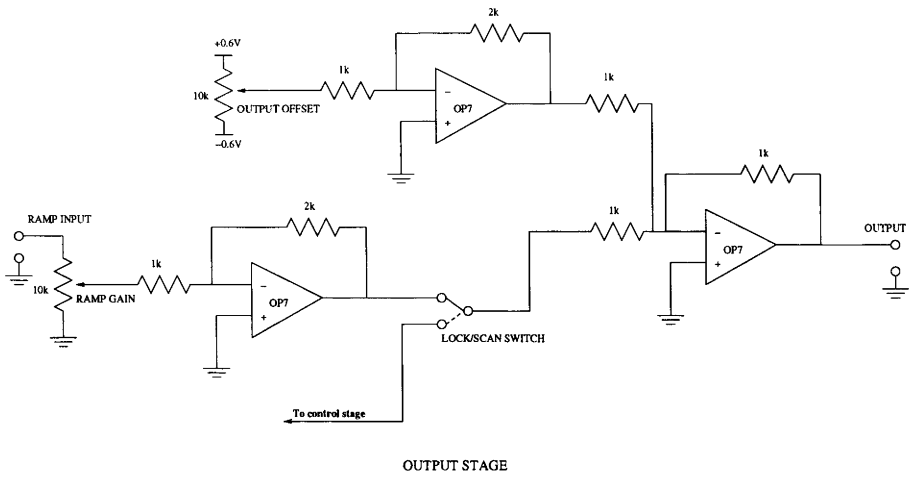

Figure 5.15: Circuit diagram of the output stage of the cavity controller. Refer to text for details

scan through the cavity resonances. The locking of the cavity can be confirmed by adjusting this offset in that the cavity stays locked i.e. the offset represents a disturbance of the system that the controller counteracts.

The locking performance of the system strongly depends on the controller's bandwidth and phase characteristics. Modeling of the controller is thus useful to analyse the locked error signals. To calculate the overall response of the controller the response of each of section need to be calculated and then combined in the appropriate way to give the total response. The response of each section consists of the responses of each of the op-amp circuits which can be directly derived using circuit theory. Since the input and output stages contain no frequency selective elements, calculation of their responses is simple and omitted for the moment since their effect is only to introduce constant multiplicative factor G to the overall response. The expression for output can be written as follows

$$T(\omega)_{total} = dG(aT(\omega)_P + bT(\omega)_I + cT(\omega)_{PF})T_{sum} \tag{5.5}$$

where a, b, c, d are attenuation constants between 0 and 1.

The attenuation constants a, b, c represent the positions of the potentiometers controlling each of the individual controller gains, while T_P, T_I, T_{PF} are the responses of each control element, T_{sum} is the response of the summer alone, and d is the position of the input attenuator. The response functions of each control element is a complex quantity whose phase and amplitude are both frequency dependent. From the theory of complex numbers it follows that if two stages with responses T_1 and T_2 are cascaded then the total response T_3 is given as

$$T_1 = r_1 e^{i\phi_1} \text{ where } r_1 \text{ is the magnitude and } \phi_1 \text{is the phase} \tag{5.6}$$

$$T_2 = r_2 e^{i\phi_2} \text{ where } r_2 \text{ is the magnitude and } \phi_2 \text{is the phase}$$

$$T_3 = T_1 T_2 = r_1 r_2 e^{i\phi_1 + \phi_2} = r_3 e^{i\phi_3}$$

The magnitudes are multiplied and the phases are added (de Moivre's rule). However at the summing point the situation is more complicated in that both magnitude and phase depend on the magnitudes and phases of each contribution. If we have three elements being summed, the expression for the resultant response and its magnitude is.

$$T_4 = T_1 + T_2 + T_3 = r_1 e^{i\phi_1} + r_2 e^{i\phi_2} + r_3 e^{i\phi_3} \text{ which when squared yields} \tag{5.7}$$

$$T_4 T_4^* = (r_1 \cos\theta_1 + r_2 \cos\theta_2 + r_3 \cos\theta_3)^2 + i(r_1 \sin\theta_1 + r_2 \sin\theta_2 + r_3 \sin\theta_3)^2$$

$$= r_1^2 + r_2^2 + r_3^2 + 2(r_1 r_2 \cos(\theta_1 - \theta_2) + r_2 r_2 \cos(\theta_2 - \theta_3) + r_1 r_3 \cos(\theta_1 - \theta_3))$$

The magnitude squared $T_4 T_4^* = |T_4|^2$ is the sum of the squares of the individual magnitudes plus an interference term. The resultant phase ϕ_4 is given by

$$\phi_4 = \arctan\left(\frac{r_1 \sin\theta_1 + r_2 \sin\theta_3 + r_3 \sin\theta_3}{r_1 \cos\theta_1 + r_2 \cos\theta_2 + r_3 \cos\theta_3}\right) \tag{5.8}$$

The amplitude and phases of the responses of each of the control elements T_{int},T_{PF} and T_P as functions of the angular frequency ω are

$$|T_P| = \frac{R_p}{R_s}\frac{1}{\sqrt{1+\omega^2 R_f^2 C_p^2}} \tag{5.9}$$

$$\phi_P = \arctan\left(-\omega R_f C_p\right)$$

$$|T_{PF}| = \left(\frac{R_{pf}}{R_s}\right)^2 \frac{1}{1+\omega^2 R_{pf}^2 C_{pf}^2}$$

$$\phi_{PF} = \arctan\left(-\frac{2\omega C_{pf} R_{pf}}{1-\omega^2 R_{pf}^2 C_{pf}^2}\right)$$

$$|T_{int}| = \frac{R_{int}}{R_s}\frac{1}{\sqrt{1+\omega^2 R_s^2 C_{int}^2}}$$

$$\phi_{int} = \arctan\left(-\omega R_s C_{int}\right)$$

These series of equations can be combined with equations 5.7, 5.8, and 5.5 to give the magnitude and response of the controller, where the substitutions $r_1 = T_P, r_2 = T_{PF}, r_3 = T_{int}, \phi_P = \theta_1, \phi_{PF} = \theta_2, \phi_{int} = \theta_3$ have been made. The component values used in the equations are those quoted previously for each section. A plot of the amplitude and phase response of the various stages of the controller is shown in figure 5.16. The plots in figure 5.16 show a frequency span of 0-50 kHz. The plot of the total amplitude response shows a high gain at frequencies below 1kHz rolling off to almost zero gain at 10kHz. The PF stage dominates the gain until $\sim$ 1.8kHz when the proportional stage starts to dominate following the roll off of the PF stage. The plot of the phase response shows that for lower frequencies the phase is dominated by the PF stage, while at higher frequencies the phase shift is compensated by the phase of the P stage.

5.5 Control loop stability and bandwidth

The frequency stability that can be achieved with this system depends on the interaction between the optical and electrical components of the system. This requires

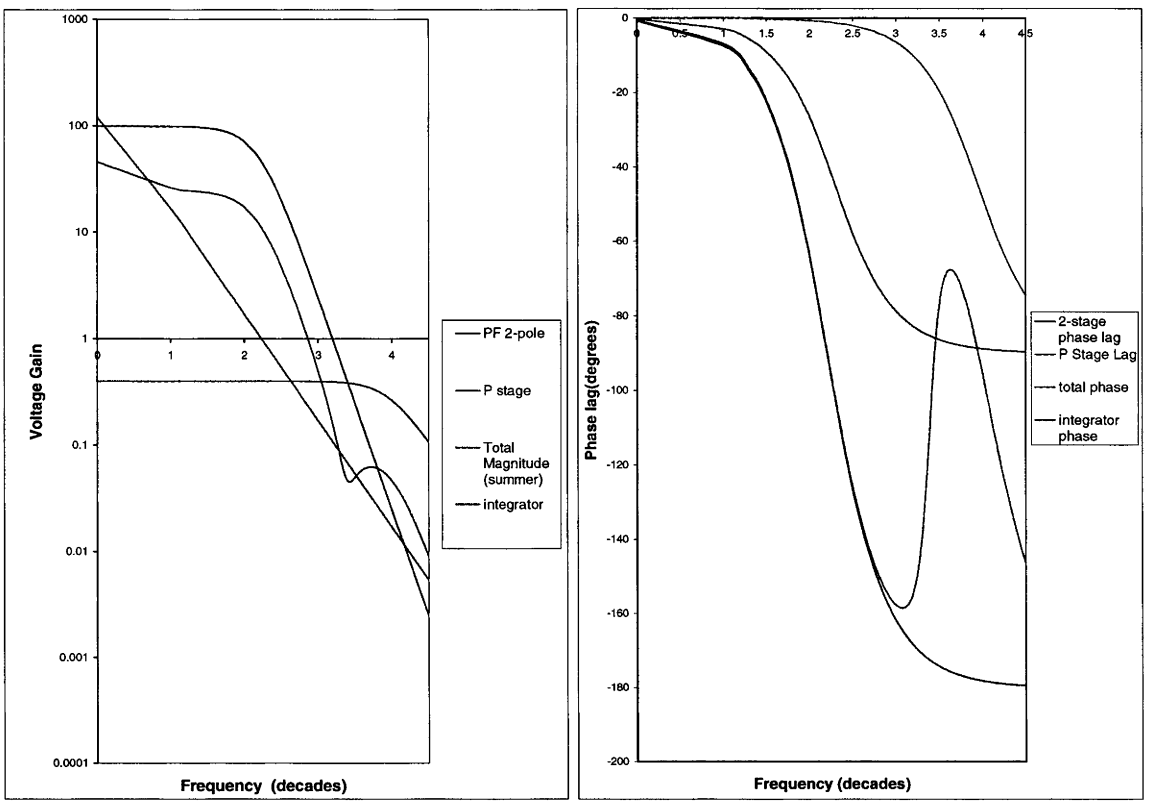

(a) controller gain vs freq

(b) controller phase vs freq

Figure 5.16: The gain and phase response of the cavity controller for typical values of the attenuation constants $a = 0.95$, $b = 0.8$, $c = 0.9$ in this case $d = 0.02$

modeling of all the components of the control loop which is in principle difficult because it requires modeling in both electrical and optical domains. The goal is to maintain the cavity in resonance with the laser through feedback control. This can be thought of as reducing the spectral density of the laser intensity noise $S_{cavity}(f)$ in units of $V/\sqrt{Hz}$ caused by external disturbance of the cavity altering the relative frequency between the resonant cavity frequency and Ti:Sapphire output. The control loop can be represented by the block diagram shown in figure 5.17. Each of the blocks can be represented by transfer functions that relate the amplitude and phase of the output to its input. The block diagram shows how the disturbance of

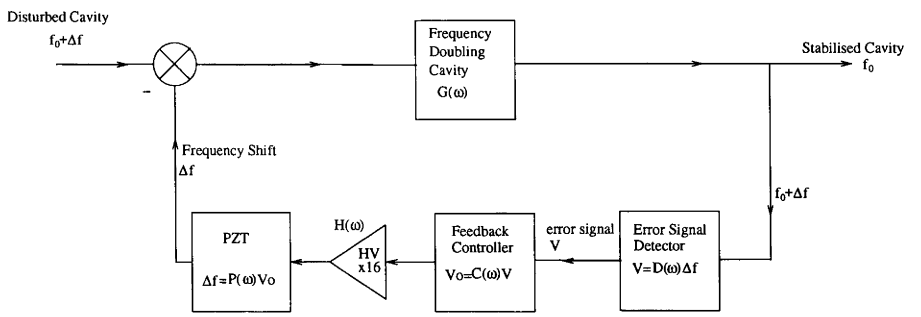

Figure 5.17: Block diagram of total control loop of the external feedback stabilization system with equivalent transfer function for each block.

the cavity causing it to be resonant at some frequency $f_0 + \Delta f$ is canceled through the generation of the error signal which is converted into an appropriate voltage by the controller and this is converted back into the optical domain by the piezo inside the cavity canceling the frequency shift Δf. The bandwidth when the control loop is closed determines the reduction in the intensity noise of the output. The calculation of the closed loop transfer function for the block diagram in figure 5.17 is given by

$$S_{loop} = \frac{S_{cavity}|G(\omega)|}{|1 + C(\omega)P(\omega)D(\omega)H(\omega)G(\omega)|} \tag{5.10}$$
$$= \frac{S_{cavity}|G(\omega)|}{|1 + G(\omega)_{openloop}|} = S_{cavity}|G(\omega)_{closedloop}|$$

where S_{cavity} represents the density of laser frequency noise of the cavity. The terms appearing in the denominator are the frequency responses of each of the elements in the control loop as a function of the driving signal frequency ω:

$C(\omega)$ - the frequency response of the cavity controller which outputs a voltage proportional to the inputs signal with an appropriate phase.

$P(\omega)$ - the piezo's frequency response that determines the displacement of the piezo and thus frequency shift of the resonant cavity in MHz/V.

$H(\omega)$ - frequency response of the high voltage amplifier.

$D(\omega)$ - frequency response of the locking setup that converts a frequency shift

of the cavity resonant frequency into an error signal voltage in (V/MHz).

$G(\omega)$ - this represents the frequency response of the cavity to disturbances. The bandwidth can be interpreted as the modulation frequency at which the cavity build up time becomes comparable to the cavity linewidth.

The product $C(\omega)P(\omega)D(\omega)H(\omega)G(\omega) = G(\omega)_{openloop}$ is called the openloop transfer function of the system and from equation 5.10 it is apparent that if $G(\omega)_{openloop} = -1$ the control loop would increase the noise of the laser rather than reduce it.

It is possible to determine whether the closed loop is stable by looking at the open loop response and its behaviour around the -1 point on a Nyquist plot [40]. The Nyquist plot combines the magnitude and phase information into one graph. For example, the Nyquist plot for the total response of the controller is shown in figure 5.18. The stability of the system when used in closed loop with feedback, is

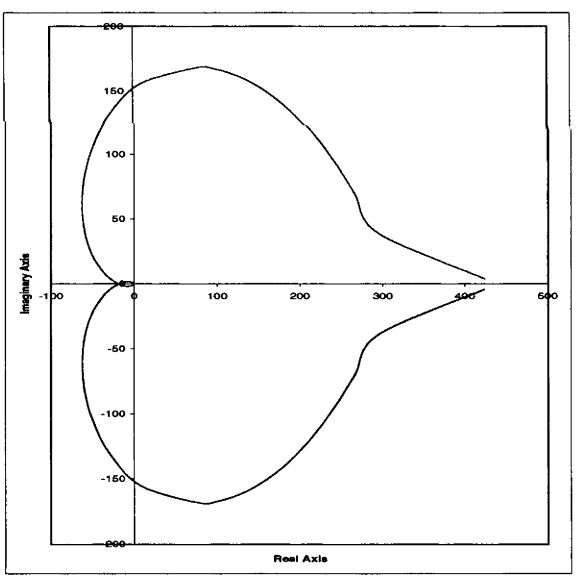

Figure 5.18: Nyquist plot of cavity controller response. It shows a polar plot of the controller's amplitude and phase as the frequency is increased. The angle from the origin is the phase and the distance is the amplitude. The bottom half of the plot is mapped in a clockwise fashion starting at the positive real axis.

determined by the number of clockwise encirclements of the point (-1,0) which are numbered N (clockwise encirclements are counted as negative encirclements); the number of half right plane poles (points at which the system shows an infinity for a positive frequency) in the open loop transfer function P; and taking the difference between them Z=P-N. If Z is positive then the closed loop system is unstable, and if Z=0 the system is only marginally stable [40]. For the plot shown above the open loop transfer function has no right half plane poles. Thus for the system to be stable in a closed loop, the Nyquist diagram should not encircle the (-1,0) point. Whether the contour encircles the point -1 in this case is dependent on the individual control stage gain factors a, b, c and the overall gain d.

Through the interaction of the mechanical and electrical properties of the piezo, the system as a whole exhibits resonant behaviour when driven by periodic signals. An appropriate model for the piezo's response is given by a second order system [41] which can be recast into a form

$$P(\omega) = \frac{c}{2i\gamma f(\omega) + k(\omega)} \tag{5.11}$$

$$\text{where } f = \frac{\omega}{\omega_n}, k = 1 - f^2$$

$$|P(\omega)| = \frac{c}{\sqrt{k^2 + 4\gamma^2 f^2}}$$

$$\phi_{piezo} = \arctan\left(\frac{-2\gamma f}{k}\right)$$

The natural frequency ω_n is the oscillation frequency in the absence of damping, γ is the damping ratio and the constant $c = 16$ MHz/V is the induced optical frequency shift per volt. The parameters ω_n and γ can be adjusted to fit experimental values. The plot in figure 5.19, which shows the magnitude and phase response of this model, displays the typical resonant behaviour that occurs at $\omega_r = \omega_n\sqrt{1-\gamma^2}$, with a phase shift tending to -180 degrees at high frequencies.

The locking signal generator can be approximated as a first order system having a bandwidth frequency of 3 MHz (the linewidth of our cavity error signals) and a transfer function similar to one of the control stages. This is a valid model because

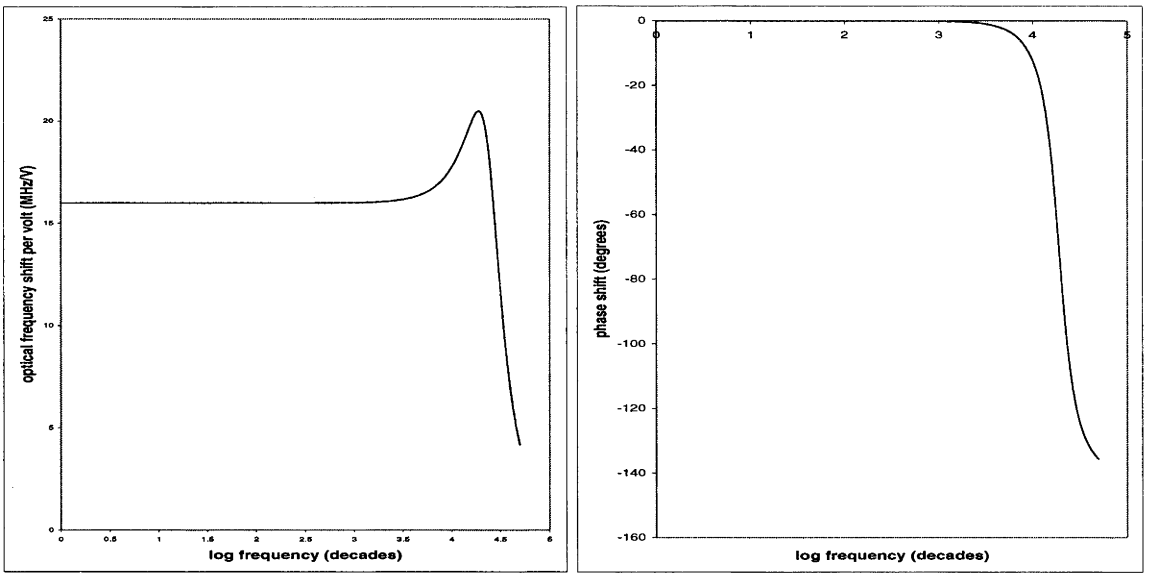

(a) pzt magnitude

(b) pzt phase

Figure 5.19: The magnitude and phase response of the piezo model for a resonant frequency $\omega_r = 11$kHz and damping $\gamma = 0.4$. The values resemble the experimental data of the piezo response.

the error signal is generated in reflection and the maximum phase shift that occurs is 90 degrees and the characteristic time is the build up time of the cavity which is the inverse of the linewidth.

$$D(\omega) = \frac{d}{i\omega R_{dis} C_{dis} + 1} \tag{5.12}$$

$$\text{where } f_{3dB} = 1/2\pi R_{dis} C_{dis} \approx 3 \text{ MHz}$$

The constant $d = 0.075$ V/MHz is the inverse of the gradient at the center of the dispersion signal and gives the conversion factor between the optical frequency shift and the generated error signal voltage. The high voltage amp frequency response $H(\omega)$ can be modeled similarly by a single order system which has a bandwidth of the order of 60kHz and a voltage gain of 20.

The cavity frequency response $G(\omega)$ can be regarded as a constant, only the reflected intensity is being sampled to extract the error signal, so essentially it has

been absorbed into the response of the discriminator.

The stability of the control loop and the locking bandwidth (bandwidth of the closed loop response) can be calculated and compared with the residual error signal obtained from experiments. The open loop response $G(\omega)_{openloop}$ is:

$$G(\omega)_{openloop} = dG(aT(\omega)_P + bT(\omega)_I + cT(\omega)_{PF})T_{sum}D(\omega)H(\omega)P(\omega)) \tag{5.13}$$

To determine the positions of the poles of this open loop transfer function, it can be rewritten as follows:

$$G(\omega)_{openloop} = dG\frac{1}{sR_{HV}C_{HV}+1}\frac{1}{sR_{sum}C_{sum}+1}\frac{1}{sR_{dis}C_{dis}+1}\times \tag{5.14}$$
$$(\frac{a}{sR_PC_P+1} + \frac{b}{(sR_{PF}C_{PF}+1)^2} + \frac{c}{sR_{int}C_{int}+1})\frac{1}{s^2R_{piezo}^2C_{piezo}^2 + 2s\gamma R_{piezo}C_{piezo}+1})$$

In this equation the $s = i\omega$ and all the constant factors appearing in the numerator have been absorbed into the constant factor G. The equation 5.14 can be rewritten as a product of factors where the roots (ie the poles of the openloop function) of the denominator are

$$\begin{aligned} s &= -\frac{1}{R_{sum}C_{sum}} \\ s &= -\frac{1}{R_{dis}C_{dis}} \\ s &= -\frac{1}{R_{HV}C_{HV}} \\ s &= -\frac{1}{R_PC_P} \\ s &= -\frac{1}{R_{PF}C_{PF}} \\ s &= -\frac{1}{R_{int}C_{int}} \\ s &= \pm\frac{\sqrt{\gamma^2-1}-\gamma}{R_{piezo}C_{piezo}} = \frac{-\gamma \pm i\sqrt{1-\gamma^2}}{R_{piezo}C_{piezo}} \end{aligned} \tag{5.15}$$

The roots appearing in equation 5.15 are all in negative half plane of the frequency contour, meaning that for stability there should be no encirclements of the -1 point of the Nyquist plot for the system to be stable in a closed loop. This is a consequence of the fact that there are no elements in the control loop that introduce a lead in the

phase (a derivative stage for example). The open loop magnitude has to be less than 1 when the phase shift becomes 180 degrees. Both the controller and the piezo's response affects the stability of the loop. An example of a Nyquist plot showing a stable system is given in Figure 5.20 for a piezo resonant frequency of $\omega_r = 15.2$ kHz and damping factor $\gamma = 0.5$. Figure 5.20 shows a stable system in a closed loop

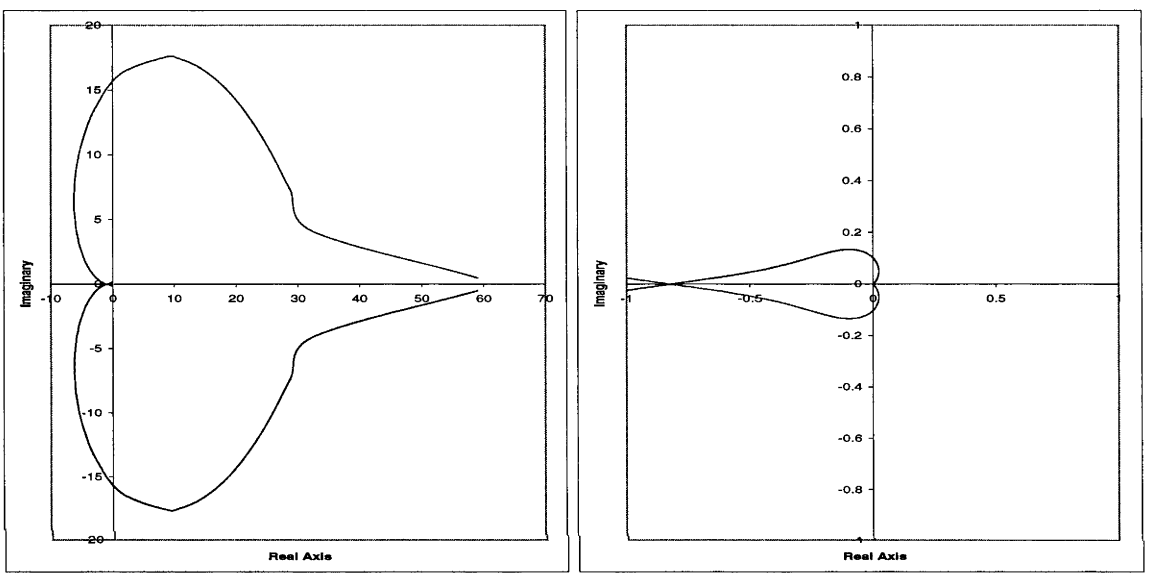

(a) nyquist plot of open loop

(b) closeup of -1 region

Figure 5.20: Nyquist plot of the cavity controller transfer function and close up of the (-1,0) critical point for gain constants $a = 0.99$, $b = 0.8$, $c = 0.8$, $d = 0.01$

because the contour does not encircle the -1 point on the real axis. However, if the gain of the controller was increased, the system would begin to oscillate at the frequency that corresponds to the intersection of the negative real axis. The amplitude increase required for the Nyquist contour to intersect the negative real axis is the gain margin g. It is usually expressed in decibels

$$G_{margin} = 20 \log_{10}(g) \tag{5.16}$$

In the previous plot the gain at the intersection of the real axis is 0.83 thus the margin is 1.61dB. The phase margin is the rotation about the origin that would cause the contour to touch the -1 point. This is found by looking at the phase rotation from the point where the contour crosses the real axis and where the magnitude is equal to 1. In the previous graph this is 1.3 degrees, which can be represented as the maximal additional time delay that can be tolerated in the control path for a signal at a particular frequency, before the control loop becomes unstable i.e. $t = \frac{1.3\times\pi}{2\pi f\times 180} = \frac{1.3}{2\times 200\times 180} = 18\mu$s for a 200 Hz signal. These two parameters characterise the closed loop stability. Higher loop stability is achieved by having larger gain and phase margins. The effect of changing the overall gain d by adjusting the input attenuator is shown in figure 5.21. Figure 5.21 shows that the control loop is stable for values of $d = 0.02, 0.1, 0.4$ and unstable for $d = 0.5$ while lower values of d would mean greater stability. This means that the overall gain is reduced and since the roll-off of the total response is fixed, there is a trade-off between the two. This is particularly true for higher frequencies where the available gain is smaller, which manifests itself in the way the cavity is much more sensitive to high frequency vibrations when locked rather than at low frequencies (e.g. tapping the table will not cause the cavity to go out of lock, while dropping a metal object on the table does).

The set of Nyquist plots shown in figure 5.22 display the stability of the system as the proportional gain is turned down controlling the parameter a. As the proportional gain the system becomes smaller the system becomes more unstable, which closely resembles what occurs in practice. The control loop oscillates with no proportional gain P in the control loop because the proportional stage compensates for the phase lag of the dominant PF stage at higher frequencies that quickly approaches 180 degrees. The system is highly unstable with these parameters and very prone to small disturbances causing it either to maintain oscillation or push the system far from one of the cavity resonances. The model also predicts that

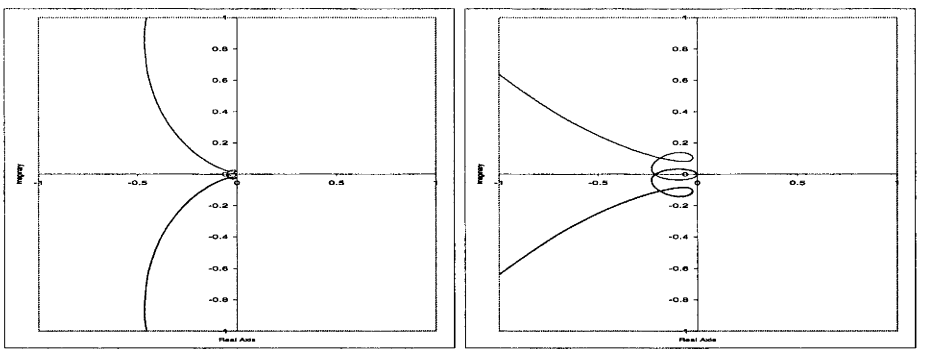

(a) d=0.02 (b) d=0.1

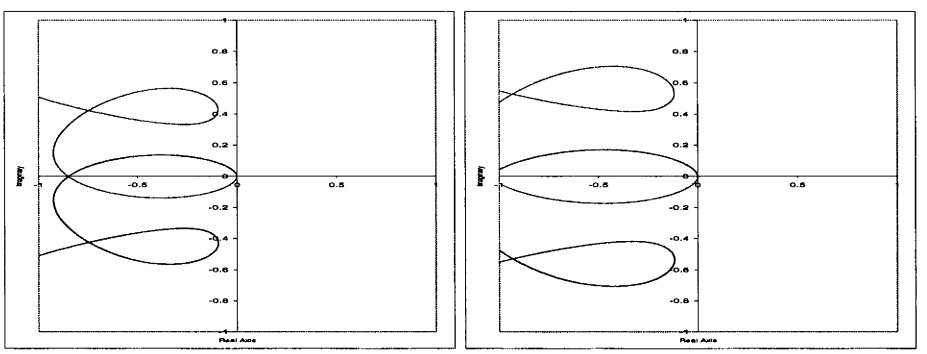

(c) d=0.4 (d) d=0.5

Figure 5.21: Nyquist plot showing stability for four values of the main gain of the cavity controller corresponding to the parameter d in the model $a = 0.95$, $b = 0.8$, $c = 0.95$, $\gamma = 0.5$.

reducing the PF gain also increases the stability by increasing the gain and phase margins. However, in practice it was found that size of the residual error signal was larger at smaller PF gains, indicating a poorer lock. This is indicative of a smaller locking bandwidth and less overall gain.

The locking magnitude and bandwidth is calculated from the closed loop response given by equation 5.10. Using the models for the various components of the

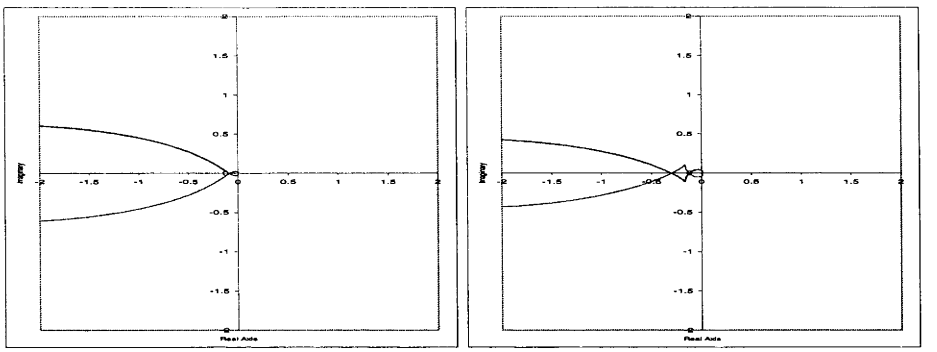

(a) a=0.1 (b) a=0.2

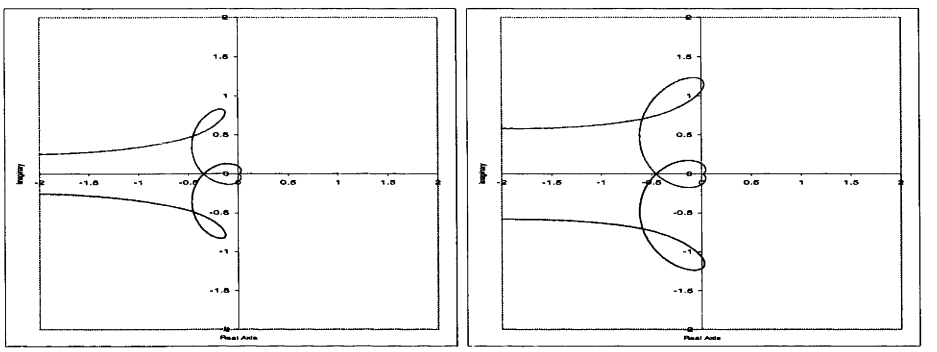

(c) a=0.6 (d) a=0.8

Figure 5.22: Nyquist plot indicating stability for four values of the proportional gain of the cavity controller corresponding to the parameter a in the model $b = 0.8$,$c = 0.95$,$d = 0.02$.

control loop $|G(\omega)_{closedloop}|$ can be recast into the form

$$G(\omega)_{openloop} = \frac{1 + r_1 r_2 r_3 r_4 \cos\phi + i r_1 r_2 r_3 r_4 \sin\phi}{1 + 2 r_1 r_2 r_3 r_4 \cos\phi + (r_1 r_2 r_3 r_4)^2} \tag{5.17}$$

$$|G(\omega)_{closedloop}| = \frac{1}{\sqrt{1 + 2 r_1 r_2 r_3 r_4 \cos\phi + (r_1 r_2 r_3 r_4)^2}}$$

$$\theta = \arctan\left(-\frac{r_1 r_2 r_3 r_4 \sin\phi}{1 + r_1 r_2 r_3 r_4 \cos\phi}\right)$$

Where $\phi = \theta_1 + \theta_2 + \theta_3 + \theta_4$ is the sum of the phase shifts of the controller, piezo, error signal detector and high voltage amplifier responses given previously, and r_1, r_2,r_3 and r_4 are their respective magnitudes. The attenuation of the cavity fre-

quency noise is calculated by looking at the magnitude of the closed loop transfer function i.e. the smaller the magnitude of the closed loop transfer function, the greater the attenuation at that frequency. A plot of the closed loop magnitude for typical experimental gains of the cavity controller is shown in figure 5.23. The figure

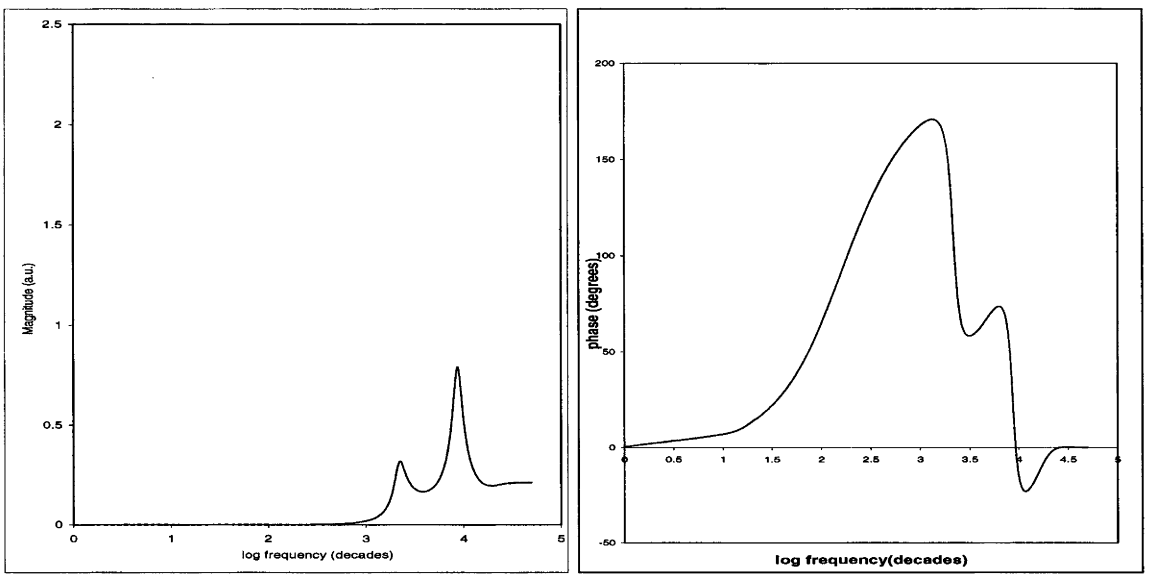

(a) closed loop magnitude

(b) closed loop phase

Figure 5.23: The gain and phase response of the closed loop transfer function for $a = 0.9, b = 0.8, c = 0.95, d = 0.02$

plots show significant attenuation below 1 kHz beyond which the transfer function displays peaks at 1.5 and around 10kHz, meaning that the feedback system is amplifying the noise at these frequencies. The phase plot shows that the phase does not reach 180 degrees. Thus the closed loop is stable. The two peaks are a result of the significant phase shifts at these frequencies due to the response of the controller and the resonance of the piezo. The bandwidth of the other components in the control loop are much larger than the cavity controller and piezo thus do not contribute significant phase shifts and are essentially constant over this frequency band. The locking performance can be more easily quantified by taking the integral of this

function and plotting it on a logarithmic scale and summing the contribution at each frequency giving the total attenuation in decibels. A plot of the log magnitude vs. frequency on a linear scale shown only up to 15kHz, is shown in figure 5.24. The plot shows more clearly that despite the peak at 1.5kHz, the input signal is

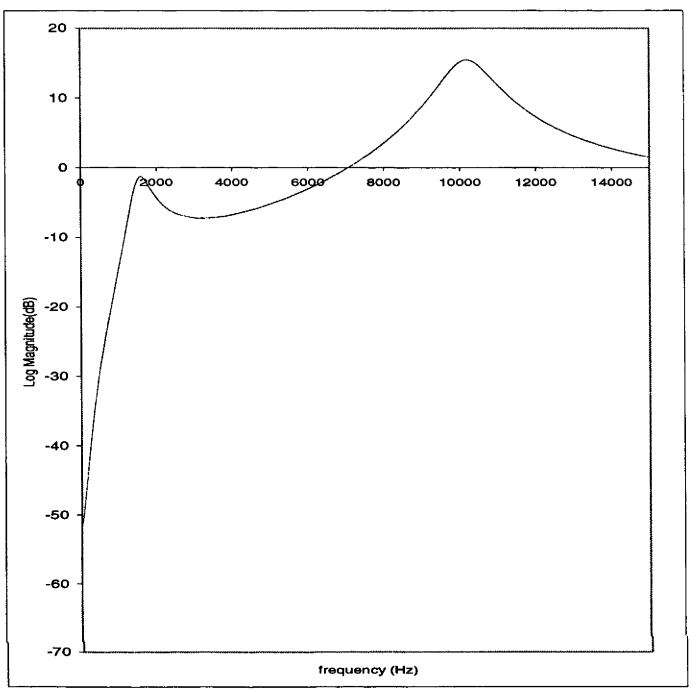

Figure 5.24: Magnitude in decibels vs linear frequency of closed loop magnitude function shown in figure 5.23. The magnitude scale has been normalised to 1 and evaluated as magnitude(dB)=20 log (magnitude).

still being attenuated up to 7kHz. The total attenuation for this plot is -1000dB over a 50kHz bandwidth.

In view of this theory, the operation of the cavity controller and its role in the control loop has been modelled and can be quantified in terms of its expected locking characteristics for the various experimental gains at the design stage. In particular it gives insight to the following points:

- The use of a high gain proportional stage enables greater error signal attenuation to be achieved given the limited bandwidth of the piezo, especially at the lower

frequencies.

- The Nyquist diagram can be used to identify causes of oscillation and to understand locking behaviour at various gain settings of the different control stages when the controller is used in feedback.
- Care must be taken when matching the responses of the high gain proportional stage and the lower gain proportional stages to avoid "holes" in the controller response which lead to an amplification of noise at that frequency when the control loop is closed.
- At the higher frequencies, minimisation of phase lag is important in providing superior locking performance.
- A peak in the closed loop frequency response occurs near the piezo resonance frequency, which amplifies the noise near the resonance frequency.

The theoretical model developed is used for comparison to results with the experimental data in the following section.

5.6 Locking performance and comparison with theory

This section presents the locking performance of the system and how it compares with theoretical results from section 5.5. In particular the intensity stability of the laser output is discussed and quantified, and how it relates to the locking performance of the feedback system. The function of each of the control stages in the experimental setup is shown and discussed. Finally, improvements in the system are discussed.

The usefulness of the laser system that has been developed in this thesis rests not only on the output power but equally on its intensity stability. The intensity stability depends on the ability of the control system to minimise the detuning between the Ti:Sapphire output and one of the cavity resonances over the measurement interval (which could be restated as the "stiffness" of the lock). In this case the

cavity linewidth is much larger than the Ti:Sapphire output, resulting in a straightforward doubling of the frequency linewidth at the 389nm output wavelength i.e. $\approx$ 1 MHz. This is satisfactory for the purposes of atom optics experiments since the laser linewidth is required to be less than the natural linewidth Γ (Γ = 1.5 MHz for the 3^3P state of helium). The output intensity and frequency stability are related through the Airy function of the cavity transmission. In cases where the two linewidths were nearly equal the output intensity noise would be determined by the overlap integral of the Airy functions of the two linewidth profiles.

The properties of the cavity provide a frequency reference by which the error signals can be compared and the relative frequency stability be determined, which are summarised in table 5.1. The FWHM of the cavity transmission peak determines

Optical Path (mm)	FSR (MHz)	$\mathcal{F}$	FWHM (MHz)
809	371	115	3.2

Table 5.1: Frequency specifications of 389nm frequency doubling cavity.

the width of the cavity error signals. The gradient at the center of the error signal determines the relative frequency stability of the cavity when locked. The gradient at the center of the dispersion signal for the series of traces shown in Figure 5.25 is $\approx$ 17 MHz/V. The magnitude of the locked error signal is $\approx$ 26mV in the right hand trace of Figure 5.26, which is equivalent to a $\approx$ 430kHz frequency deviation on a 8ms timescale (ignoring the transients due to the mains supply). The root mean squared (RMS) value of this signal represents the average value of the deviation from the lock point, it is $\approx$ 150kHz taken over a 25ms period. The dominant features in the locked signal are transients at 50Hz due to the mains supply and oscillations at 2 and 30kHz measured on a spectrum analyser. The former cannot be easily removed without filtering of the mains supply with large capacitors. The oscillation at 2 kHz is due to a dip in the cavity controller's response. This occurs

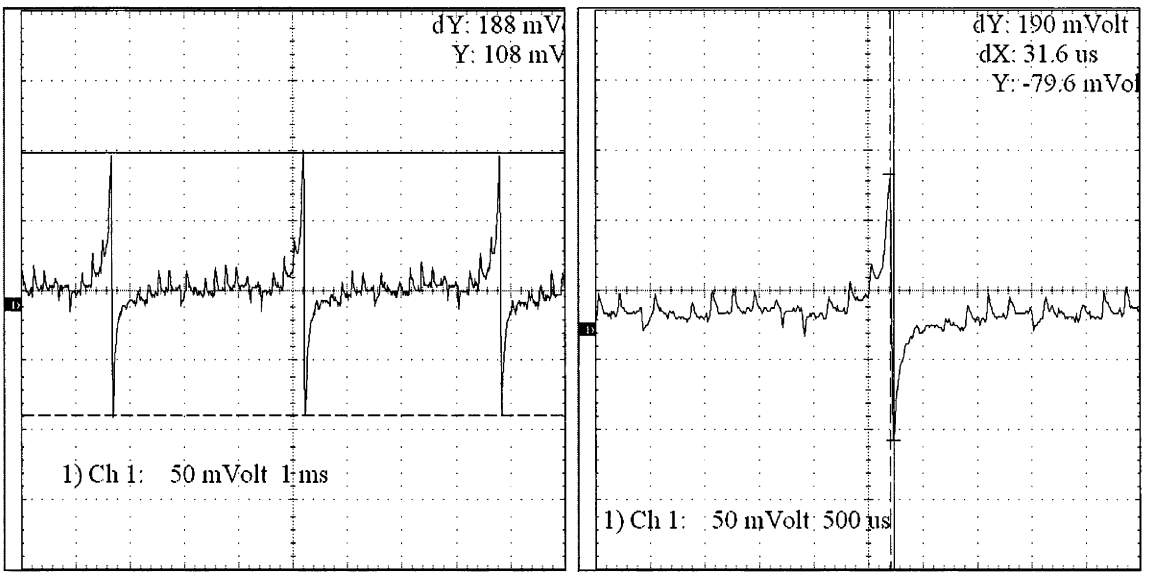

(a) scanning signal

(b) closeup

Figure 5.25: Time series of the error signals when scanning the cavity.

at the point where the low gain proportional stage begins to make up the gain of the high gain proportional stage, which suggests directions for improvement in the future. The oscillation around 30kHz is due to frequency noise in the Ti:Sapphire output since it was found that the error signal was greatly reduced when the frequency locking of the Ti:Sapphire was turned off. This was confirmed by the FFT (Fast-Fourier Transform) spectrum that showed a significant reduction in the magnitude at this frequency. The cavity controller has no gain at this frequency and is unable to counteract it. The oscillation at 30kHz can not be eliminated without further frequency stabilisation of the Ti:Sapphire output.

The intensity stability of the output is closely coupled to the frequency stability of the cavity because locking fixes the resonant cavity frequency to one of the cavity transmission fringes. The intensity stability however is only approximately linear to the cavity frequency stability since the output intensity is not linear near the peak

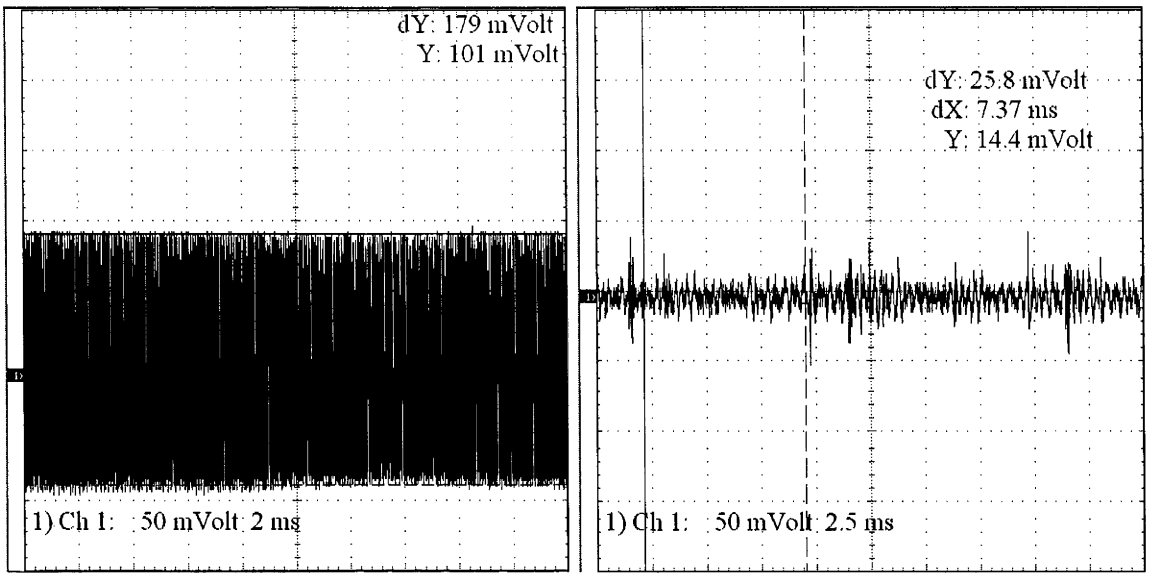

(a) oscillating signal

(b) locked signal

Figure 5.26: Time series showing the error signals when the cavity is partially and fully locked, the measurement bandwidth is 0.5 MHz

of the transmission fringe. The relationship between the intensity and frequency stability can be estimated through the use of the Airy transmission function of the cavity fringes shown in figure 5.27. Figure 5.27 shows that a magnitude of 10% intensity noise corresponds to locking to within $\approx$ 500kHz of the peak, and 50% intensity noise corresponds to locking to within half of the cavity linewidth.

Experimentally, the method which was used to measure the intensity stability takes the ratio of the magnitude of the AC component relative to the DC component of the signal on a photodiode:

$$\frac{\Delta V}{V_{av}} = \frac{2\sqrt{1/\tau \int_t^{t+\tau} (V_{av} - V(t))^2 dt}}{V_{av}} = \frac{2V_{RMS}}{V_{av}} \qquad (5.18)$$

$$\text{where } V_{av} = \frac{1}{\tau}\int_t^{t+\tau} V(t)dt$$

The DC component is represented by the mean value of the voltage V_{av} generated by the photodiode which is linear with the incident intensity of the light if it is below

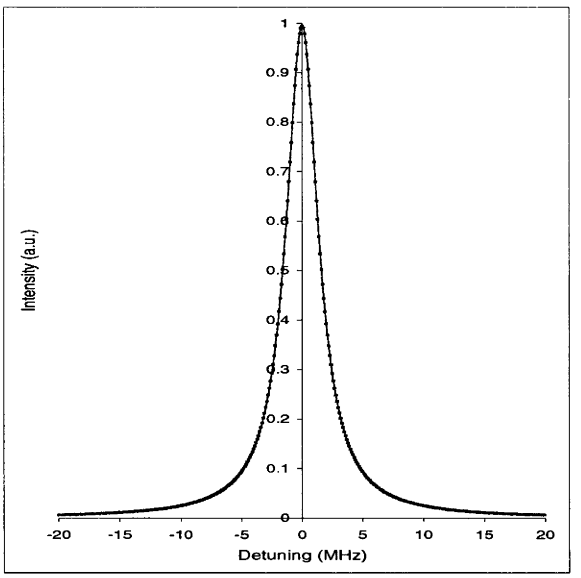

Figure 5.27: Calculated Airy transmission function of the cavity showing the relationship between the normalised intensity and detuning from resonance. The FWHM is 3.2 MHz.

the saturation intensity of the photodiode. The AC component is the difference between this average value and the instantanenous voltage V(t). Because the voltage V(t) is a function of time, both the average power and the intensity noise expressed as a percentage $\Delta V/V_{av} \times \%$ will depend on the length of the measurement period τ. The measurement bandwidth needs to be specified since the photodetector in combination with the electronics may bias the observed intensity by rolling off the noise in the signal past the cut-off frequency. An example trace of the intensity output taken using a homebuilt photodetector is shown in figure 5.28. The relative intensity stability for the trace marked 1 in figure 5.28 is $\approx$ 10% on a timescale of 2.5ms and a bandwidth of 0.5MHz. This would indicate that currently the intensity stability of the system is most likely limited by the Ti:Sapphire intensity noise which is around 5%, which is in agreement with the observed noise magnitude at 389nm. This is confirmed by the trace on the right hand side (the internal lock of the Ti:Sapphire has been disabled) where the intensity noise has almost halved.

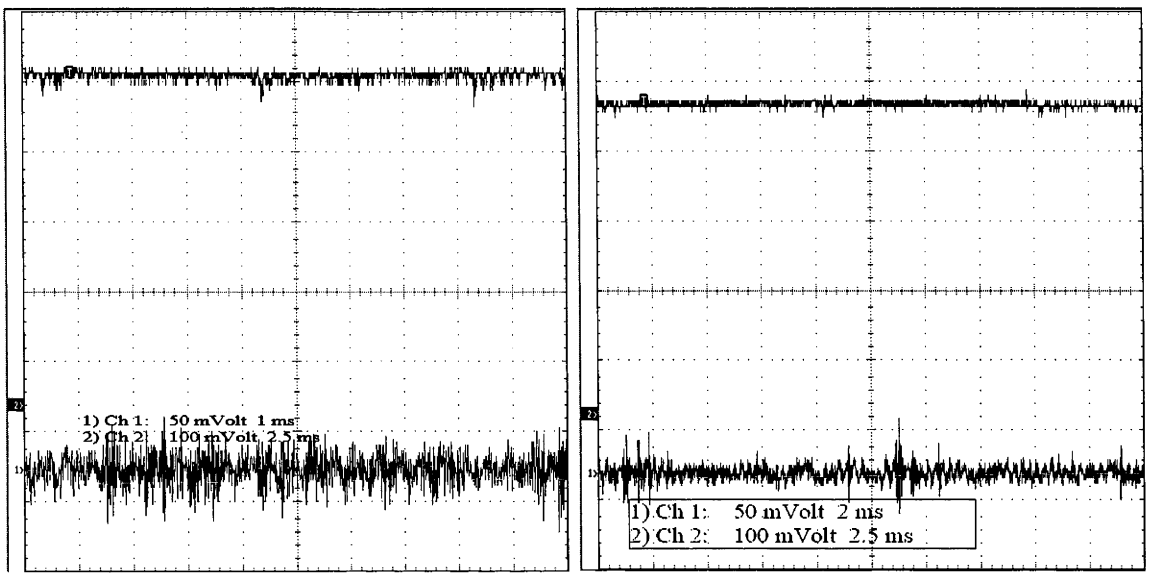

(a) lock on

(b) lock off

Figure 5.28: Traces of the intensity when the cavity it locked to the laser output using a homebuilt photodetector at 778nm. The traces marked (1) are the residual error signals and (2) the intensity of the 389nm output recorded with the photodiode. The traces in the left hand figure are taken with the internal frequency stabilisation of the Ti:Sapphire turned on. The right hand figure has the internal frequency stabilisation of the Ti:Sapphire turned off.

The signal to noise ratio in the right hand trace (Figure 5.28) is comparable to that of the error signals of the cavity when scanned, suggesting that the control system is near optimal. The current intensity stability of 10% suggests that the Ti:Sapphire output is being locked to within 500kHz of the peak transmission of the cavity by comparison with the shape near the peak of the Airy function in figure 5.27.

The residual error signals can also be analysed in the frequency domain by the use of the Fourier transform which decomposes a periodic signal into a series of sine waves at different frequencies with various amplitudes. This is performed by the Tektronix TDS210 digital oscilloscope with math module installed. It takes the central 2048 points of the time domain waveform and decomposes it into 1024 fre-

quency bands (with appropriate windowing) up to half the Nyquist frequency which is the sampling rate. This enables easier comparison between the calculated closed loop transfer function and the experimental residual locking signals obtained.

In order to better understand the role of each control element in the feedback loop, the cavity was locked and the gain of a particular stage was varied, until the controller locks without having to change the overall gain. Firstly, the laser was locked with the controller having maximal integral control, then proportional was added to minimise the residual error signal. Finally, the proportional filter control was added giving the smallest overall error signal. Traces of the time series of the residual error signal and intensity output on the photodiode are shown in Figure 5.29. It can be seen from the series of traces that adding the proportional stage to the integral attenuates the higher frequency components of the signal the most. However it also amplifies certain lower frequency components. The traces of the amplitude clearly show much poorer locking with just integral control as compared with the use of proportional stages. However it would seem on first glance that integral control is somewhat better than proportional+integral (PI) control.

The signals can be more clearly analysed in frequency space. Figure 5.30 shows the spectra of the residual locking signals, along with the calculated closed loop functions with the same experimental parameters as the traces in figure 5.30. It can be seen that with PPFI control the magnitude of the error signal is the smallest up to around 20kHz. The reasons for this is the large gain at frequencies below 10kHz which cancels out most the dominant sources of noise from laboratory equipment (such as vacuum pumps and the laminar airflow unit) which appear in the I control trace. This has the secondary effect of reducing the residual error signal at higher frequencies despite the lack of locking gain at these frequencies. This is simply the result of feedback control. The total gain of the controller is less with just PI control so the spectrum shows less attenuation in comparison to the PPFI case. It does however introduce a spike at around 2 kHz which is also seen in the

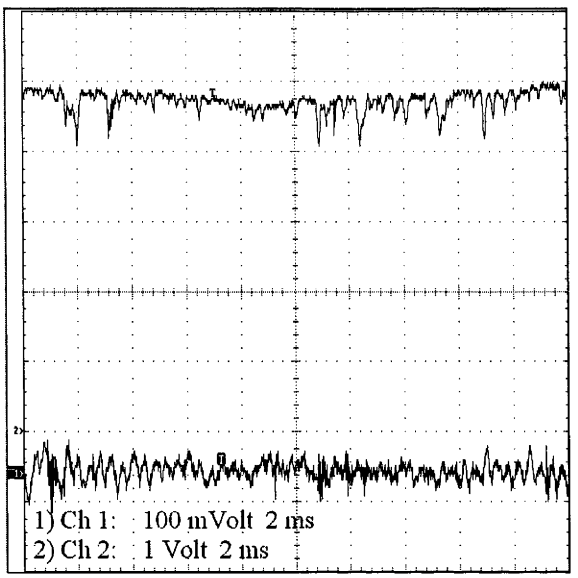

(a) I-control

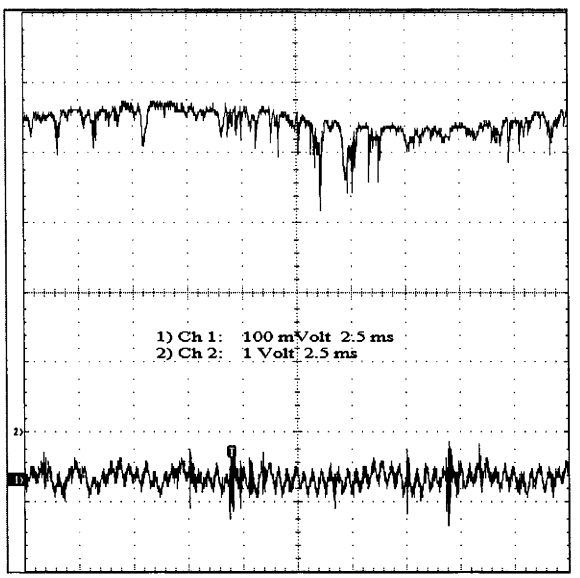

(b) PI-control

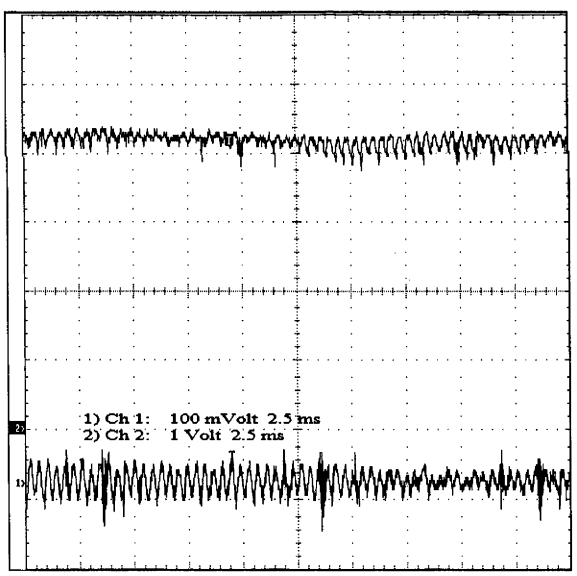

(c) PPFI-control

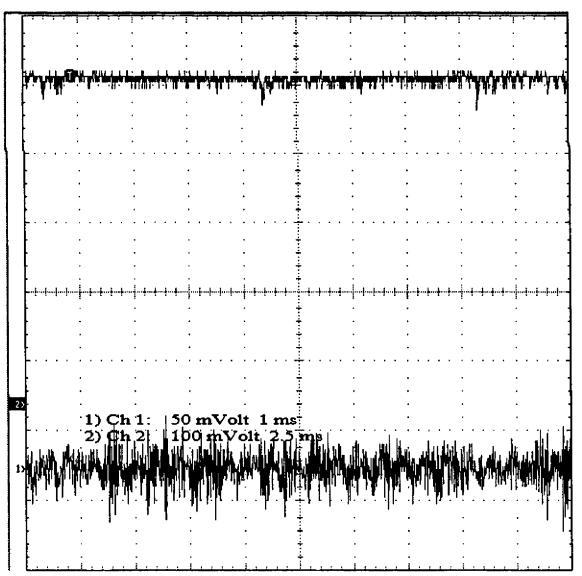

(d) PPFI-optimal

Figure 5.29: Time series of residual locking signal and intensity showing effect of adding each control element into the control loop. The top trace in each figure is the intensity of the frequency doubled output recorded with a photodiode and the bottom trace is the residual error signal. The bottom right hand trace shows the intensity stability achieved with PPFI control with the optimal gain parameters.

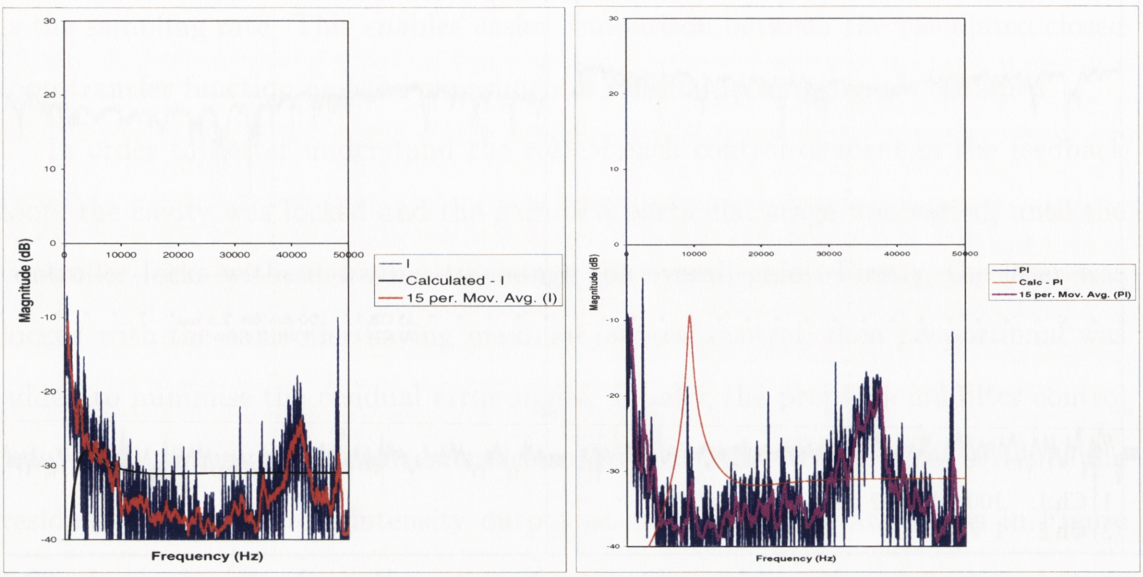

(a) I-control

(b) PI-control

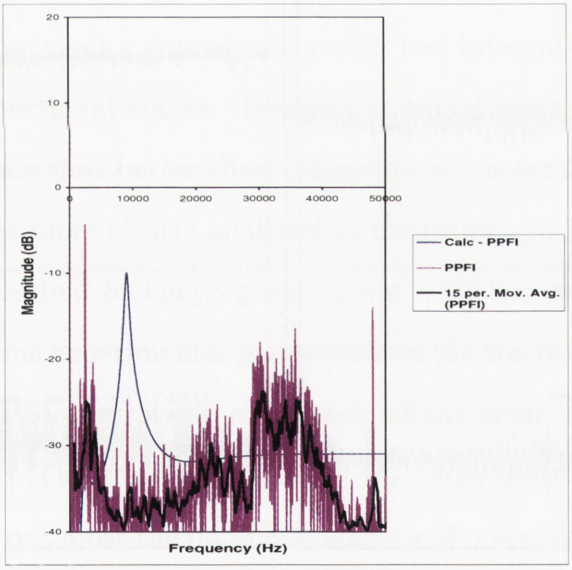

(c) PPFI-control

Figure 5.30: Spectra of residual error signals for the total control loop for the case of I, PI and PPFI control. The calculated closed loop magnitude and a 15 point moving average for the experimental data is shown for each case. The magnitude scale is normalised to 1 V_{RMS}.

PI control trace shown in green. This is due to a drop out at this frequency in the amplitude response of the controller. The calculated trace for PPFI control shows a peak at this frequency. Another prominent feature is at 10kHz which is likely due to resonance of the piezo which fits with the calculated closed loop amplitude discussed in section 5.6. The model also predicts the apparent shifting in frequency of the spectra between the case with PI and PPFI control which is most likely an effect of slightly smaller phase shift at each frequency with PPFI control. Also the introduction of proportional stages shifts the Ti:Sapphire intensity noise which consists of a broad distribution around 30kHz to lower frequencies. A feature that is characteristic of many feedback systems is that as the locking gain is increased within the bandwidth of the control loop (in this case 0-10kHz), there is an increase in noise at higher frequencies (due to the phase lag as the gain is rolled off) which could possibly explain why the broad feature around 20kHz is larger when the proportional and proportional filter gain stages are used [42].

The model predicts some of the features seen in the spectra and gives approximately the correct average attenuation ($\approx$ -30dB). However it does not predict the overall shape of the spectra for several reasons:

- Frequencies approaching 0 Hz are dominated by transistor noise from the electrical components which has a 1/f spectrum.

- Johnson noise due to random thermal movement of the electrons has not been taken into account.

- Influence of the Ti:Sapphire output intensity noise is excluded.

- Constant input magnitude is used across all frequencies, which is unrealistic (the magnitude of noise sources in the laboratory is not constant across the spectrum).

- The model is static in that it does not account for the change in magnitude of the error signal with time.

5.6.1 Conclusion

It can be concluded that with the implementation of relatively straightforward feedback controller a cw source of 389nm radiation has been realised. From the traces of the residual error signals and the intensity noise, it can be confirmed that the 389nm output from the cavity is locked with 10% intensity noise which corresponds to locking the cavity to within $\approx$ 500kHz of the Ti:Sapphire output. This is the best that is currently possible due to the 5% intensity noise of the Ti:Sapphire output with the internal frequency locking enabled. An appropriate model for the total control loop has been developed to explain qualitatively the behaviour of the system and shows good quantitative agreement with experimental spectra of the residual error signal. The development of the control system has enabled the system to be used for the saturation absorption spectroscopy experiments in helium, whose results are to be presented in the next chapter.

The system could be improved in several ways. In particular, further investigation of the controller characteristics by the use of the developed model could yield improvements in locking bandwidth and gain. The extension of the piezo in normal operation is very small compared to its maximal extension which is rarely used. A smaller piezo-electric stack could be used which would increase its usable bandwidth by increasing the resonant frequency. Intensity stabilization of the Ti:Sapphire output would greatly decrease the noise present in the output of the 389nm beam through tighter locking to the cavity fringe. The passive stability of the cavity could be increased by greater isolation of the cavity from vibrations in the lab.

CHAPTER 6

Saturation absorption spectroscopy of 3^3P state of helium in a DC discharge

6.1 Introduction

The observation and study of atomic and molecular states is the field of spectroscopy. In particular laser spectroscopy concerns itself with the interaction of the atomic levels under excitation with laser radiation. The advent of the laser has enabled a huge expansion of the field of spectroscopy by providing a means with which to probe atomic and molecular states with unprecedented resolution [43]. The spectral lines of atoms and molecules provide a wealth of information about the quantum behaviour of the systems themselves, as well as their surrounding environment. This has enabled the expansion of applications of spectroscopy, as well providing better comparison with theory.

Experiments in atom optics rely on the resonant or near resonant interaction of the atoms with the laser field. Transition frequencies of atomic systems do not change over time and can thus be used to provide absolute frequency references. While the linewidth of many laser systems can be made much smaller than the natural linewidth of the atomic transitions being probed e.g. (Γ = 1.6 MHz for He $2^3S \rightarrow 2^3P$), their absolute frequency is prone to drift over 100's

of MHz per hour due to temperature effects [36]. Thus the laser frequency is often locked to an atomic transition to enable both long interaction times between atoms and the laser field, and to provide an absolute frequency reference [44], [7],[8],[4], [51]. Usually the observed linewidth is greater than the natural linewidth due to other processes which broaden the transition.

6.2 Line broadening mechanisms

Three commonly observed line broadening mechanisms are pressure broadening, Doppler broadening and power broadening.

Pressure broadening is an example of homogeneous line broadening by which all atoms in the sample are affected equally [45]. It is caused by atoms undergoing collisions with other atoms in the sample or with the container walls which shift the energy levels through attractive or repulsive interactions. This creates a shift $\Delta\nu_0$ in the transition frequency $\nu = (E_2 - E_1)/\hbar$ between the two electronic levels of the atom. Alternatively, it can be regarded as a phase disturbance of the emitted wave if the mean time between collisions τ_c is much greater than timescale on which a single collision occurs. This phase disturbance manifests itself as a broadening in the linewidth of the emitted light. The associated frequency broadening is inversely proportional to the time between collisions τ_c

$$\Delta\omega_0 = \frac{1}{\pi\tau_c} \tag{6.1}$$

The lineshape due to pressure broadening is a Lorentzian function with the full width at half maximum (FWHM) given by $\Delta\omega_0$. An order of magnitude of the time between collisions can be made by taking the ratio of the mean free path and the mean velocity v_{th} due to thermal movement of the atoms where

$$v_{th} = \sqrt{\frac{8kT}{\pi M}} \tag{6.2}$$

$$\text{and } \tau_c \simeq \sqrt{\frac{MkT}{16\pi}}\frac{1}{pa^2}$$

Here M is the mass of the atom, T is the temperature, p is the pressure, a is the effective size of the atom (around $1\text{x}10^{-10}$ metres) and k is Boltzmann's constant. For helium at room temperature the broadening is $\sim$ 6 MHz/Torr from equation 6.2. At low pressures i.e. $\ll$ 1 Torr this is effect is small and simply adds to the natural linewidth (1.6 MHz).

A much more dominant effect in gas discharges, such as used to create metastable helium is Doppler broadening. This is an inhomogeneous process because it depends on the velocity of the individual atom in the atomic sample, which in a gas of thermal atoms has a Maxwell-Boltzmann distribution peaked at the mean thermal velocity. Due to the fact that the atoms are moving with respect to the laboratory, there is an observed frequency shift of the central transition frequency ω_0 to $\omega' = \omega_0(1 \pm v/c)$, where the v is the velocity of the atom. For a laser to be resonant with the transition, it must be detuned away from resonance by an amount $\mp\omega_0 v/c$. Since there is a distribution of velocities in the sample, there is a corresponding distribution in the number atoms whose Doppler shifted frequency is ω. In the rest frame of the atom, the distribution is peaked around the central transition frequency ω_0 given by

$$g(\omega - \omega_0) = \frac{1}{\omega_0}(\frac{Mc^2}{2\pi kT})^{1/2}\exp\{-\frac{Mc^2}{2kT}\frac{(\omega-\omega_0)^2}{\omega_0^2}\} \tag{6.3}$$

and the FWHM of the resulting Gaussian lineshape is

$$\Delta\omega_0 = 2\frac{\omega_0}{c}(\frac{2kT}{M}\ln 2)^{1/2}$$

Thus the Doppler width is proportional to the central resonant frequency and the square root of the temperature, while being inversely proportional to the square root of the atomic mass M. Hence it is highest for light elements such as helium and hydrogen. The combination of Doppler broadening and homogeneous line broadening yields a Voigt profile, which is a convolution of the Gaussian profile with the Lorentzian profile of the homogeneously broadened transition [43].

The third common line broadening is power broadening (also called saturation broadening). This occurs when the laser intensity is much greater than the satura-

tion intensity I_s given by [1]

$$I_s = \frac{\pi hc}{3\lambda^3 \tau} \tag{6.4}$$

When $I_s \to \infty$ the two electronic states become equally populated, and at lower intensities excited state population fraction ρ_{ee} becomes

$$\rho_{ee} = \frac{s}{2(1+s)} = \frac{1}{2}\frac{s_0}{1+s_0+(2\Delta/\gamma)^2} \tag{6.5}$$

Here s is the saturation parameter, s_0 is the on resonance saturation parameter $s_0 = I/I_s$ where I is the incident intensity, $\gamma = 1/\tau$ is the natural linewidth, and $\Delta = (\omega - \omega_0)$ is the detuning from resonance. As $s \gg 1$, ρ_{ee} approaches 1/2. Since the upper state population decays at a rate γ the scattering rate per atom is

$$\gamma_p = \gamma\rho_{ee} = \frac{s_0}{2}\frac{\gamma}{1+s_0+(2\Delta/\gamma)^2} \tag{6.6}$$

The scattering rate saturates to $\gamma/2$ when $s_0 \gg 1$. This equation can be rewritten as

$$\gamma_p = (\frac{s_0}{1+s_0})(\frac{\gamma/2}{1+(2\Delta/\gamma')^2} \tag{6.7}$$

Here $\gamma' = \gamma\sqrt{1+s_0}$ is the linewidth broadened by saturation. If we plot γ_p as a function of the detuning Δ we obtain a Lorentzian line shape broadened by a factor $\gamma\sqrt{1+s_0}$. This is commonly encountered in experiments where laser beams high above saturation are used. Saturation can also be exploited to obtain Doppler-free linewidths from a gaseous sample or a plasma discharge by burning a "hole" in the spectrum of the material. This is the principle behind saturated absorption spectroscopy used in the experimental setup.

6.3 Saturated Absorption Spectroscopy

Saturation absorption spectroscopy is a technique that is used to observe homogeneous linewidths (approaching the natural linewidth) in situations where inhomogeneous Doppler broadening dominates. Two beams are used: one to saturate

the transition in the sample and a weaker probe beam to scan across the saturated absorption profile. As discussed previously, the frequency distribution of a sample of thermal atoms has a Gaussian profile. When the sample is probed by a single, weak ($s_0 \ll 1$) laser beam of frequency ω, the absorption by the atoms depends on the detuning from resonance in a manner given by equation 6.3 due to the Doppler shift. However, if another laser beam is introduced at $\omega = \omega_0 + \Delta\omega$ that is sufficiently intense (i.e. $s_0 = I/I_s \gg 1$), then absorption by atoms belonging to a velocity group $v = (\Delta\omega)/k$ is decreased as a result of saturation since there are fewer atoms in the lower state. The resultant absorption profile is still Gaussian but has a hole at $\omega_s = \omega_0 - \Delta\omega$, the saturating laser frequency as shown in figure 6.1. The width of this hole is given by the power broadened width $\gamma' = \gamma\sqrt{1+s_0}$

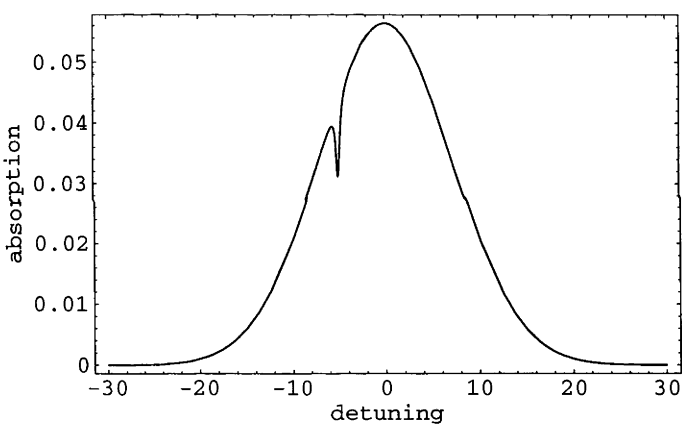

Figure 6.1: Doppler absorption profile with hole burned at saturating laser frequency $\omega_s = \omega_0 - \Delta\omega$.

plus other homogeneous sources, where the power is that of the saturating laser and the depth is $4s_0/\gamma'$. In a standing wave saturating field comprising two counter-propagating beams, there will be two holes burnt in the lower state population for atoms with velocities $v = \pm(\Delta\omega)/k$, because of opposing Doppler shifts as shown in figure 6.2. If the standing wave laser frequency ω is scanned, the two holes will coincide when $\omega = \omega_0$, which corresponds to atoms moving with zero velocity. This

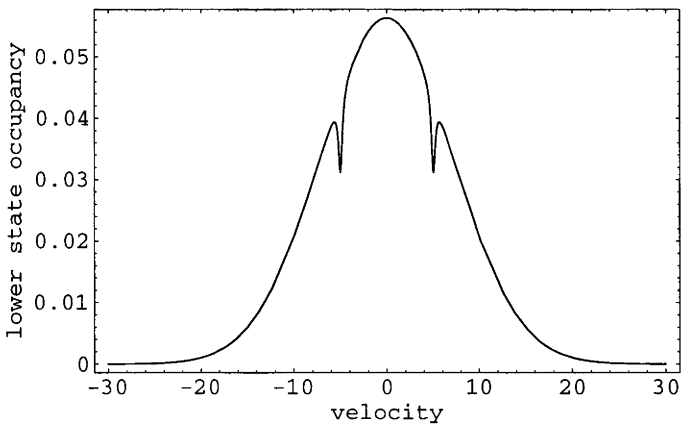

Figure 6.2: Lower state velocity distribution with holes burned at $\pm(\Delta\omega)/k$ by counterpropagating laser beams.

yields a decrease in the absorption at ω_0 relative to the rest of the profile - the so-called Lamb dip shown in figure 6.3. The Lamb dip width is determined by the

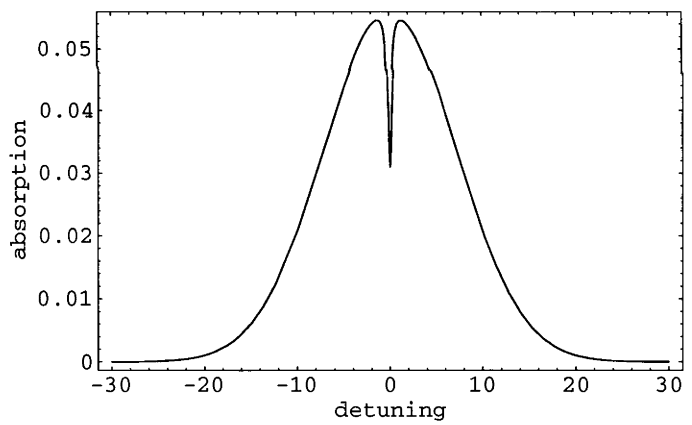

Figure 6.3: Saturated absorption profile with Lamb dip burned at ω_0.

saturation broadened profile given by $\gamma' = \gamma\sqrt{1+s_0}$, plus any other homogeneous broadening such as pressure broadening. Since this technique cannot remove homogeneous broadening mechanisms, they must be minimised in order to resolve the natural linewidth. This technique has been successfully used to perform frequency

locking of lasers to the $2^3S - 2^3P$ transition and (as in this thesis) the $2^3S - 3^3P$ transition in metastable helium.

6.4 Laser frequency locking in a DC discharge

The technique developed in the Atom Manipulation Laboratory involves the use of saturated absorption spectroscopy in a DC discharge cell [44]. This is used to lock the output of the SDL-6702 R diode lasers to the $2^3S \rightarrow 2^3P$ cooling transition of He* at 1083nm on the main beamline used for atom experiments. The technique utilises the interaction of intense laser light with helium metastables. The laser passes through a polarising beamsplitter (PBS) cube, and a $\lambda/4$ plate is used to drive σ transitions in the first pass through discharge cell, before being retroflected by a mirror. The incoming beam acts as the saturating beam and the retroflected beam acts as the probe. The retroflected beam traverses the $\lambda/4$ plate twice, and thus its polarisation is rotated by $\pi/2$ relative to the incoming beam. The PBS cube then deflects the return beam at right angles to the incoming beam. The intensity of the probe beam is monitored by a photodiode as the laser frequency is scanned. An absorption signal similar to 6.3 is observed. Metastable helium has three substates at 1083nm corresponding to total angular momentum number $j = 0, 1, 2$ of which $j = 1$ and $j = 2$ are 2.3 GHz apart and are observed experimentally as two partially overlapped Doppler profiles with Lamb dips at their respective centers. A crossover peak occurs halfway between each pair of transitions, and the width of the absorption dips is measured to be 50MHz. Crossover resonances are a result of atoms moving at velocities such that Doppler shift drives them into different upper states by the laser beams opposite directions.

To obtain a locking signal a pair of coils placed close to the cell volume are used to dither the frequency of the transitions via the Zeeman shift, at a rate of several kHz. The phase is detected with a lock-in amplifier, giving a dispersive error signal.

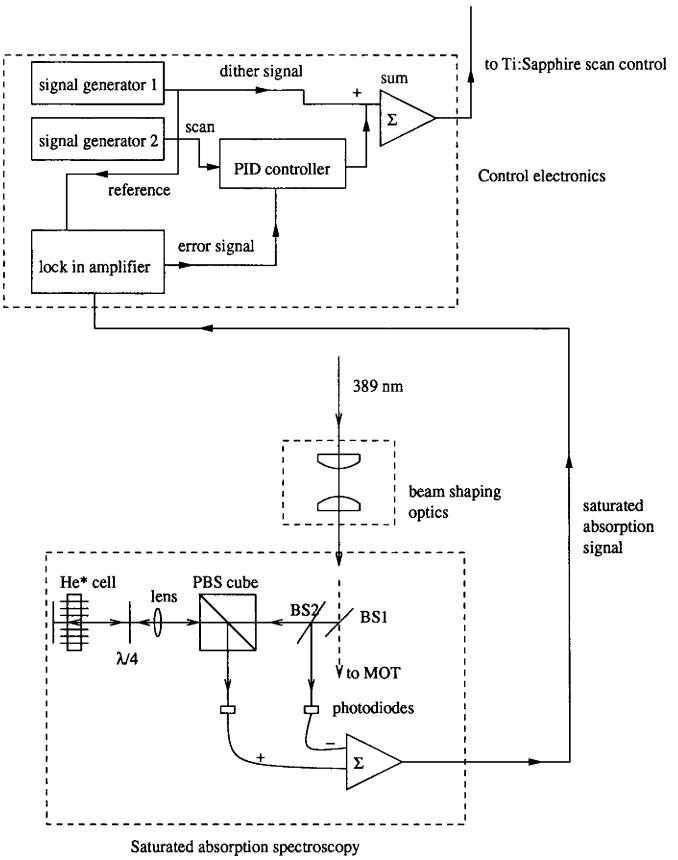

Figure 6.4: Experimental setup for saturated absorption spectroscopy at 389nm. The diagram shows the finalised optics setup and associated electronics.

Detuning from resonance can also be achieved by adding a DC component to the coils. This system enables the laser to be locked to the transitions for many hours.

The 1083 nm setup described was mostly adopted to the 389nm system and the final version is shown in figure 6.4. The differences between the 1083nm and 389nm setups are due to several factors. Firstly, an intrinsic and thus unavoidable problem is the smaller absorption cross section. Reference [1] gives the cross section σ_{eg} for resonantly scattering light as

$$\sigma_{eg} = \frac{\hbar\omega\gamma}{2I_s} = \frac{3\lambda^2}{2\pi} \tag{6.8}$$

Due to the wavelength differences, $\sigma_{1083} = 7.75\sigma_{389}$. Hence less light will be scattered by an equal number of atoms in the 389nm cell, and thus a smaller signal will be observed at equal laser powers. This consequently leads to higher laser powers being used. Secondly, there was a much larger intensity noise on the 389nm beam than the 1083 nm beam, which could be reduced but not be eliminated. This is both a consequence of the Ti:Sapphire intensity noise amplified by the non-linear conversion process, as well as instabilities in the external doubling cavity. The Ti:Sapphire laser also varied slightly in intensity when the frequency was scanned. For these reasons two photodiodes were used to subtract the common mode noise. Due to the greater noise levels, Zeeman shifting of the transitions was also harder to observe. Instead, the Ti:Sapphire laser frequency was dithered which resulted in the intensity stability of the laser being slightly compromised due to the greater frequency offset between the cavity and Ti:Sapphire output (around 800 kHz) to obtain the error signals. Details of the experimental procedure and the obtained signals are presented in the following section.

6.5 Saturated Absorption Spectroscopy of 3^3P state of helium in a DC discharge

In this section the results obtained by saturation absorption spectroscopy of helium at the 389nm transition will be presented. This represents a significant development of the existing system in that this had not been achieved previously. An error signal was subsequently extracted by dithering the Ti:Sapphire frequency. The UV output was subsequently locked to one of the substates of the 3^3P transition.

The procedure that was developed relies on the removal of this intensity noise from the laser output which from the previous chapter was found to be of the order of 10 %. This is performed electronically by the use of a two port photodiode that was developed to remove common mode noise in the saturated absorption signal.

The final procedure for obtaining the saturated absorption signals and error signals is outlined below. The experimental setup is that shown in the previous section.

(1) Firstly, the UV output beam was collimated using a single AR coated spherical lens f=150mm placed one focal length from the center of the crystal. This produces an almost perfectly collimated beam that is however elliptical with a 3:1 ellipticity in vertical direction. This is corrected by a pair of cylindrical lenses (f=150mm and f=50mm) used to focus the vertical dimension to give an approximately spherical output beam. The 389nm beam is now roughly collimated with full angle of divergence of 3.3×10^{-4} and 3.7×10^{-4} radians in the horizontal and vertical dimensions, and a 300 μm diameter.

(2) The 389nm beam is aligned using the steering mirrors to be in the middle of the gas cell window and perpendicular to it. The beam splitter (60/40) is inserted and is aligned to reflect part of the beam towards one port of the split photodetector.

(3) The polarising beam splitter cube is placed after the beam splitter followed by the $\lambda/4$ plate. An AR coated lens is placed before the gas cell so that it focuses the beam on to the retroreflecting mirror, thus ensuring the beam is the same size on both passes through the gas cell. The retroreflecting mirror is aligned to overlap the beam back onto itself, using the fact that the 389nm light visibly fluoresces blue in all the optics. Due to the additional rotation of the retroreflected beam by the $\lambda/4$ plate, the beam that goes through the gas cell is deflected by 90 degrees into the second port of the photodetector. The size of both beams in the ports of the photodetector is made approximately the same. If this is not the case, the collimation of the beam has to be repeated or the lens that focuses the beam into the gas cell needs to be adjusted. This ensures that the difference signal generated is mostly due to the absorption in the gas cell and not due to the different intensity of the two beams.

(4) The pressure in the gas cell was optimised at 0.8 Torr and the voltage on the

gas cell is turned up until the milliameter reads 40mA. The total power in the beam directed towards the gas cell is around 2-2.5mW. The magnitude of the photodiode signal is typically $\approx$ 2V at this power level. The beam that is reflected by the beam splitter is now blocked and the beam going towards the cavity is made to overlap onto itself, so that the input and output spots on the polarising beam splitter cube overlap. The angle adjustments on the beam splitter cube are now used to maximise the intensity entering the other port of the photodetector by monitoring the intensity on the CRO. The signal level should be the same as the other port, but with the opposite polarity.

(5) The Ti:Sapphire laser is tuned using the birefringent filter (coarse) and thin etalon offset (fine) using the Burleigh WA-1100 wavemeter to approximately 777.949 nm and adjusted for maximum power. A visible streak of fluorescence when the cavity is locked is then visible in the gas cell. The beam entering the normalising port of the photodetector is again blocked and the laser frequency tuned using the SCAN OFFSET control of the Ti:Sapphire control box until the output of the photodiode is minimum. This is the peak of the absorption of the 3^3P transition. The Ti:Sapphire scan range is then set to 0.8 GHz and scan frequency 1-4 Hz on the function generator set to triangle waveform and 5Vp-p amplitude. The Ti:Sapphire scan control knob is set to external which will start the laser frequency scan. The beam into the normalising port of the photodetector is then unblocked which causes the signal level of the photodiode output to drop to almost zero, due to the signal subtraction between the two beams. The voltage range on the CRO is set so that the magnitude of the noise is observable. The internal potentiometer controlling the gain of one of the photodetector ports is now adjusted with a screwdriver until the magnitude of the noise is a minimum. Typically, the residual noise on the signal is around 6-10mV. The cavity controller gains (in particular the proportional) might need to be adjusted so that the magnitude of the residual error signal remains constant while the DC level shifts up and down with the scan. Rotating

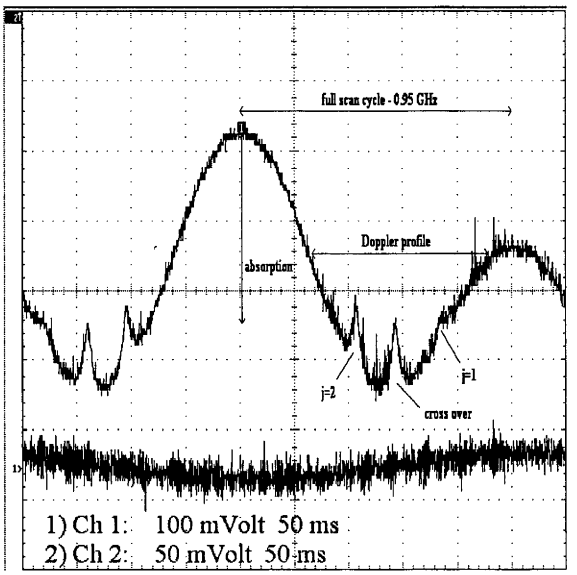

Figure 6.5: Saturated absorption signal of helium at 389nm obtained by scanning the Ti:Sapphire laser frequency 0.95GHz at 778nm. The top trace shows the resulting Doppler profile of the overlapped $j = 1, j = 2$ substates of the 3^3P transition, and the three Lamb dips. The middle one in the trace is the crossover. The trace shows two cycles of the Ti:Sapphire frequency scan. The direction of more absorption is indicated by the vertical arrow.

the input offset control of the controller might also decrease the intensity noise on the photodiode trace. A saturated absorption signal should now be visible on the oscilloscope trace similar to figure 6.5. The signal to noise ratio in the top trace of the figure is approximately 10:1. The three peaks shown in the figure are the j = 1,2 and the crossover peak which enables a calibration of the frequency scale since the crossover occurs at exactly half the $j = 1 \leftrightarrow j = 2$ separation of 659MHz. The $j = 1$ substate is barely visible in the figure since this trace was taken with the $\lambda/4$ plate placed after the gas cell, meaning that the atoms in the cell were seeing a linearly polarised laser beam driving π rather than σ transitions. It is possible to obtain Lamb dips larger than 50mV with this setup. If the peaks appear noisy, the balance of the photodiodes should be readjusted. If there is flattening of the peak

tops and distortion of the background (e.g. random shifting of the DC level) then an attenuator should be placed in front of both ports of the photodiode to prevent saturation or the gas cell needs refilling.

(6) To obtain the dispersive error signals an AC lock-in method is used. It involves dithering the Ti:Sapphire laser frequency with an AC signal which produces an amplitude modulation at the photodiode output. An analogue summer is used to sum the dithering signal with the scan signal which drives the Ti:Sapphire. The photodiode output and the dithering signal are both connected to the photodiode signal and reference inputs of the lock-in amplifier. The lock-in amplifier produces a signal that is proportional to the gradient of the photodiode signal at the frequency of the reference signal with a fixed relative phase. The gradient of the saturated absorption signal is the highest at the sides of the Lamb dips and has a zero crossing at the top of the dip. The dither signal should be set to 50mV and 500-550 Hz on the signal generator which appears on the cavity error signal as a modulation of the lock point. The reasons for the low modulation frequency is the low bandwidth of the Ti:Sapphire scan control input which is around 800Hz. It was found that frequencies lower and higher than the dither signal is strongly attenuated. A higher dither amplitude could be used but this may further compromise the output intensity stability. Thus the largest possible dispersive signal is desirable with the least amount of modulation, which requires the largest possible Lamb dips. With the dither on, and the scan running, the output of the lock-in amplifier produces three dispersive resonances with a fixed phase shown in 6.6. If the phase is not fixed then the reference input of the lock-in amplifier should be checked or there is not enough modulation depth. The controls of the lock-in amplifier should be adjusted to obtain the cleanest possible signals. If the phase is correct, it should be possible to lock to the middle of the dispersive signal using the PID controller. The controller is set to LOCK and manually scanned using the dispersive signals with the OFFSET control on the PID box (with the CRO channels connected to

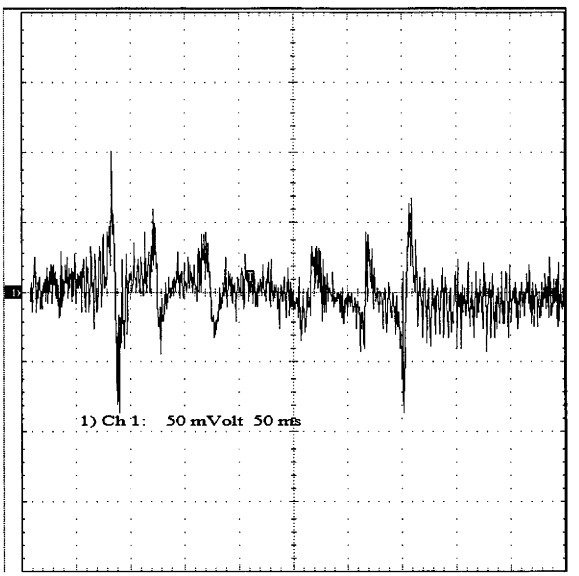

Figure 6.6: Error signal obtained through frequency modulation and lock in detection of the saturated absorption signal at 389nm. The trace shows three dispersive signals corresponding to the $j = 1, 2$ substates and the crossover of the 3^3P transition. The trace shows the error signal for the forward and backward phase of the scan.

the VERT output of the Ti:Sapphire control box and MONITOR output of the PID controller and set to XY mode). The integrator reset switch is closed and the integral and proportional gains of the controller adjusted to obtain the least amount of horizontal and vertical jitter of the lock point. It is possible to lock to any of the three resonances; the largest in figure 6.6 is the $j = 2$ cooling transition.

6.6 Results and Discussion

The saturated absorption signals obtained in the experiment enable the calibration of the laser output frequency on an absolute scale since the separation between individual substates of the 3^3P state is well known. Furthermore, the locking of the laser frequency to the transition ensures on-resonant excitation with He* atoms

being probed and the calibration can be used to set a known detuning from resonance.

The signals that were obtained depended strongly on the conditions in the DC discharge - in particular the temperature and pressure. The dominant effect is the Doppler broadening (due to heating of the metastables by plasma collisions) and is much larger than the frequency separation of the $j = 1 \leftrightarrow j = 2$ substates. Consequently, one broad absorption peak is observed whose FWHM was measured to be $\approx$ 6 GHz at 389nm. This value was obtained by scanning across the resonance and recording the intensity of the laser that has made two passes of the cell volume and recording the wavelength with the wavemeter (minimum resolution $\pm$ 0.001 nm). The plot of the relative absorption vs. the wavelength on the wavemeter is shown in figure 6.7. The absorption is relative to the transmitted intensity well

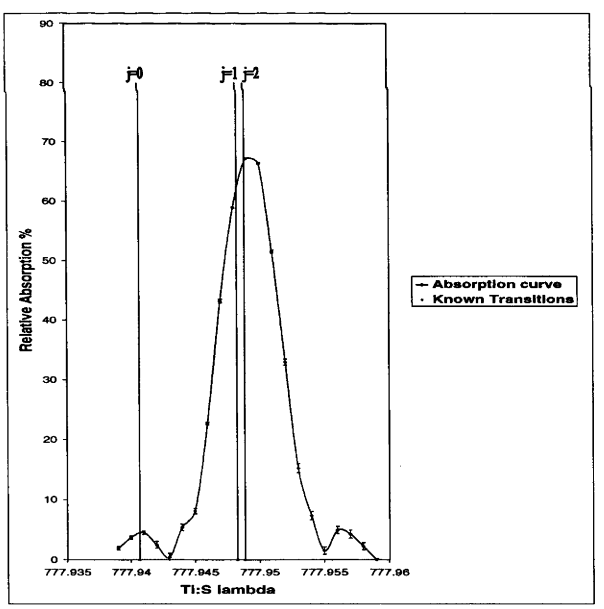

Figure 6.7: Relative absorption in the DC discharge cell at 389nm and pressure of 1.5 Torr vs Ti:Sapphire wavelength. FWHM of the peak is 3 GHz. Also shown are the positions of known transitions as given by [46].

away from resonance. The peak of the absorption is 70% at a pressure of 1.5 Torr and lies around 777.95 nm which corresponds to 388.98 nm in the UV. The $j = 0$ state which lies 8.773 GHz to the blue of the peak was not resolved probably due to the Doppler broadening and much smaller line strength of this transition. The line strength is proportional to the statistical weight of that level which is dependent on the total angular momentum quantum number as (2J+1) [47]. Thus the $j = 0$ exhibits the least absorption and the $j = 2$ the greatest absorption when excited by a laser beam.

To obtain the Doppler free linewidths saturation spectroscopy was used. This was initially attempted at higher pressures (1.5 Torr), however the saturated absorption signal that was obtained was very small. A laser beam above saturation $I > I_{sat}$ passing through a gas cell of resonant atoms is attenuated exponentially via Beer's Law [1]

$$I = I_0 e^{-\sigma \rho L} \tag{6.9}$$

where I_0 is the incident intensity, σ is the resonant cross-section, ρ is the effective column density and L is the length of the gas cell. The only controllable parameter in the He* gas cell is the effective column density which is altered by changing the size of the beam or the pressure in the cell. It was found that the best signals were obtained by using small beams which ensured saturation. The size of the beams used was around 300 μm which for the 2mW laser beam that was eventually used is $\approx 860 I_{sat}$. This is clearly enough to saturate the transition. However to maximise the signal, the percentage attenuation of the beam should not be too large so that there is still enough power in the return beam to obtain a large signal. To determine the optimal pressure a transmission measurement was performed. The laser power before and after the gas cell were measured with the laser frequency tuned to top of the absorption peak. By plotting the fraction of the power transmitted through the gas cell, it was determined whether to raise or lower the pressure in the cell and whether or not to focus the beam into the cell. The plot shown in figure 6.8 shows

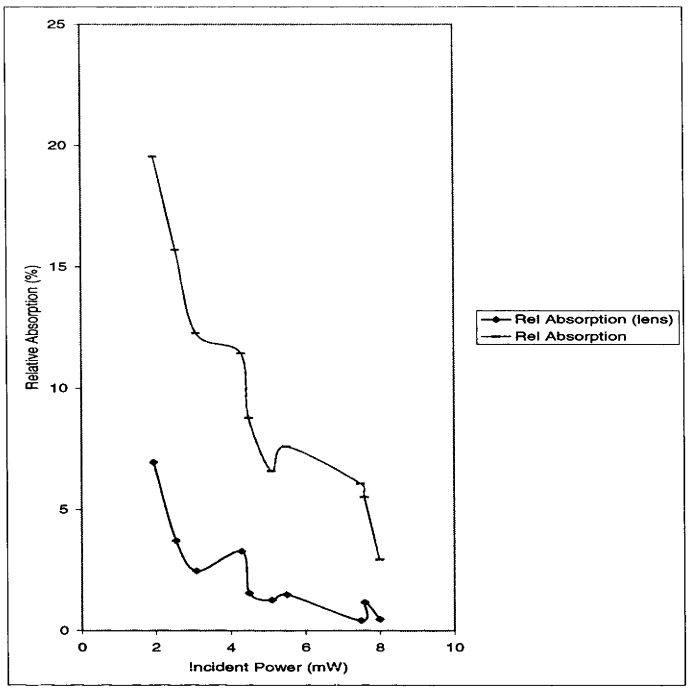

Figure 6.8: Relative absorption in the DC discharge cell at 389nm and pressure of 0.9 Torr vs incident laser power. Top curve - no focusing, bottom curve - focusing with a lens f=125mm.

the saturation of the atoms at higher powers as the relative absorption becomes smaller. It also shows that greater saturation is obtained at lower powers using a focusing lens. The trade-off however with using focusing is that greater saturation broadening of the Lamb dips occurs.

Lowering the pressure in the cell results in less power being needed to saturate the atoms, due to the lower density. It was also found that the beam was severely attenuated by the cell windows $\approx$ 57 % when the beam passed through the front and rear window. Three saturation signals are shown for three different pressures in figure 6.9. The best signals that were obtained in experiments resemble that of the figure for 0.9 Torr.

The change in the relative peak magnitudes for 0.8 Torr is due to the saturating beam being circularly polarised rather than linearly polarised for the other two

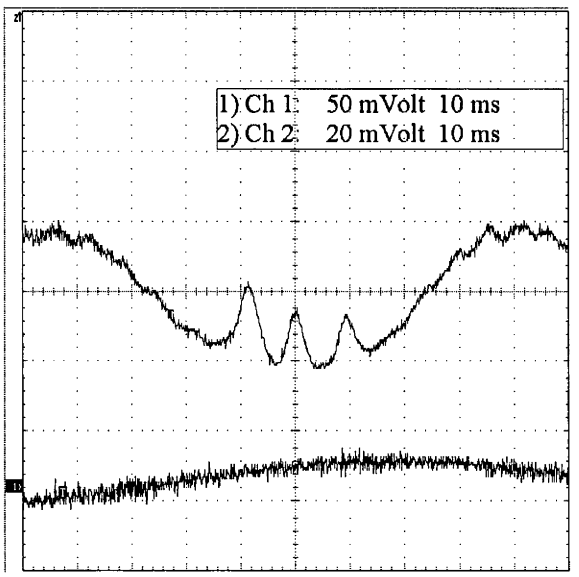

(a) 0.8 Torr

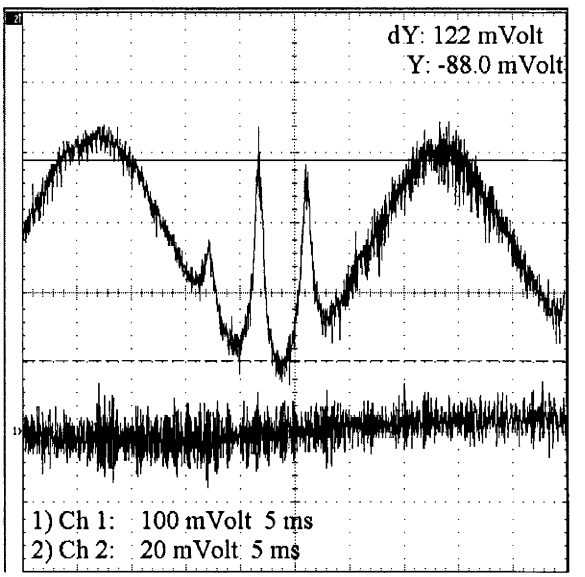

(b) 0.9 Torr

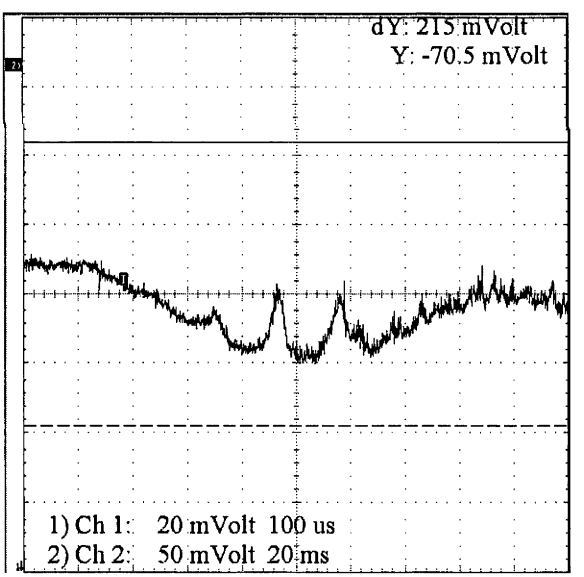

(c) 1 Torr

Figure 6.9: Saturated absorption spectroscopy signals of $j = 1, 2$ and crossover peaks using the full power of the output laser for three different pressures in the DC discharge cell and focusing into the gas cell.

figures. The $j = 1$ becomes larger when circularly polarised light is used because of greater coupling between magnetic substates of the excited and ground state corresponding to a change in magnetic quantum number $\Delta m_j = \pm 1$ as opposed to $\Delta m_j = 0$ for plane polarised light.

The separation between the two substates enables a calibration of the frequency scale and thus yields the linewidth of the Lamb dips which in the case for 0.9 Torr is $\approx$ 60 MHz, which is largely due to saturation broadening of the transition. Obtaining narrower peaks would require using less power. However this would require lower pressures in the gas cell to enable saturation. The gas pressure could not be reduced indefinitely because the DC discharge could not be sustained.

Once sufficiently large enough Lamb dips were obtained a technique to derive the error signal was needed. This requires a dithering either the light or the atomic resonance frequencies so that the phase could be derived by the use of a lock-in amplifier. Initially, an attempt was made to provide the dithering via Zeeman shifting of the transition frequencies analogous to the 1083nm setup. This is realised by the use of a coil placed close to the cell volume to create an alternating magnetic field to provide a Zeeman dither of the electronic transition. It was attempted on both large and small windows of the DC discharge cell with little success.

The Zeeman shift is a result of the interaction of the magnetic moment of the electron $\boldsymbol{\mu}$ and an external field magnetic $\mathbf{B}$ giving an additional term H_B to the Hamiltonian of the electron. This interaction raises or lowers the total energy of the electron, depending on the orientation of $\boldsymbol{\mu}$ in the magnetic field.

$$H_B = -\boldsymbol{\mu} \cdot \mathbf{B} \tag{6.10}$$

For a magnetic field aligned with the z axis interacting with the magnetic substate m_j the corresponding energy shift of the transition E_{m_j} is

$$\Delta E_{m_j} = g_j \mu_B B_z m_j \text{ and where} \tag{6.11}$$
$$g_j = 1 + \frac{J(J+1) + S(S+1) - L(L+1)}{2J(J+1)}$$

The term g_j is the Lande factor of the electronic substate and μ_B is the Bohr magneton. Since the electronic structure of the 2^3P and 3^3P states are identical and there is no dependence in g_j on the primary quantum number n, the Zeeman shifts for each of the magnetic sublevels should be identical for the same magnetic field. The modulating signal was provided using a 20W amplifier operating at a dithering frequency of 5.5 kHz which used identical coils as the 1083nm setup. An estimate using the dimensions of the coil suggest that the setup should be able to produce a $\approx$ 30G field inside the cell volume which induce a sufficient dithering amplitude of around 15 MHz in the transition frequency. Both the polarisation of the laser beam and the electronics were checked. However the dither could not be picked up by the lock in amplifier. A very small and unstable error signal was observed, but it was not possible to lock to the transition. The most likely explanation for the absence of a reliable Zeeman modulated error signal is that due to the much larger intensity noise of the 389nm output. The audio amplifier used to drive the coils could not provide enough modulation depth to be detectable above the noise.

Consequently, the Ti:Sapphire laser frequency was dithered (50mV amplitude at 550Hz) directly through the scan input of the control unit. The effect of the dithering is a modulation of the cavity error signal which translates to a modulation of the lock point and thus the intensity as it scans the cavity resonance, the magnitude of which can be inferred from the cavity error signal. The modulated cavity error signal is shown in the left hand trace of figure 6.10 compared to the unmodulated cavity signal in the right hand trace. From the magnitude of the two signals and the gradient at the center of the cavity error signal (17 MHz/V), one gets a RMS relative frequency deviation of the locked signal with the modulation on of $\approx$ 800kHz in the IR corresponding which yields a peak deviation of about 1.2 MHz with the modulation on. The effect of the dither on the output intensity is to approximately double the intensity noise as is shown in figure 6.11.

The dithering of the centre frequency of the UV output creates a gradient in

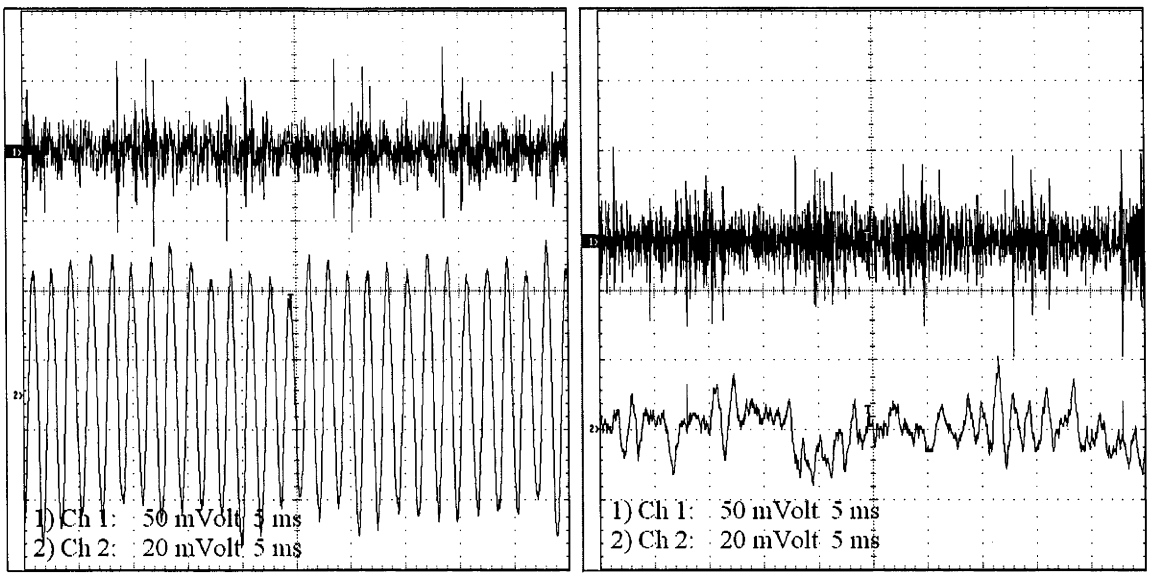

(a) modulation on

(b) modulation off

Figure 6.10: Comparison of locked cavity error signals shown in the top two traces with modulation and off. Bottom traces in both figures show the drive signal from cavity controller.

the absorption signal so that the lock-in amplifier is able lock into to phase of the saturated absorption signals and convert this signal into a suitable error signal to drive another (ANU built) PID controller that controls the Ti:Sapphire laser frequency. The error signals were similar to figure 6.6 and the largest amplitude that was obtained was 1V p-p with a 50mVp-p dithering amplitude. The bandwidth of this control loop is only 800Hz and is limited by the Ti:Sapphire control input. Frequency locking was then easily achieved by manually scanning across the dispersive signals before turning the integrator stage on and adjusting the gains of the proportional and integral stage for the most stable signal. The long term stability was only limited by the drift of the subtracting photodetector that detects the saturated absorption signals which had to be readjusted every 20 minutes or so. The short term stability of the system is estimated approximately to be less than 6 MHz on a

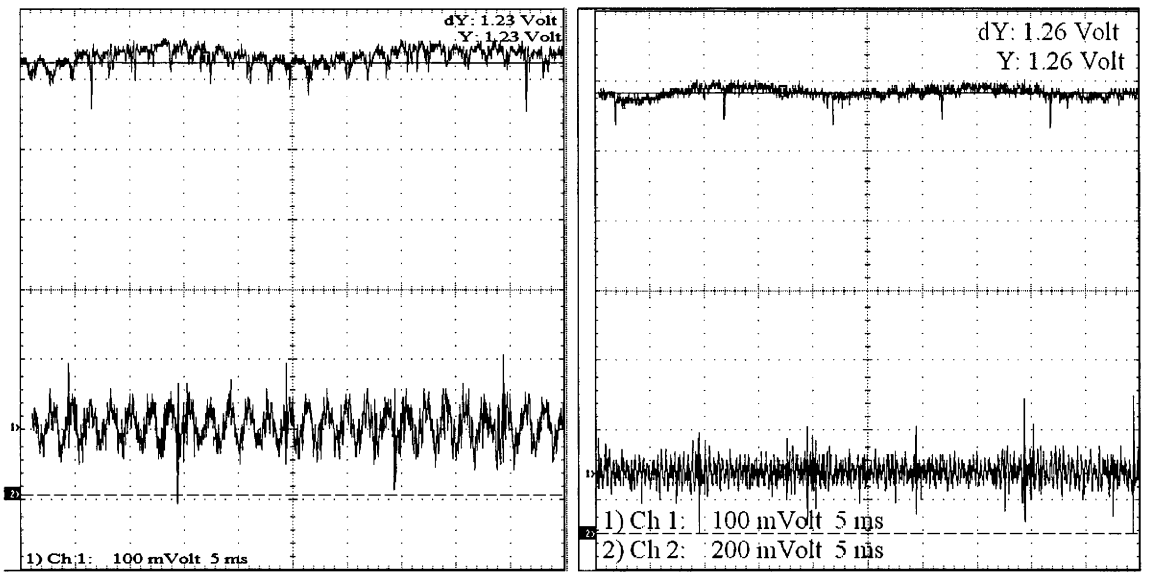

(a) modulation on

(b) modulation off

Figure 6.11: Comparison of the output at 389nm of the doubling cavity with modulation on and off. Bottom traces in both figures show the cavity error signal.

timescale of milliseconds calculated by the gradient of the dispersive signal and the excursion of the residual error signal from the zero crossing.

6.6.1 Conclusion

In conclusion, the $j = 1, 2$ substates of the 3^3P were clearly resolved in the saturated absorption profile and the linewidth observed was $\approx$ 60 MHz (the result of the saturation broadening). Only a small proportion of the generated light was used for locking ($\approx$ 2mW of the maximum 24mW that was obtained). The error signals obtained enabled the system to be succesfully locked to any of the 3^3P substates by dithering the Ti:Sapphire laser, which locked the 389nm light to within 6 MHz of the peak of the Lamb dip for periods longer than an hour.

The system could be improved in several ways. Firstly obtaining still larger

saturated absorption signals by reducing the pressure (however at low enough pressures a discharge could not be sustained) and using less laser power would both narrow the linewidth of the transition and possibly enable tighter locking to the center of the Lamb dip. An anti-reflective coating on the windows of the gas cell would also further increase the absorption in the gas cell. The current method of dithering the Ti:Sapphire laser frequency (and thus the 389nm output) is not ideal because the intensity noise of the 389nm output is increased and the inability to arbitrarily detune the laser frequency once locked, which would be desirable for a variety of experiments. This could be remedied either through obtaining a Zeeman modulated error signal or possibly using a EOM/AOM to modulate the frequency of beam interacting with the atoms in the gas cell. The photodetector that was built to subtract the common mode noise of the Ti:Sapphire could be improved by using more stable amplifiers that have smaller temporal drifts and smaller offset voltages. The use of a 50/50 beamsplitter would increase the common mode rejection of the output intensity fluctuations and improve the signal to noise ratio of the saturated absorption peaks.

CHAPTER 7

Conclusion

In summary, I have developed a practical source of cw laser light at 389nm for use in metastable helium experiments. The system in its current state is ready to be used for a variety of experiments as both an imaging tool and to investigate new phenomena that arise at the 389nm wavelength.

The existing system was characterised in terms of its output power and mode quality, and a procedure for optimum alignment has been developed. The maximum power produced by the system was shown to be consistent with previous work and it is currently limited by the reflectivity of the optics set. The modeling of the laser cavity enabled a close to optimum mode-match to the Ti:Sapphire source. The output has also been collimated and corrected for the inherent ellipticity which resulted from the walk-off inside the non-linear crystal.

Crucial to the experiments performed was the ability to successfully lock the Ti:Sapphire output frequency to one of the resonant cavity modes to enable stable cw operation. I have shown through the implementation of an active feedback stabilisation system that the output laser intensity has been locked to better than 10% of the peak cavity transmission. This corresponds to a relative frequency offset of less than 500 kHz on millisecond timescales. The cavity stays locked at the same level for periods of several hours and was found to be limited by mode-hopping of the pump. A model of the feedback system has been developed which shows

some agreement with the experiment and could be used to improve the locking performance in the future. The current limit on the bandwidth of the feedback system is the resonant behaviour of the PZT mirror which was characterised in terms of its bandwidth and resonant frequency.

Saturation absorption spectroscopy in a DC helium discharge cell was performed and the substates of the 3^3P transition were resolved, which previously had not been possible with this system in this laboratory. Close to optimum conditions in the discharge cell were determined for obtaining large saturated absorption signals. Due to the smaller absorption cross-section for the transition at 389nm and larger intensity noise of the laser output, the method for obtaining the saturated absorption signal is based on the subtracting the common-mode noise of the signal. The width of the Lamb dips that were obtained is 60 MHz as a result of saturation broadening. Error signals were obtained by dithering the frequency of the Ti:Sapphire laser and using lock-in detection of the saturated absorption signal. The output of the 389nm light was subsequently locked to the $j = 2$ substate using feedback control of the Ti:Sapphire laser frequency.

7.1 Further Work

The utility of the current system could be greatly enhanced by taking care of several outstanding issues.

The current optic set limits the output UV power to around 25mW at the maximum output of the Ti:Sapphire (currently 1W at 778nm). Increasing the reflectivity of the mirrors would make this in excess of 100mW accessible with minimal effort. It has been reported that an efficiency of approaching 50% is achievable [8]. This would enable the system to be used as both a cooling/trapping laser and as a laser for altering the dynamics inside the current metastable helium MOT operating at 1083nm.

Improvements to the frequency locking system would decrease the intensity noise on the output. This would increase signal to noise ratio in any application experiment. By development of the model of the control system set out in this thesis, the locking bandwidth could be improved. The bandwidth could be further enhanced by obtaining a piezo of greater bandwidth and subsequent modification of the existing controller. Enhanced frequency stabilization of the Ti:Sapphire throught the use of an EOM/AOM would also decrease the output intensity fluctuations.

The locking to the resonant transition could be improved by obtaining larger saturated signals with less power and narrow the currently power broadened Lamb dips. Observation of the Zeeman shift in the cell would enable locking to the transitions without adding intensity noise to the output and also would enable the frequency to be detuned arbitrarily from resonance, which is currently not possible. Alternatively dithering without adding noise to the output of 389nm as well as detuning from the atomic transition could be achieved using an AOM or EOM. Improvement in the photodetector built to detect the error signals would also increase locking intervals.

Finally the use of the system in an application experiment would enable the investigation of several open questions regarding the behaviour of metastable helium in this highly excited state. Possible experiments include the study of the production of cold long-range dimers via photoassociation spectroscopy whose internuclear separation would be even greater than those observed at 1083nm. The cold collision dynamics at this transition are not well understood and warrant further investigation. Higher momentum transfer makes the system applicable for collimation stages for brightening of atomic beam apparatus and as a more efficient optical molasses stage for the compression of the atomic cloud. Furthermore, as an imaging tool it would be highly useful since the quantum efficiency of CCD cameras are much greater at this wavelength.

Bibliography

[1] Harold J. Metcalf and Peter van der Straten *Laser Cooling and Trapping,* Springer-Verlag, 1999

[2] W. Vassen, C.R. Acad. Sci. Paris., *2*, Series 4, 613-618, 2001

[3] M. Jacka, M. D. Hoogerland, W. Lu, D. Milic, K.G.H. Baldwin, K.Bartschat, and S.J. Buckman J. Phys. B. *29*, L825-830(1996)

[4] F. Pereira Dos Santos, J. Leonard, Junmin Wang, C.J. Barrelet, F.Perales, E. Rasel, C.S. Unnikrishnan, M. Leduc, and C. Cohen-Tannoudji, Phys. Rev. Let. *86* vol 16, 3459(2001).

[5] A. Robert, O. Sirjean, A. Browayes, J. Poupard, S. Nowak, D. Boiron, C.I. Westbrook, A. Aspect, Science *292*, 461, 20 April 2001.

[6] N. Herschbach, P.J.J. Tol, W. Vassen, W. Hogervost, G. Woestenek, J.W. Thomsen, P. van der Straten, A. Niehaus, Physical Review Letters *84* No 9, 1874, 28 February 2000.

[7] Paul J.J. Tol, N. Herschbach, E.A. Hessels, W. Hogervost, and W. Wassen, Phys. Rev. A. *60* vol 2, R761(1999).

[8] J.C.J. Koelemeij, R.J.W. Stas, W. Hogervost, and W. Vassen, Phys. Rev A., *67*, 053406-1, 2003

[9] R. Schumman, C. Schubert, U. Eichmann, R. Jung, and G. von Oppen, Phys. Rev. A. *59* vol 1, 2120(1999).

[10] Paul J.Hack, L. Liu, M. Olshanii, and H. Metcalf, Phys. Rev. A. *62*, 013405(2000).

[11] J. Leonard, M. Walhou, A.P. Mosk, T. Muller, M. Leduc, and C. Cohen-Tannoudji, Physical Review Letters *91* No 7, 073203-1, 15 August 2003.

[12] Robert G. Dall, Electron collisions with cold metastable helium, PhD Thesis, to be submitted ANU 2004

[13] Linda Uhlmann, Electron collisions with cold metastable helium, PhD Thesis, to be submitted ANU 2004

[14] T. Hanna, J. Nes, R.G. Dall, A. Truscott and K.G.H. Baldwin, ANU 2004, to be submitted.

[15] R.W.Boyd, *Nonlinear Optics,* Academic Press, 1992

[16] P.A. Franken, A.E. Hill, C.W. Pteres, G. Weinreich, Phys. Rev. Lett. *7*, 118, 1961

[17] H.Kogelnik, T. Li, Applied Optics, *5*, No 10, 1550 (1966)

[18] G.D. Boyd, D.A. Kleinman, J. Appl. Phys. *39* 1968 (3597)

[19] E.Hecht, *Optics*, Third Edition, Addison-Wesley, 1998

[20] W.J. Kozlovsky, C.D. Nabors, R.L. Byer, IEEE Journal of Quantum Electronics *24* No 6, 913, 1998

[21] E.S. Polzik , J.D. Kimble, R.L. Byer, Optics Letters *16* No 18, 1400, 1991

[22] E. Jurdik, J. Hohlfield, E. A. van Etteger, A. J. Toonen, W.L. Meerts, H. van Kempen, Th. Rasing, J. Opt. Soc. Am. B Vol. *19*, No. 7, page 1660, 2002

[23] S. Bourziex, M.D. Plimmer, F. Nez, L. Julien, F. Biraben, Optics Communications *99*, 89-94, 1993

[24] T. Kaing, M. Houssin, Optics Communications *157*, 155-160, 1998

[25] C. S. Adams, A. I. Ferguson, Optics Communications *90*,89-94, 1992

[26] C.Q. Wang, L. Reekie, Y.T.Chow, W.A. Gambling, Optics Communications *157*, 155-160, 1998

[27] Dragana Milic. PhD Thesis, ANU 1999

[28] James Swansson, Generating blue 389nm light, May 2000 internal report, ANU

[29] Stefan Voll, Masters Thesis, Stony Brook, SUNY 1995

[30] W.W. Rigrod, The Bell System Technological Journal, 907, 1965

[31] Casix website crystals page,http://www.u-oplaz.com/crystals/

[32] Xinping Zhang, PhD Thesis,PU Marburg 2002

[33] C.Harb, Stabilization of a Ring Dye Laser, Masters Thesis, ANU 1992

[34] Coherent 899-21 Ring laser operator's manual, Coherent Laser Group

[35] R.L. Barger, M.S. Sorem, J.L. Hall, Frequency stabilisation of a cw dye laser, Applied Physics Letters *22*, 573, 1973

[36] A.D. White, Frequency stabilisation of Gas Lasers,IEEE Journal of Quantum Electronics QE-1, 349, 1965

[37] T. Hansch, B. Couillaud, Optics Communications *35* 3, 441, 1980

[38] N.Storey, *Electronics a Systems Approach*, Second Edition, Addison-Wesley, 1995

[39] OP7 & OP27 Data sheets, Analog Devices Homepage, http://www.analog.com/

[40] N.S.Nise, *Control Systems Engineering*, The Benjamin/Cummings Publishing Company, 1992

[41] R.Heck, Feedback Stabilized Laser Cavities, Masters Thesis, ANU 2000

[42] B.J.Lurie, P.J. Enright, *Classical Feedback Control*, Marcel Decker Inc, 2000

[43] W.Demtroder, *Laser Spectroscopy - Basic Concepts and Instrumentation*, Second Corrected Edition, Springer-Verlag, 1982

[44] W.Lu, D. Milic, M.D. Hoogerland, M.Jacka., K.G.H. Baldwin, S.J. Buckman, A practical direct current discharge helium absorption cell for laser freuqency locking at 1083nm, Rev. Sci. Instrument *67*, 9, 1996

[45] O. Svelto, *Principles of Lasers*, Third Edition, Plenum Press, 1989

[46] NIST Physics Laboratory homepage,http://physics.nist.gov/

[47] B.H.Bransden & C.J. Joachain, *Physics of Atoms and Molecules*, First Edition, Addison-Wesley Longman, 1998

[48] A.S. Tychkov, J.C.J. Koelemeij, T. Jeltes, W. Hogervost and W. Vassen, Twocolo magneto-optical trap for metastable helium, Laser Centre Vrije University, Feb 24 2004, to be submitted

[49] J.C.J Koelemeij, Perfomance check and reccomendations concerning second-harmonic generation at the ANU (July 2003), Private communication

[50] M. Brieger, H. Busener, A. Hese, F.v. Moyers, A. Renn, Optics Communications *38* No 5,6 , 423, 1981

[51] B. Smeets, R.C.M. Bosch, P. van der Straten, E. te Sligte, R. E. Scholten, H.C.W. Bejerink, K. A. H. van Leeuwen, Applied Physics B, (submitted) 2003

APPENDIX A

Appendix A - Cavity Alignment

This is a difficult procedure at first, so it is described in some detail. Presented here is the final procedure that gave the highest power. The nomenclature of the cavity optics is that used in figure A.1. To perform this procedure the following vital pieces of equipment are needed:

- White business card - to observe the IR beam spot which is a deep red colour.
- IR viewer - to observe the beam spots on the optics of the cavity where the intensities are much smaller.
- photodetector - to measure the cavity throughput once the beams are roughly aligned and some IR power is transmitted through the output coupler. This must be used in conjunction with an attenuator to keep it in the linear range. The detector uses a photodiode in reverse bias mode and is powered by $\pm$ 15V supply. Otherwise the signal saturates at much lower powers and the response time is slower.
- CRO - to display the signal at the photodetector and optimise the cavity by observing the fringes as the cavity is scanned through the resonances.
- mode matching lenses - the output mode of the Ti:Sapphire is different to the lowest order cavity mode and they need to be matched. While it is possible to mode match with one spherical lens, the optimal combination was found to be a telescope consisting of one f=200mm and one f=175mm plano convex lens.

• alignment pinhole (variable aperture) - mounted on a shortened post to align the height of the laser beam inside the cavity to a height roughly equal to the center of the crystal.

The Ti:Sapphire is operated at moderate power about (600mW on the Spectra

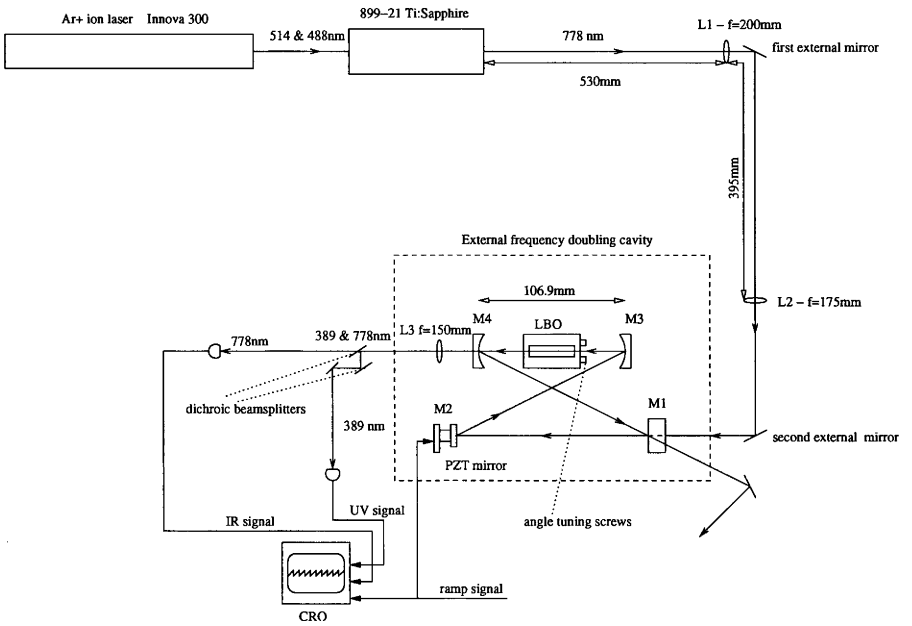

Figure A.1: Experimental setup for alignment of the external doubling cavity. Refer to the text for details

Physics 404 power meter) and with the scan mode set to internal and lock. The cavity length is scanned using the Burleigh RC-42 ramp generator as the source. The ramp is used to trigger the CRO, and the ramp period is on the fastest setting (20ms) so that slower fluctuations in the cavity length are less visible. The aligmnent is then faster because of the more instantaneous response to mirror adjustment.

The first goal is to couple the laser beam into the cavity, roughly centered on all the cavity optics. This is achieved by steering the first two external mirrors in the beam path. The procedure is to:

(1) Steer the beam so that it goes through the larger hole in the perspex housing. Now the card is placed inside cavity and the path it follows towards the PZT

mounted mirror is traced. Using the first external mirror the beam is steered so that the spot is roughly in the center of input coupler M1 in both horizontal and vertical directions. Now the beam path is followed towards the piezo mirror, and the mirror closest to the cavity is steered so that the beam spot follows a path that is roughly parallel to the sides of the box and hitting at center the center of the PZT mirror. It was found that the proper height was not exactly in the center of the piezo but slightly closer to the lower edge. The beam spot at the piezo mirror at this stage slightly less than half the size of the piezo mirror in height, and slightly larger in width.

(2) Introduce the mode matching lenses. The f=200mm lens is placed closest to the Ti:Sapphire laser 576mm from the output face of the laser and just before the first external mirror. A white card is taped on the input hole of the cavity and the lens placed centrally on the laser axis, resulting in minimal deflection of the beam spot on the card compared to when the lens wasn't there. Ensure the curved side of the lens is facing the the laser to reduce spherical abberation.

(3) The height of the crystal above the granite block should now be measured using calipers(without touching the crystal face or optics). This is used then to set the height of the mounted pinhole. With the pinhole almost totally closed the beam should be now small enough to pass through it. The pinhole is placed immediately after the input coupler and the first external mirror adjusted to steer the beam through the pinhole. Then the pihole is then placed before the PZT, and the second external mirror (i.e. the one closest to the cavity) is adjusted so the beam passes through the pinhole. The pinhole is now used to set the height adjustment of the cavity mirrors. It is only possible to do this for the beam path from the PZT mirror M2 to the first focusing mirror M3, but this is adequate. The mounted crystal itself gives enough spatial reference to steer the beam onto the output coupler M4.

(4) With the vertical adjustment on the PZT mirror M2 the beam is steered so the spot is at the center of the first focusing mirror in the horizontal direction, and is

set using the pinhole the vertical direction.

(5) Using the infrared viewer it is possible to finely adjust the position of the beam spot on the first focusing mirror M3 using the piezo mirror M2. The first focusing mirror is now adjusted to steer the beam through the crystal and onto the center of the output coupler mirror M4.

(6) The beam should then enter the crystal almost perpendicular to the crystal face. Using the infra red viewer the beam should be steered through the center of the crystal so that it exits the crystal roughly at the same position on the face as it entered. Now the crystal's long dimension is parallel to the beam, and the beam height following the crystal is not being deflected. This takes some iterations and the angle adjustment on the crystal stage also is used to rotate the crystal about the tangential plane of the cavity (the top two screws on New Focus mount). Using lateral the translation (single screw on the right hand side), the beam is placed correctly to ensure that it enters and exits the crystal at the same place position on the crystal face, and strikes the output coupler mirror M4 at the center.

(7) The cavity dimensions - in particular the distance between the two focusing mirrors are set close to those given in Section 3 r i.e. $a = 106.9mm$ for the distance between the two curved mirrors. The cavity is most sensitive to the separation of these two mirrors so this must be set precisely. The mirror separation varies the size of the cavity mode and thus modematching, so this determines how much light enters the cavity on resonance and thus determines the peak height. With these mirrors set accurately, an initial overlap can be performed which is sufficient to observe fringes on the photodide.

(8) The mirror M4 completes the ring cavity by steering the beam back on to the input coupler to the position where it entered the cavity. The overlap between these when viewed with the infra-red viewer is crucial. Using the controls of the M4 mirror, beam placement onto the input coupler is found using the infra-red viewer, and the beam walked till it is obvious which spot is the reflection. The spots on the

input coupler should be clean and round and the surface of the optic fairly clean under the viewer. If the input coupler appears dirty or shiny there is too much scatter from dust, it should be cleaned well with ethanol and lens tissues. At most there should be two small satellite spots visible slightly displaced from the central maximum and which are probably due to diffraction from the Ti:Sapphire output coupler.

(9) By walking the beam with the mirror M4 it is possible to overlap the reflected spot with the input beam. To make sure the vertical position is correct, the beam is dithered horizontally, and vice versa for the other dimension. If the dimensions of the cavity are close to correct (step 7), two spots will be about the same size. If not then a rough overlap is made.

(10) By walking the input coupler M1 a bright spot should be visible in the vicinity of the PZT mounted mirror M2, this is the beam after it has completed one cavity round trip. The single cavity round trip spot is then moved with the input coupler M1 slightly to the side so that, with the white card and the IR viewer, the relative size of the input spot on the piezo and the beam size after one cavity trip can be compared, and should be roughly the same size and shape. If the two spots can not be distinguished in size the cavity is ready to be overlapped. If the beam sizes are obviously different, then distance of M4 the output coupler should be adjusted by turning all three controls the same amount in the same direction and observing how the beam size changes. Step 7 should have also remedied this part.

(11) Overlapping the cavity is achieved by walking the reflected spot using the input coupler M1 onto the input spot on the piezo. When the cavity is close to being overlapped a familiar axial mode pattern will appear, the higher order Hermite-Gaussian TEM_{nm} of the resonator. Most likely it will be the TEM_{0m} or TEM_{n0}; they appear as a series of spots side by side or on top of each other. Their number will increase and eventually disappear as M1 is adjusted or will decrease, and collapse onto one bright spot. This is then the main TEM_{00} Gaussian mode which is

the least divergent mode with the lowest loss in the resonator. In the TEM_{00} mode the spots on the cavity mirrors should now appear much brighter and should flicker in time with the scan frequency. With the white card it should be now possible to see a dull red beam outside the cavity after the output coupler M4 or even a blue 389nm beam which is elliptical and overlapped with the fainter red beam.

(12) A second lens is placed after the output coupler M4 to provide a degree of collimation of the output beam so that higher spatial modes can be detected by the photodiode. An f=150mm focal length lens that is AR coated for 389nm is placed one focal length away from the center of the crystal to collimate the 389 nm beam onto the photodiode to allow fine tuning to be performed. The linearity of the photodiode should be checked so that it is not being saturated, by placing filters of known transmission and observing that the signal reduction is linear with the filter's attenuation. If the Newport power meter is used the proprietary OD3 filter should be used and the correct mode selected on the display.

(13) The cavity length is now scanned using the piezo and the photodiode produces a series of narrow spikes representing the transmitted cavity modes. The optimisation now involves tweaking the cavity mirrors to maximise the power in the lowest order mode. Because the different cavity modes have differing Guoy phases they have different resonant frequencies, appearing in the signal as different time intervals between adjacent maxima. These are shown in figures A.2, A.3

(14) Maximising the power in the lowest order cavity mode involves the adjustment of three of the cavity mirrors which control the overlap inside the cavity, and careful adjustment of the external mirrors which control the incoupling. At this point if the cavity is producing blue light visible on the card, the optimisation should be switched to the blue signal because increasing the peaks in the red signal does not necessarily increase the conversion into the second harmonic due to depletion of the fundamental. The two dichroic beam splitters should be used when monitoring the blue output to ensure almost no fundamental radiation reaches the photodetector.

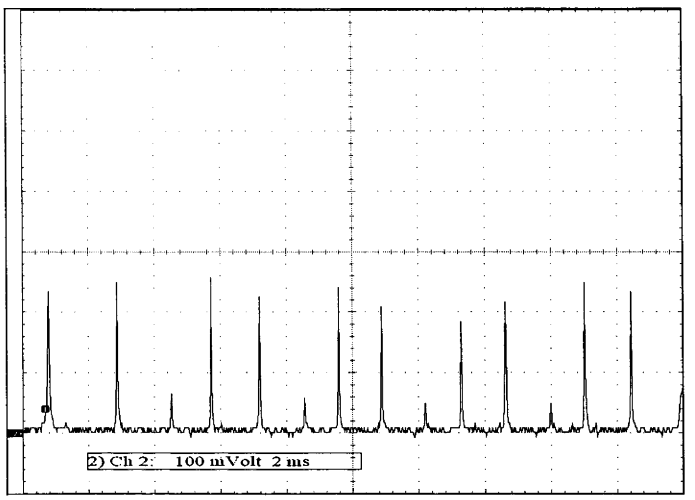

Figure A.2: The tranmission of the 778nm fundamental through the external doubling cavity when the length of the cavity is being scanned showing sharp transmission resonances measured with Newport power meter. This figure shows the next higher order spatial mode TEM_{01}, verified by observing the beam shape on a white card.

(15) If the cavity is not producing blue light that is visible on the card the phase matching angle needs to be adjusted. This is done by rotating the top two screws on the crystal stage. The crystal should be rotated to the position where the maximum amount of blue light is visible on the white card. Because of the change in refractive index between the crystal and the air, rotating the crystal deflects the beam slightly degrading the overlap. Thus this should be compensated by adjusting the M4 output coupler and M1 input coupler in that order, to overlap the beam first on the input coupler and then back on the piezo. When this occurs the intensity of the blue light should increase on the card so that the red can not be seen. If the overlap causes the blue to disappear then the crystal needs to be rotated in the opposite direction and the overlap repeated. The phasematching directly controls the interaction length via the phase mismatch parameter Δk to which the conversion has a sinc squared dependence given in equation 2.8. Thus it is desirable to

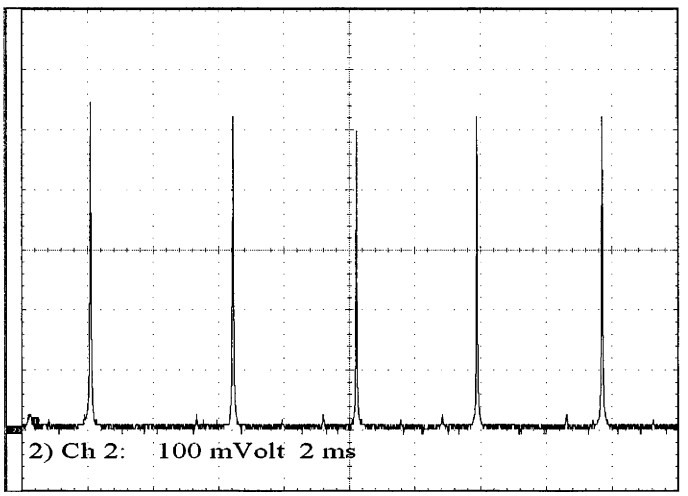

Figure A.3: As for figure A.2, but this is showing the lowest order Gaussian TEM_{00} mode. The peaks are much higher in comparison with the previous figure and the spacing between adjacent maxima is larger. A residual higher order mode is somewhat visible. The peak-to-peak transmitted power is 62mW. The horizontal and vertical scales in both figures are the same.

be in the central lobe of that curve. The crystal has been cut in such a way that if the beam enters the crystal perpendicular to the endfaces, the input beam is at the proper phasematching angle to the crystal axis. Thus it should be not be too difficult to obtain visible blue light.

(16) Alternatively the input coupler optic can be removed, and by steering the 778nm beam into the crystal via mirrors M2 and M3 while adjusting the crystal angle, blue should become visible. During this process the fundamental spot on the M4 output coupler should be maintained in the middle of the optic and at the correct height. The input coupler is then replaced and the cavity overlapped. When the cavity is overlapped again the blue spot will be seen displaced from the center of the red spot this due to the extra optical path introduced by the input coupler. This can be remedied using the next step in the procedure. Care must be used with this procedure since all the laser power enters the cavity at all times i.e. the

intracavity power is high!

(17) The fine tuning procedure which follows aims to maximise the power in the blue by adjustment of the separation between the two focusing mirrors, the parameter to which the output power is most sensitive. This is performed while monitoring the peak height of the blue light with the photodiode. By turning the three controls on the optics mounts the same amount in the same direction, translation is performed while the attitude of the mirror to the beam is maintained. The optic used to perform the translation is the output coupler M4; there is no need to move the first focusing mirror M3 at all. The M4 optic also controls the overlap on the input coupler M1. So the procedure is always to translate the M4 optic, and the signal on the photodiode is made to disappear and reappear when all three have been turned the same amount. The overlap should still be significant and thus the signal would not disappear completely. Then the input coupler M1 tilt controls should be adjusted to obtain the maximum blue output peak height. This should be performed iteratively, always maintaining the order of the adjustment i.e. adjust M4 then M1. The peak height should monitored at all time. If after several iterations the peak height decreases the process should be reversed i.e. the M4 optic translated in the opposite direction. One whole turn of the controls translates the mirror by 1mm. Slight gains can also be made by translating the position of the second external lens back and forth with the longitudinal control of the lens holder, which has the effect of varying the size of the focus at the center of the crystal. Slight adjustment of crystal angle on the mount might also produce gains, but it also causes misalignment of the ring cavity, so this must be compensated once again with the M4 and M1 optics.

This finalised alignment procedure enabled quick realignments when necessary, and yielded the highest conversion efficiency observed during experiments. Obtaining the positions of the modematching lenses (as well as whether to use one or two lenses) required modeling of the beam parameter in the cavity as well the propaga-

tion of the mode of the Ti:Sapphire. This was done by implementing ray transfer matrices in Mathematica.

APPENDIX B

Appendix B - Practical guide to locking the 389nm cavity

In this section the practical aspects of locking the external doubling cavity to the Ti:Sapphire output are described. This was performed on a daily basis during all aspects of the experimental work.

A good lock of the cavity requires three basic elements:

1.- Symmetrical cavity locking signal with sharp as possible dispersion shapes with low noise and little extraneous structure due to higher spatial modes (shown in section 5.3) and an peak-to-peak amplitude of around 220mV ;

2. - The gains of the controller to be roughly in the correct positions defined by table B.1;

3. - The internal lock of the Ti:Sapphire to be functioning correctly without excessive noise and fast intermittent jumps in frequency.

The first requirement is met by following the procedure in Appendix A. This should give error signals when the cavity is scanned similar to Figure 5.10. This is done by adjusting the TOTAL GAIN control so that the signals are about 220 mVp-p. It should be noted that the magnitude of the dispersion signals will vary with the incident power of the Ti:Sapphire but it was found that for a stable lock their magnitude should be kept at around 220mV p-p at the MONITOR output which

is probably an effect of the slew rate of the amplifiers.

With good clean dispersion signals on screen the SCAN/LOCK switch on the side of the controller should be set to LOCK. At this point either the cavity will lock or there will be little or no signal present at the MONITOR output meaning the cavity is somewhere far from one of the resonances. The potentiometers on the cavity controller that set the gain of each of the control stages have dials with numbers on them which range from 0-100. The should be set to the numbers shown in table B.1 With these controls set, the INPUT OFFSET control is adjusted until a

Gain Control	PF	I	P	TOTAL GAIN
Value	99	85	50	30-90

Table B.1: Typical gain parameters parameters for locking 389nm cavity set by the heliostats on the front panel of controller.

fast oscillation on a 5ms time scale is observed that resembles the left hand trace of figure B.1 At this point the cavity is partially locked and is oscillating with the full

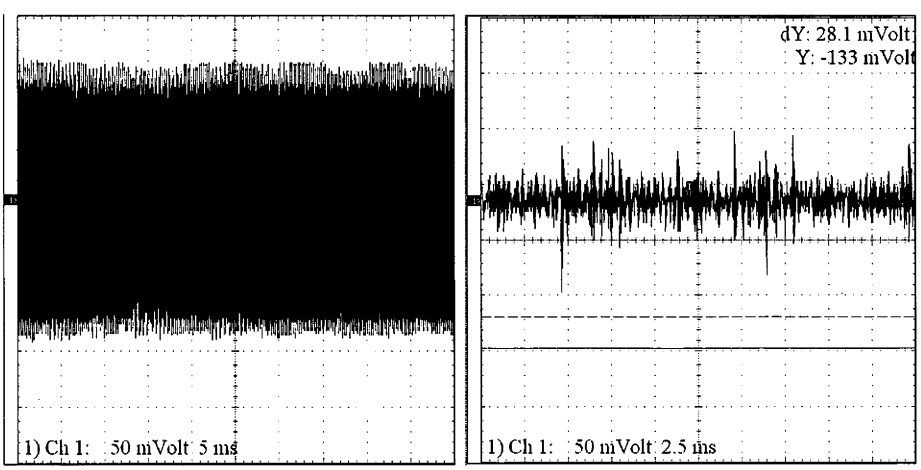

(a) partial lock (b) fully locked

Figure B.1: Time series of error signal at MONITOR output of controller showing a partial lock and full lock of the cavity.

amplitude of the error signal. The trace is around zero if the INT RESET switch had been set to ON previously. If the switch is in the OFF position then the signal will be offset from zero. flipping the switch will move the trace around zero but it also might cause the cavity to lose lock if the gains are too high. If the trace is around zero then the integral stage will maintain the position and counteract any drifts. At this point however the control loop is very sensitive to external factors and is not providing any attenuation of the error signal. To obtain the full locked state shown in the right hand trace of figure B.1 the proportional stage is adjusted either up or down. When the gain is turned up and the cavity locks up, it happens suddenly. If the gain is adjusted down and the left hand trace becomes smaller, it occurs gradually. The proportional stage can be turned down until the trace is around 10% of the original amplitude. Turning it down further will send the cavity into oscillation due to not enough phase correction at higher frequencies, as is shown in figure B.2 This behaviour is explained through the series of Nyquist diagrams

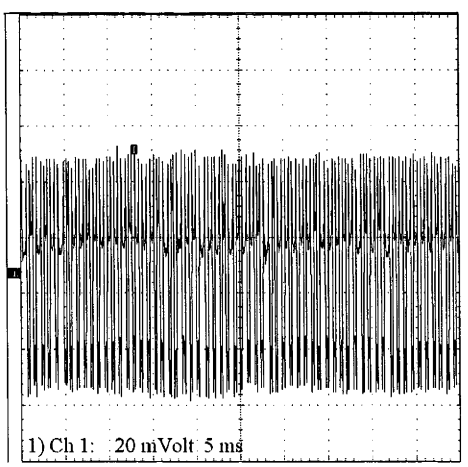

Figure B.2: Error signal showing oscillation of control loop due to inadequate proportional gain.

in figure 5.22. At this point the cavity is fully locked and will maintain its state for long periods of time (many hours) and is fairly robust to low to mid frequency

vibrations: small taps and bumps of the table will not disturb it. The intensity of the laser output should be monitored with a suitable photodetector to observe the intensity noise. Small but significant improvements can than be made by a slight adjustment to the INPUT OFFSET control. This sets the cavity lock point and it was found that the intensity noise is smaller when the lock point is slightly offset from zero, which is probably due to the cavity locking slightly to the side of the cavity fringe than the center. While the magnitude of the error signal does not change greatly the intensity noise does reduce appreciably.

If the cavity becomes unlocked it may drift into lock on its own, otherwise the INPUT OFFSET is readjusted to obtain the traces previously discussed. If the cavity does not lock well the SCAN/LOCK switch should be set back to SCAN and the symmetry of the dispersion signals should be readjusted by the rotation of the $\lambda/4$ plate in the locking setup.

If the frequency of the Ti:Sapphire is being scanned as is needed to obtain the saturation spectroscopy signals discussed in chapter 6, some adjustment of the P gain will be needed since it will be observed that the amplitude of the error signal will vary in phase with the frequency scan. The P gain is adjusted until the amplitude of the error signal is again roughly the same as before (around 10% of the dispersion signal amplitude) while the zero point of the trace moves in phase with the modulation. If this is not possible to achieve then the integral gain I should be reduced this is the case. It was found that this was not required if the scan range on the Ti:Sapphire was less than 1 GHz for a scan frequency of less than 4 Hz. This is simply a result of the integral stage counteracting the scan.

An intermittent problem was found with optical feedback from the doubling cavity back into the internal Ti:Sapphire frequency locking system. This could not be fully explained since a ring cavity of the bowtie configuration such as one in our system should not reflect any power back towards the laser. However this was observed from time to time which makes locking for timescales longer than a few

seconds impossible. The symptoms of this problem are large spikes in the intensity of the laser and the error signal which are also present at the VERT output of the Ti:Sapphire control box. This was confirmed to be optical feedback shown by the following two traces shown in figure B.3. The lower traces marked 1 show the

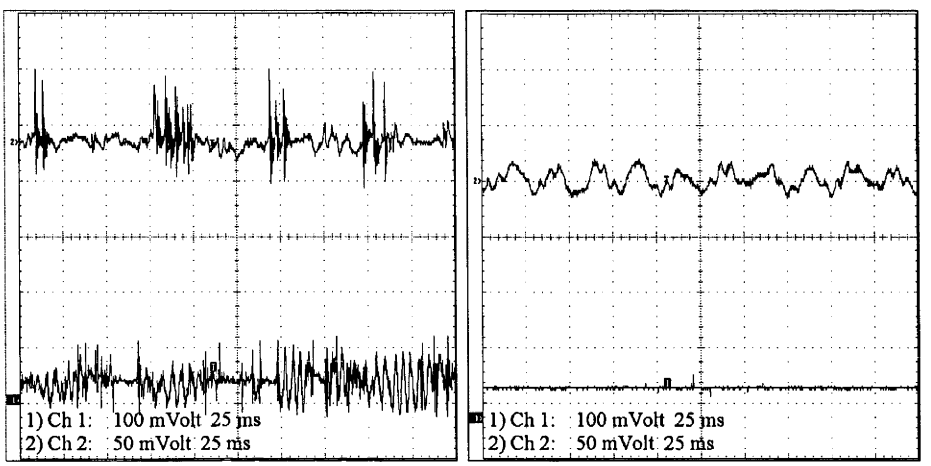

(a) cavity unblocked (b) cavity blocked

Figure B.3: Time series of the cavity error signal and the intensity noise of the Ti:Sapphire output. Top traces show the intensity noise of the Ti:Sapphire laser recorded with Spectra Physics 404 power meter. Bottom traces are the residual error signals with the cavity locked.

intensity noise,and are taken by splitting off some power from the Ti:Sapphire with a beam splitter before the cavity and measuring it with the Spectra Physics 404 power meter that has been AC coupled. Trace 1 in both pictures is the residual error signal when the cavity is locked. The left hand figure shows when the path to the cavity is unblocked, with the intermittent peaking in the output of the Ti:Sapphire correlated to large transients in the error signal. The right hand picture shows when the path to the cavity is blocked, and these transient peaks are not seen. Electrical interference was ruled out by the fact that the voltages that occur at the high voltage amplifier are when the cavity is locked are around 200mVp-p and changing

the power points did not alleviate the problem. The solution was found was to slightly rotate the crystal around the phase matching direction with a subsequent realignment of the cavity for peak power. However the exact position of the crystal that caused the problem was not clear.

APPENDIX C

Appendix C - Electronic Circuitry

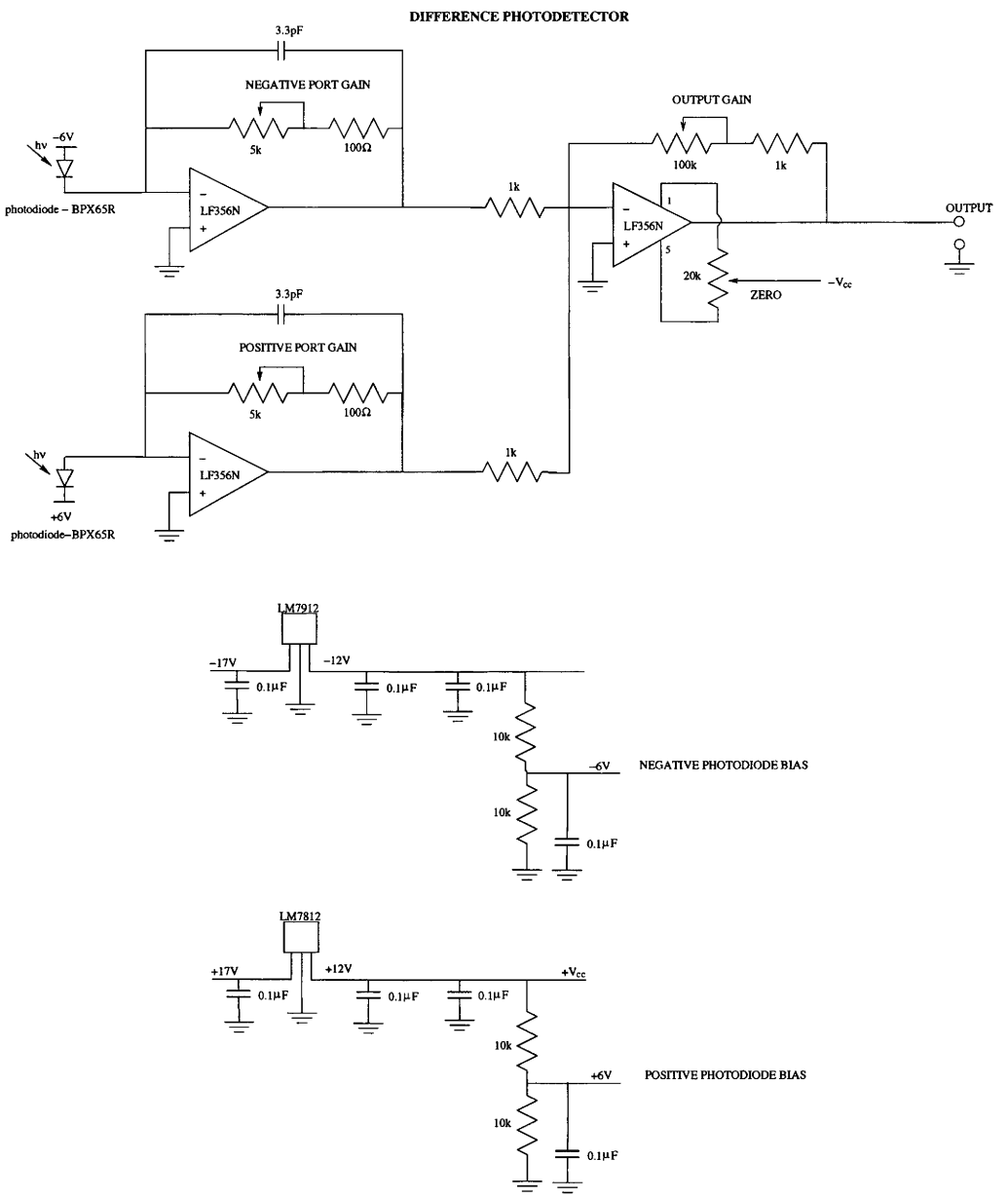

Figure C.1: Circuit diagram of homebuilt photodetector for detection of saturated absorption signal in chapter 6. Output produces voltage proportional to difference of photocurrent in each port

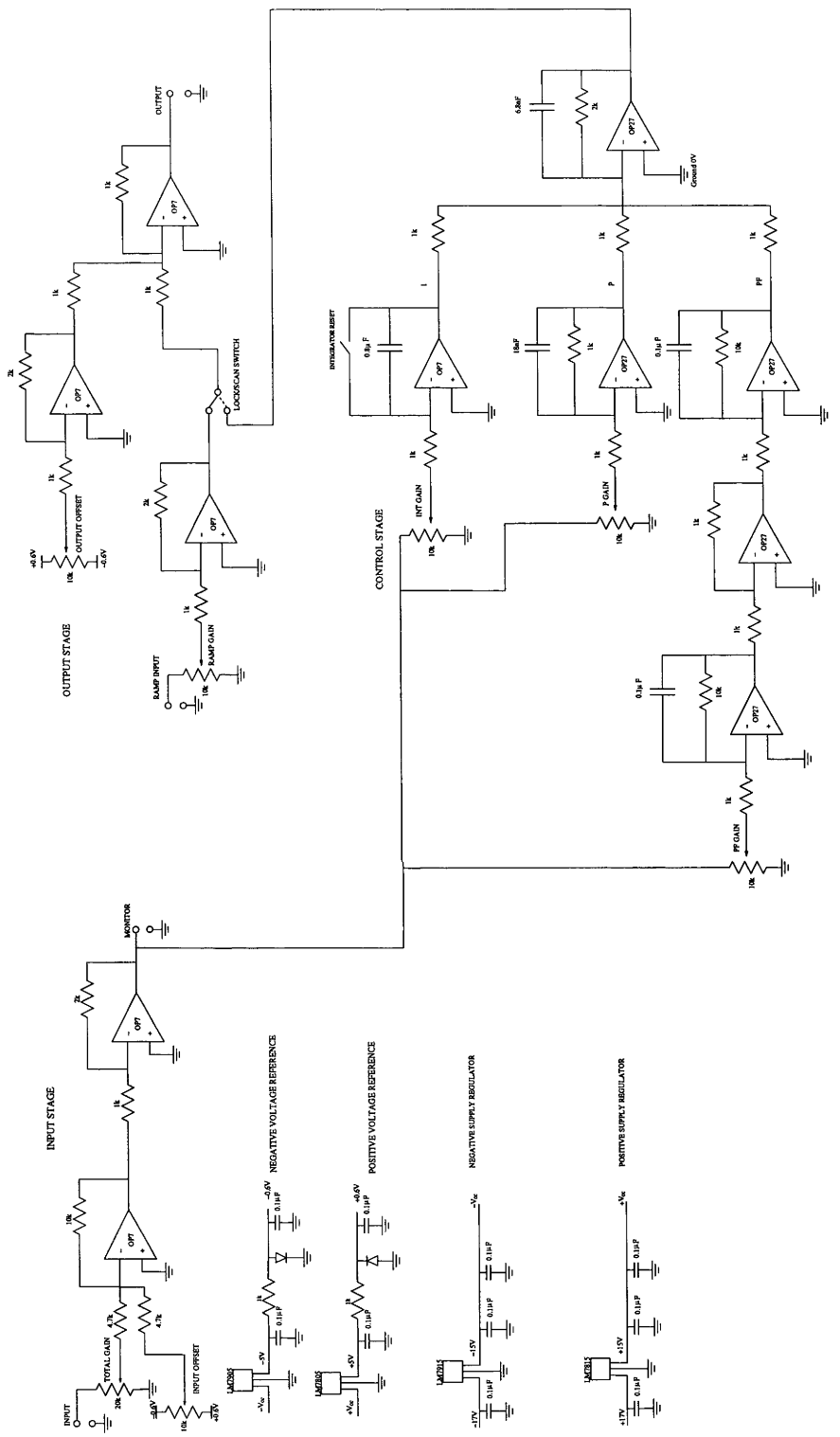

Figure C.2: Complete circuit diagram of 389nm feedback cavity controller described in detail in chapter 5.

Appendix D - Mathematica Printouts

```
(* Mathematica script to calculate laser waist inside cavity
  between plane mirrors using transfer matrix method by Kogelnik and
  Li by varying the mode matching lens to laser seperation we want
  to obtain the optimum waist inside the cavity  of 311 microns *)
(* Single Lens f=500 mm *)

λ = 0.000778
w0 = 0.324 (* Ti:Sapph waist and corresponding q1 beam parameter *)
q1 = I ((Pi * w0 ^ 2) / λ)
theta = 0.113
```

0.000778

0.324

423.897 i

0.113

```
T = 1186
```

1186

```
(* Total distance to cavity T=d1val+d2val,
 d1val=mode matching lens to laser waist,
 d2val=modematch lens to input coupler use d1val as parameter *)

d1val = 650
(* original position was 711 but that gave
  that beam was focusing on the piezo which by lookin at the
  cavity seemed to be correct so it has to be moved 84 mm *)
f1val = 500
d2val = T - d1val
x = g
```

$$\text{Mat} = \begin{pmatrix} 1 & d \\ 0 & 1 \end{pmatrix} \cdot \begin{pmatrix} 1 & k \\ 0 & 1 \end{pmatrix} \cdot \begin{pmatrix} 1 & 0 \\ -1/f1 & 1 \end{pmatrix} \cdot \begin{pmatrix} 1 & u \\ 0 & 1 \end{pmatrix} /. \{d \to x,\ f1 \to f1val,\ u \to d1val,\ k \to d2val\}$$

650

500

536

g

$$\left\{\left\{1 + \frac{1}{500}(-536 - g),\ 536 + 650\left(1 + \frac{1}{500}(-536 - g)\right) + g\right\},\ \left\{-\frac{1}{500},\ -\frac{3}{10}\right\}\right\}$$

```
MatrixForm[%]
```

$$\begin{pmatrix} 1 + \frac{1}{500}(-536 - g) & 536 + 650\left(1 + \frac{1}{500}(-536 - g)\right) + g \\ -\frac{1}{500} & -\frac{3}{10} \end{pmatrix}$$

```
q2ofg[g_] = ((A * q + B) / (C * q + D)) /.
  {A → Mat[[1]][[1]], B → Mat[[1]][[2]], C → Mat[[2]][[1]], D → Mat[[2]][[2]], q → q1}
```

$$(-0.370941 + 1.04827\,i)\left(536 + (650 + 423.897\,i)\left(1 + \frac{1}{500}(-536 - g)\right) + g\right)$$

```
Plot[Re[q2ofg[g]] , {g, 0, 300}, AxesLabel → {"distance (mm)", "curvature (1/mm)"}]
```

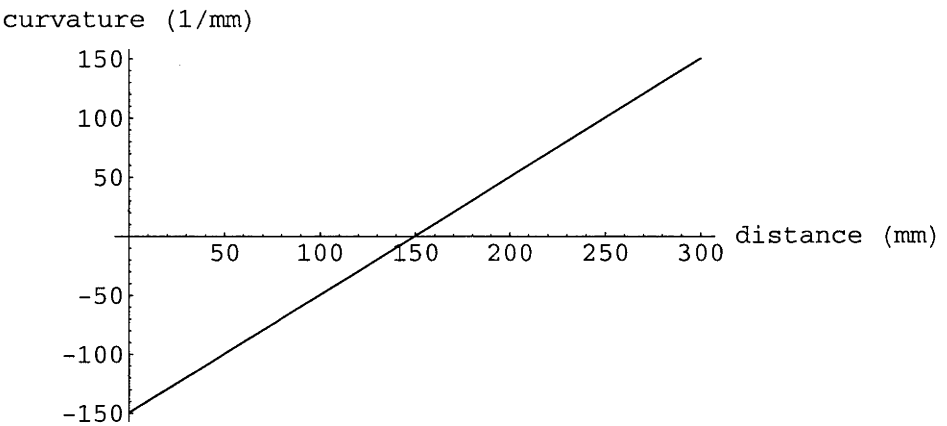


```
- Graphics -
```

```
overq[g] = 1 / q2ofg[g]
overq2[z] = 1 / q3ofg[z]
```

$$-\frac{0.3 + 0.847794\,i}{536 + (650 + 423.897\,i)\,\left(1 + \frac{1}{500}\,(-536 - g)\right) + g}$$

$$\frac{1}{q3ofg[z]}$$

```
w2of[g_] = Sqrt[Abs[1 / (Pi * (Im[overq[g]] / lambda))]] /. {lambda → λ}
```

$$\frac{0.0157367}{\sqrt{\text{Abs}\left[\text{Im}\left[-\frac{0.3+0.847794\,i}{536+(650+423.897\,i)\,\left(1+\frac{1}{500}\,(-536-g)\right)+g}\right]\right]}}$$

```
w2of[0]
```

```
0.374641
```

```
0.3795588020894773`
w3of[0]
```

```
0.379559
```

```
w3of[0]
```

```
Plot[w2of[g], {g, 0, 300}, AxesLabel → {"distance (mm)", "waist size(mm)"}]
```

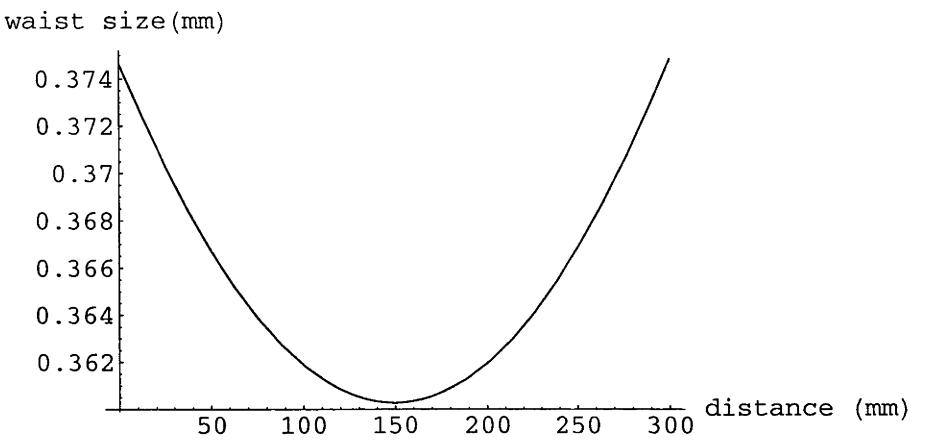

- Graphics -

- Graphics -

Syntax::noinfo : Input expression contains insufficient information to interpret result.

- Graphics -

```
FindMinimum[w2of[g], {g, 0, 150}]
```

```
{0.360277, {g → 149.47}}
```

```
(* Kogelnik and Li selfreproducing beam calculator for both
  saggital and tangential planes between the two focusing mirrors ,
 change cavity dimensions see what happens *)
<< Graphics`Graphics`
<< Graphics`Legend`
a = 110 (* separation between two focusing mirrors *)
f = 50  (* lens focal length *)
b = 300 (* separation between flat mirrors *)
c = 210 (* crossover beam lengths *)
d = 210
lambda = 0.000778 (* wavelength *)
x = .
theta = 0.113 (* mirror astigmatic angle *)
ft = f * Cos[theta]
fs = f / (Cos[theta])
Mattan = {{1, a - x}, {0, 1}} . {{1, 0}, {-1/f1, 1}} . {{1, b + c + d}, {0, 1}} . {{1, 0}, {-1/f1, 1}} . {{1, x}, {0, 1}} /. {f1 → ft}
Matsag = {{1, a - x}, {0, 1}} . {{1, 0}, {-1/f2, 1}} . {{1, b + c + d}, {0, 1}} . {{1, 0}, {-1/f2, 1}} . {{1, x}, {0, 1}} /. {f2 → fs}

110

50

300

210

210

0.000778

0.113

49.6811

50.3209

{{1 - 0.0201284 (110 - x) - 0.0201284 (110 + 720 (1 - 0.0201284 (110 - x)) - x),
   110 + 720 (1 - 0.0201284 (110 - x)) - x +
    (1 - 0.0201284 (110 - x) - 0.0201284 (110 + 720 (1 - 0.0201284 (110 - x)) - x)) x},
 {0.251452, -13.4924 + 0.251452 x}}

{{1 - 0.0198724 (110 - x) - 0.0198724 (110 + 720 (1 - 0.0198724 (110 - x)) - x),
   110 + 720 (1 - 0.0198724 (110 - x)) - x +
    (1 - 0.0198724 (110 - x) - 0.0198724 (110 + 720 (1 - 0.0198724 (110 - x)) - x)) x},
 {0.244593, -13.3082 + 0.244593 x}}
```

```
MatrixForm[%]
beamrad1[x_] =
 Sqrt[(2 * lambda * Abs[B]) / (Pi * Sqrt[Abs[4 - ((A + D) ^ 2)]])] /. {A → Matsag[[1]][[1]],
   B → Matsag[[1]][[2]], C → Matsag[[2]][[1]], D → Matsag[[2]][[2]]}
106.9`
beamrad2[x_] = Sqrt[(2 * lambda * Abs[B]) / (Pi * Sqrt[Abs[4 - ((A + D) ^ 2)]])] /.
  {A → Mattan[[1]][[1]], B → Mattan[[1]][[2]], C → Mattan[[2]][[1]], D → Mattan[[2]][[2]]}
```

$$\left(\frac{1 - 0.0198724\,(110 - x) - 0.0198724\,(110 + 720\,(1 - 0.0198724\,(110 - x)) - x) \quad 110 + 720\,(1 - 0.01}{0.244593}\right.$$

$$\left(0.0222551\sqrt{\text{Abs}[110 + 720\,(1 - 0.0198724\,(110 - x)) - x + (1 - 0.0198724\,(110 - x) - 0.0198724\,(110 + 720\,(1 - 0.0198724\,(110 - x)) - x))\,x]}\right) \Big/ \text{Abs}[4 - (-12.3082 - 0.0198724\,(110 - x) - 0.0198724\,(110 + 720\,(1 - 0.0198724\,(110 - x)) - x) + 0.244593\,x)^2]^{(1/4)}$$

106.9

$$\left(0.0222551\sqrt{\text{Abs}[110 + 720\,(1 - 0.0201284\,(110 - x)) - x + (1 - 0.0201284\,(110 - x) - 0.0201284\,(110 + 720\,(1 - 0.0201284\,(110 - x)) - x))\,x]}\right) \Big/ \text{Abs}[4 - (-12.4924 - 0.0201284\,(110 - x) - 0.0201284\,(110 + 720\,(1 - 0.0201284\,(110 - x)) - x) + 0.251452\,x)^2]^{(1/4)}$$

```
beamwaist1[x_] =
 Sqrt[(lambda * (Sqrt[Abs[4 - ((A + D) ^ 2)]])) / (2 * Pi * Abs[C])] /. {A → Matsag[[1]][[1]],
   B → Matsag[[1]][[2]], C → Matsag[[2]][[1]], D → Matsag[[2]][[2]]}
beamwaist2[x_] = Sqrt[(lambda * (Sqrt[Abs[4 - ((A + D) ^ 2)]])) / (2 * Pi * Abs[C])] /.
  {A → Mattan[[1]][[1]], B → Mattan[[1]][[2]], C → Mattan[[2]][[1]], D → Mattan[[2]][[2]]}
```

$$0.0224997 \Big/ \text{Abs}[4 - (-12.3082 - 0.0198724\,(110 - x) - 0.0198724\,(110 + 720\,(1 - 0.0198724\,(110 - x)) - x) + 0.244593\,x)^2]^{(1/4)}$$

$$0.0221908 \Big/ \text{Abs}[4 - (-12.4924 - 0.0201284\,(110 - x) - 0.0201284\,(110 + 720\,(1 - 0.0201284\,(110 - x)) - x) + 0.251452\,x)^2]^{(1/4)}$$

```
Plot[{beamrad1[x], beamrad2[x]}, {x, 1, 110}, PlotStyle → {Hue[.8], Hue[.65]},
 PlotLegend → {"sag", "tan"}, LegendPosition → {0.2, -0.4}, LegendSize → {.6, 0.2},
 LegendShadow → None, AxesLabel → {"distance(mm)", "w(mm)"}]
```

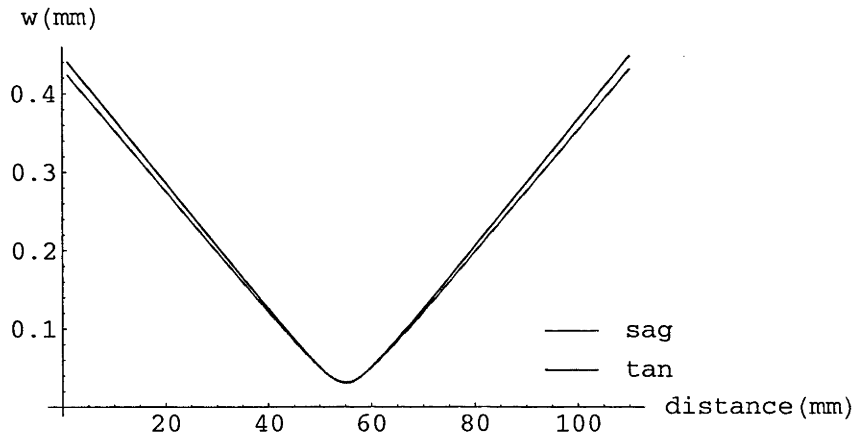

- Graphics -

```
FindMinimum[beamrad1[x], {x, 1, 100}]
beamwaist1[50]
```

```
{0.0316521, {x → 55.}}
```

```
0.0316521
```

```
(* Mathematica script to calculate laser waist inside
  LBO crystal using transfer matrix method by Kogelnik and Li by
  varying the mode matching lens to laser seperation we want to
  obtain the optimum waist inside the crystal of 31.5 microns *)

λ = 0.000778
w0 = 0.324 (* Ti:Sapph waist and corresponding q1 beam parameter *)
q1 = I ((Pi * w0 ^ 2) / λ)
refindex = 1.61
```

0.000778

0.324

423.897 i

1.61

0.267

0.267

T = 1186

1186

```
(* Total distance to cavity T=d1val+d2val, d1val=mode matching lens to laser,
 d2val=modematch lens to input coupler use d1val as parameter *)
```

```
d1val = 650
d3val = 46.5
f1val = 500
d2val = T - d1val
f2val = 50
fixed = 508
x = g
(* This is  the distance where it calculates the waist which for length of our
  crystal is 18 mm ie we are looking at the waist size halfway into the crystal *)
Mat = {{1, d/n}, {0, 1}}.{{1, h}, {0, 1}}.{{1, 0}, {-1/f2, 1}}.{{1, k}, {0, 1}}.{{1, v}, {0, 1}}.{{1, 0}, {-1/f1, 1}}.{{1, u}, {0, 1}} /.
  {d → x, f1 → f1val, u → d1val, f2 → f2val, v → d2val, h → d3val, n → refindex, k → fixed}
```

650

46.5

500

536

50

508

g

$$\left\{\left\{1+\frac{1}{50}\left(-46.5-0.621118\,g\right)+\frac{1}{500}\left(-46.5-1044\left(1+\frac{1}{50}\left(-46.5-0.621118\,g\right)\right)-0.621118\,g\right),\ 46.5+1044\left(1+\frac{1}{50}\left(-46.5-0.621118\,g\right)\right)+650\left(1+\frac{1}{50}\left(-46.5-0.621118\,g\right)+\frac{1}{500}\left(-46.5-1044\left(1+\frac{1}{50}\left(-46.5-0.621118\,g\right)\right)-0.621118\,g\right)\right)+0.621118\,g\right\},\ \left\{\frac{247}{12500},\ -\frac{1759}{250}\right\}\right\}$$

```
q2ofg[g_] = ((A * q + B) / (C * q + D)) /.
  {A → Mat[[1]][[1]], B → Mat[[1]][[2]], C → Mat[[2]][[1]], D → Mat[[2]][[2]], q → q1}
```

$$(-0.0587969-0.0699965\,i)\left(46.5+1044\left(1+\frac{1}{50}\left(-46.5-0.621118\,g\right)\right)+(650+423.897\,i)\left(1+\frac{1}{50}\left(-46.5-0.621118\,g\right)+\frac{1}{500}\left(-46.5-1044\left(1+\frac{1}{50}\left(-46.5-0.621118\,g\right)\right)-0.621118\,g\right)\right)+0.621118\,g\right)$$

```
q2ofg[10]
```

0.626005 + 3.54233 i

```
Plot[Re[q2ofg[g]] , {g, 0, 18}, AxesLabel → {"distance (mm)", "curvature (1/mm)"}]
```

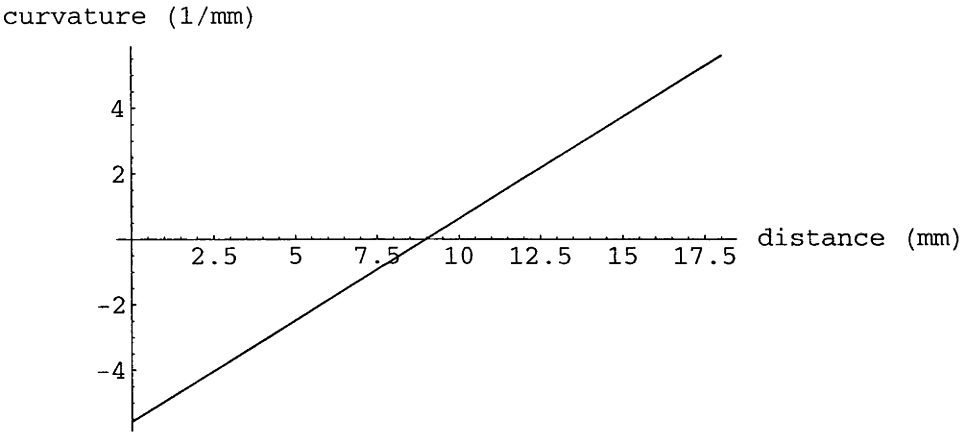

- Graphics -

```
overq[g] = 1 / q2ofg[g]
```

$$-(7.036 - 8.3762\,i) \Big/ \left(46.5 + 1044\left(1 + \frac{1}{50}(-46.5 - 0.621118\,g)\right) + (650 + 423.897\,i)\left(1 + \frac{1}{50}(-46.5 - 0.621118\,g) + \frac{1}{500}\left(-46.5 - 1044\left(1 + \frac{1}{50}(-46.5 - 0.621118\,g)\right) - 0.621118\,g\right)\right) + 0.621118\,g\right)$$

```
w2of[g_] = Sqrt[Abs[1 / (Pi * (Im[overq[g]] / lambda))]] /. {lambda → λ}
```

$$0.0157367 \Big/ \left(\sqrt{\text{Abs}\left[\text{Im}\left[-(7.036 - 8.3762\,i) \Big/ \left(46.5 + 1044\left(1 + \frac{1}{50}(-46.5 - 0.621118\,g)\right) + (650 + 423.897\,i)\left(1 + \frac{1}{50}(-46.5 - 0.621118\,g) + \frac{1}{500}\left(-46.5 - 1044\left(1 + \frac{1}{50}(-46.5 - 0.621118\,g)\right) - 0.621118\,g\right)\right) + 0.621118\,g\right)\right]\right]}\right)$$

```
w2of[1]
```

```
0.0509898
```

```
Plot[w2of[g], {g, 0, 18}, AxesLabel → {"distance (mm)", "waist size(mm)"}]
```

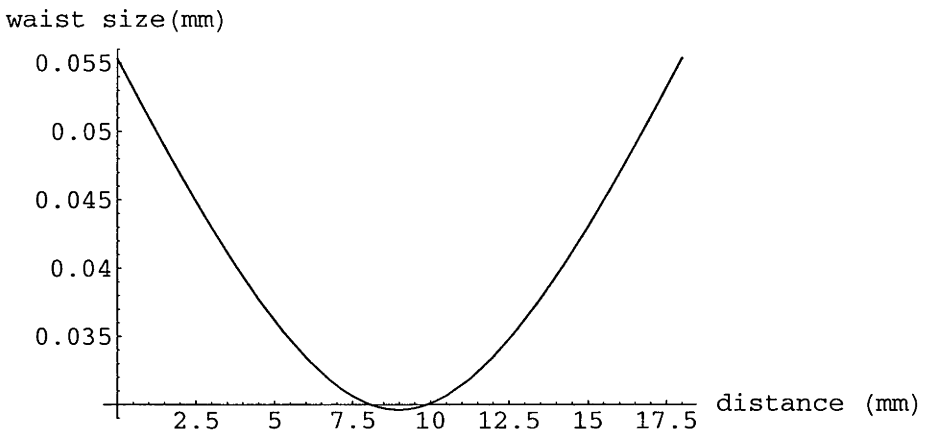

- Graphics -

```
FindMinimum[w2of[g], {g, 0, 18}]
```

```
{0.0296183, {g → 8.99213}}
```

```
(* Looking at ratio of 1/b, b being the confocal parameter ie
  the extent of the waist region 1 being the length of the crystal
  this optimises the Boyd and Kleinman focussing parameter *)
l = 18
b = ((0.0315) ^ 2.) * ((2.0 * Pi * index) / lambda) /. {lambda → λ, index → refindex}
rat = l / b
```

```
18
```

```
12.9017
```

```
1.39516
```

```
(* Mathematica notebook to calculate optimum beam size at first focusing mirror
  starting with a beam of the ideal waist size in the centre of the crystal *)
λ = 0.000778
w0 = 0.0315
q1 = I ((Pi * w0^2) / λ)
n = 1.61
l = 9
d1 = 45.45
w2 = 0.402
q3 = 51.041 + I ((Pi * w2^2) / λ)
f1val = 50
```

0.000778

0.0315

4.00674 i

1.61

9

45.45

0.402

51.041 + 652.563 i

50

```
x
g
Mat = {{1, d}, {0, 1}} . {{1, cr/ref}, {0, 1}} /. {d → x, ref → n, cr → 1}
Mat2 = {{1, f/ref}, {0, 1}} . {{1, t}, {0, 1}} . {{1, 0}, {-1/foc, 1}} /. {f → g, ref → n, t → d1, foc → f1val}
```

x

g

{{1, 5.59006 + x}, {0, 1}}

$$\left\{\left\{1+\frac{1}{50}\,(-45.45-0.621118\,g),\ 45.45+0.621118\,g\right\},\ \left\{-\frac{1}{50},\ 1\right\}\right\}$$

```
q2ofx[x_] = ((A * q + B) / (C * q + D)) /.
   {A → Mat[[1]][[1]], B → Mat[[1]][[2]], C → Mat[[2]][[1]], D → Mat[[2]][[2]], q → q1}
q3ofx[g_] = ((A * q4 + B) / (C * q4 + D)) /. {A → Mat2[[1]][[1]],
    B → Mat2[[1]][[2]], C → Mat2[[2]][[1]], D → Mat2[[2]][[2]], q4 → q3}
```

(5.59006 + 4.00674 i) + x

$$(-0.000122229 + 0.0766208\,i)\left(45.45 + (51.041 + 652.563\,i)\left(1+\frac{1}{50}\,(-45.45-0.621118\,g)\right) + 0.621118\,g\right)$$

```
q2ofx[45.45]
```

```
51.0401 + 4.00674 i
```

```
q3ofx[0]
Plot[Re[q2ofx[x]], {x, 0, 45.45},
 AxesLabel → {"distance (mm)", "wavefront curvature (1/mm)"}]
Plot[Re[q3ofx[g]], {g, 0, 8},
 AxesLabel → {"distance (mm)", "wavefront curvature (1/mm)"}]
Re[q2of[45.45]]
```

```
-4.55611 + 3.83104 i
```

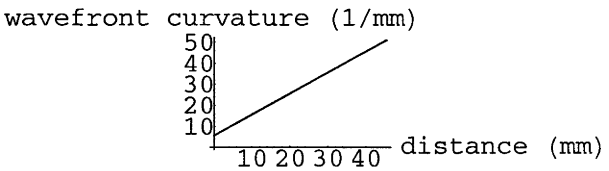


```
- Graphics -
```

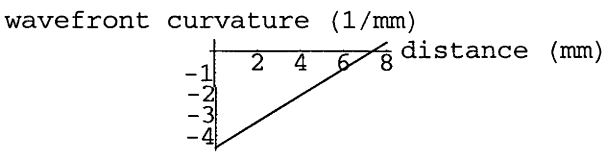


```
- Graphics -
```

```
General::spell1 : Possible spelling error: new symbol name "q2of" is similar to existing symbol "q2ofx".
```

```
Re[q2of[45.45]]
```

```
N[Re[q2of[45.45]]]
```

```
Re[q2of[45.45]]
```

```
overq[x] = 1 / q2ofx[x]
w2of[x_] = Sqrt[Abs[1 / (Pi * (Im[overq[x]] / lambda))]] /. {lambda → λ}
```

$$\frac{1}{(5.59006 + 4.00674\,i) + x}$$

```
General::spell1 : Possible spelling error: new symbol name "w2of" is similar to existing symbol "q2of".
```

$$\frac{0.0157367}{\sqrt{\text{Abs}\left[\text{Im}\left[\frac{1}{(5.59006+4.00674\,i)+x}\right]\right]}}$$

```
overq2[g] = 1 / q3ofx[g]
w3of[g_] = Sqrt[Abs[1 / (Pi * (Im[overq2[g]] / lambda))]] /. {lambda → λ}
```

$$-\frac{0.02082 + 13.0513\,i}{45.45 + (51.041 + 652.563\,i)\,\left(1 + \frac{1}{50}\,(-45.45 - 0.621118\,g)\right) + 0.621118\,g}$$

$$\frac{0.0157367}{\sqrt{\text{Abs}\left[\text{Im}\left[-\frac{0.02082+13.0513\,i}{45.45+(51.041+652.563\,i)\,\left(1+\frac{1}{50}\,(-45.45-0.621118\,g)\right)+0.621118\,g}\right]\right]}}$$

λ

0.000778

```
w2of[45.45]
w2of[0]
w3of[8]
w3of[0]
```

0.402499

0.0540708

0.0309799

0.04786

```
Plot[w2of[x], {x, 0, 45.45
 }, AxesLabel → {"distance(mm)", "w(mm)"}]
```

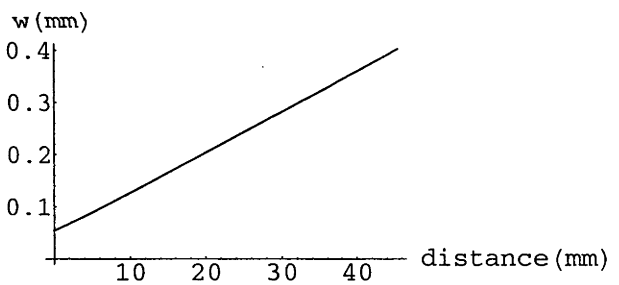

- Graphics -

```
- Graphics -
FindMinimum[w2of[x], {x, 0, 45.45}]
```

Syntax::noinfo : Input expression contains insufficient information to interpret result.

- Graphics -

{0.0315, {x → -5.59006}}

```
Plot[w3of[g], {g, 0, 10}, AxesLabel → {"distance(mm)", "w(mm)"}]
```

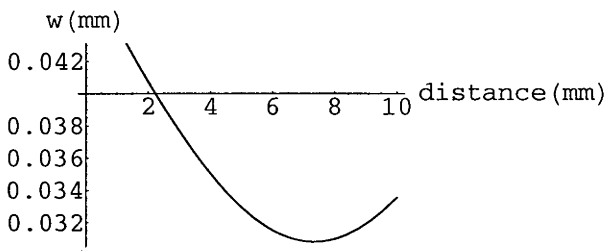

- Graphics -

```
FindMinimum[w3of[x], {x, 0, 10}]
```

```
{0.0308016, {x → 7.33534}}
```